PET/Organoclay Nanocomposites

A Thesis submitted for the degree of Doctor of Philosophy

by

Somchoke Sontikaew

School of Engineering and Design

(Mechanical engineering)

Brunel University

September 2008

Abstract

This thesis looks at the study of nanocomposites of Poly(ethylene terephthalate) and organoclays. Two methods of materials blending are investigated for the production of the nanocomposites: solvent blending and melt blending. The main objectives were the investigation of the influence of organoclays and processing conditions on morphological, rheological, mechanical properties, crystal structure and isothermal crystallization kinetics of the nanocomposite and a comparison with unfilled PET.

In solvent blending, the use of long sonication time and epoxy led to the formation of a two-dimensional network structure of long, thin particles in a solvent blended PET nanocomposite at low clay loading. The clay network structure seemed not to affect the tensile properties. The long, thin particles were able to be separated and dispersed further by high shear in a twin screw extruder, resulting in a high level of separation and dispersion. The crystallization of the solvent blended nanocomposite was not only influenced by the nanoclay but also by the residual solvent. The extent of clay dispersion did not affect the crystallization of the solvent blended sample.

Both solvent blended and melt blended nanocomposites showed that increasing the amount of surfactant improved the degree of nanoclay dispersion in the PET that led to an enhancement in the tensile properties of the nanocomposite compared to the unfilled polymer. The degradation of the organoclay during melt blending did not limit the nanoclay dispersion in the PET. The low thermal stability of the organoclay reduced the strength of the crystalline nanocomposite but it did not affect the strength of the amorphous nanocomposite. In contrast to the solvent blended sample, the extent of clay dispersion influenced the crystallization of the melt blended sample. The poorly dispersed particles were more efficient in nucleating PET crystallization than the well dispersed particles. The crystallization rate of PET increased as the surfactant concentration decreased.

Acknowledgement

I would like to express my gratitude to Dr Karnik Tarverdi and Dr Peter Allan for their support and advice throughout my study here. It is the most pleasure to have the assistance of many persons from Wolfson Centre for Material Processing and School of Engineering, Design (Mechanical engineering) and Experimental Techniques Centre at Brunel University throughout this work. I would like to express my special thank to the Royal Thai Government, Commission on higher education and King Mongkut's University of Technology Thonburi for the scholarship. Finally, thanks go to my family for their continuous encouragement and support throughout my PhD research and study at Brunel University.

List of Publications

K. Tarverdi, S. Sontikaew; *Experimental Study of Extrusion and Surface of treatment of organo clay with PET nanocomposites*, Conference Proceedings, ANTEC 2008, Milwaukee, May 2008.

K. Tarverdi, S Sontikaew; *Processing of PET Nanocomposites with Different Percentage of Surfactant Using Twin Screw Extruder Technology*, Conference Proceedings, ANTEC 2009, Chicago, Illinois, June 2009 (submitted November 2008).

Table of Content

List of Figures

List of Tables

Abbreviations and Symbols

ABS	Acrylonitrile-Butadiene-Styrene Copolymer	
ADA-clay	12-aminododecanoic acid-modified clay	
ATO	antimony doped tin oxide	
ARES	Advanced Rheometric Expansion System	
BHET	bis-hydroxyethyl terephthalate	
c	polymer solution concentration	g/dL
C_{12}PPh	dodecyl-triphenyl-phosphonium-chloride	
CEC	cation exchange capacity	mequiv/100g
CHDM	cyclohexane dimethanol	
CMC	cetyltrimetylammonium chloride	
CPC	cetylpyridinium chloride	
CSD	carbonated soft drinks	
C-10A	PET nanocomposites containing 2.5wt% 10A	
C-N2	PET nanocomposites containing 2.5wt% N2	
C-10A-M	C-10A with non-surfactant clay	
C-N2-M	C-N2 with non-surfactant clay	
d_{001}	interlayer distance	nm
DGEBA	diglycidyl ether of bisphenol A	
DMT	dimethyl terephthalate	
DP	degree of polymerization	
DSC	differential Scanning Calorimetry	
E	Young's modulus of the composite	MPa
E_f	modulus of filler	MPa
E_m	Young's modulus of the polymeric matrix	MPa
EG	ethylene glycol	
$E_{gallery}$	modulus of polymer in clay gallery	MPa
E-MA-GMA	ethylene–methyl acrylate–glycidyl methacrylate	
E_{MMT}	modulus of clay	MPa
EVA	ethylene vinyl acetate	

ExPET	extruded poly(ethylene terephthalate)	
ExPET-M	extruded PET treated with TFA	
$E_{//}$	longitudinal modulus	MPa
$E_{\perp}$	transverse modulus	MPa
G	shear modulus	Pa
G'	storage (elastic) modulus	Pa
G''	loss (viscous) modulus	Pa
G^*	complex modulus	Pa
HDT	heat distortion temperature	
HPTA	hydroxypentyl trimethylammonium iodide	
IP10TP	10-[3,5-bis(methoxycarbonyl)phenoxy] decyl triphenylphosphonium bromide)	
IPA	isophthalic acid	
IV	intrinsic viscosity	dL/g
K	overall crystallization rate constant	
L	Long period	nm
l	particle length	nm
l_a	amorphous thickness	nm
l_c	lamellar thickness	nm
ME	expandable fluorine mica	
MMT	montmorillonite	
M_n	number-average weight	g/mol
n	Degree of polymerization	
n	Avrami constant	
NCH	nylon-6 clay hybrid	
PA	Polyamide	
PBT	Poly(butylene terephthalate)	
PEO	poly (ethylene oxide)	
PET	poly(ethylene terephthalate)	
PETC	cast poly(ethylene terephthalate)	
PETN	poly(ethylene terephthalate-co-ethylene naphthalate)	

PEVA	poly(ethylene vinyl alcohol)	
PLM	polarized Light Microscopy	
PLSNs	polymer layered silicate nanocomposites	
PMMA	Poly(methyl methacrylate)	
POM	polyoxymethylene	
PVA	poly (vinyl alcohol)	
PVP	poly(N-vinyl pyrrolidone)	
SB	acidified sodium cocoamphophydroxypropylsulfonate	
$Sb(OAc)_3$	antimony acetate	
SEM	scanning Electron Microscopy	
SSP	solid state polymerization	
t	time	s
t_0	flow time of pure solvent mixture	s
t_1	flow time of polymer solution	s
$t_{1/2}$	crystallization half-time	s
T_{cc}	crystallization temperature from solid amorphous	°C
t_{layer}	thickness of clay layer	nm
t_p	particle thickness	nm
TEM	transmission Electron microscopy	
TFA	Trifluoroacetic acid	
TGA	Thermo Gravimetric Analysis	
T_g	glass transition temperature	°C
T_{hc}	crystallization temperature from melt	°C
T_m	melting temperature	°C
TPA	terephthalic acid	
TPE	thermoplastic elastomer	
VPET	virgin poly(ethylene terephthalate)	
V_f	volume of filler	
V_m	volume of matrix	
X	relative crystallinity	
XRD	X-ray diffraction	
σ	shear stress	Pa

γ	shear strain	
η	shear viscosity	Pa-s
η'	viscous dynamic viscosity	Pa-s
η''	elastic dynamic viscosity	Pa-s
η^*	complex viscosity	Pa-s
η_{rel}	relative viscosity	
$\dot{\gamma}$	shear rate	1/s
γ_o	small strain amplitude	
ω	frequency	rad/s
σ_o	shear-stress amplitude	
δ	phase shift angle	
β	power-law exponent describing low frequency dependence of G' and G''	
ξ	shape parameter dependent on filler geometry	
ϕ_{MMT}	volume fraction of clay	
$\phi_{gallery}$	volume fraction of clay-gallery space	
α	power-law index describing frequency dependence of η^*	
ΔH_c	heat of cold-crystallization	J/g
ΔH_{hc}	heat of hot-crystallization	J/g
ΔH_m	heat of fusion	J/g

Chapter 1

Introduction

1.1 Introduction

The background information regarding general details of polymeric materials, polymer layered silicate nanocomposites, and the development of nanocomposites, especially PET/organoclay nanocomposite, is described. The main objective and structure of the thesis are presented in this chapter.

1.2 Thesis outline

Chapter One provides some background information concerned with polymer/clay nanocomposites. General detail of polymer material, layered silicate clay, and also the development of nanocomposites are described. The objective and the Thesis's structure of the work are also presented.

Chapter Two provides the necessary background relevant to the contents of the thesis. The rheology-morphology relationship, mechanical properties, and crystalline behaviour and structure of nanocomposites are discussed.

Chapter Three describes the experimental method and materials used for the preparation of PET/organoclay nanocomposites via solvent blending and melt blending. The essential backgrounds of the experimental methods are also discussed.

Chapter Four reports on the preliminary experiments made to optimize the processing conditions for solvent blending. The solvent blended PET nanocomposites are prepared by assistance of ultrasonication and the use of a compatibilizer. The influence of processing conditions on the morphology, rheology, and tensile

properties and crystallization of the nanocomposite is studied. The clay dispersion mechanism is also described.

Chapter Five focuses on the effect of surfactant content on the morphological, rheological, tensile properties, and isothermal crystallization behaviour of melt blended PET nanocomposites. The relationships between the crystal structure and tensile properties for PET nanocomposites are discussed.

Chapter Six provides the overall conclusions of the work carried out in this study and proposes recommendations for further work on the subject.

1.3 Poly(ethylene terephthalate)

Poly(ethylene terephthalate) (PET) is one of the most versatile engineering plastics because of its low cost, chemical resistance, good thermal resistance, excellent electrical insulation and optical properties and high strength and stiffness with good processability [1]. PET is used in a variety of applications particularly in the

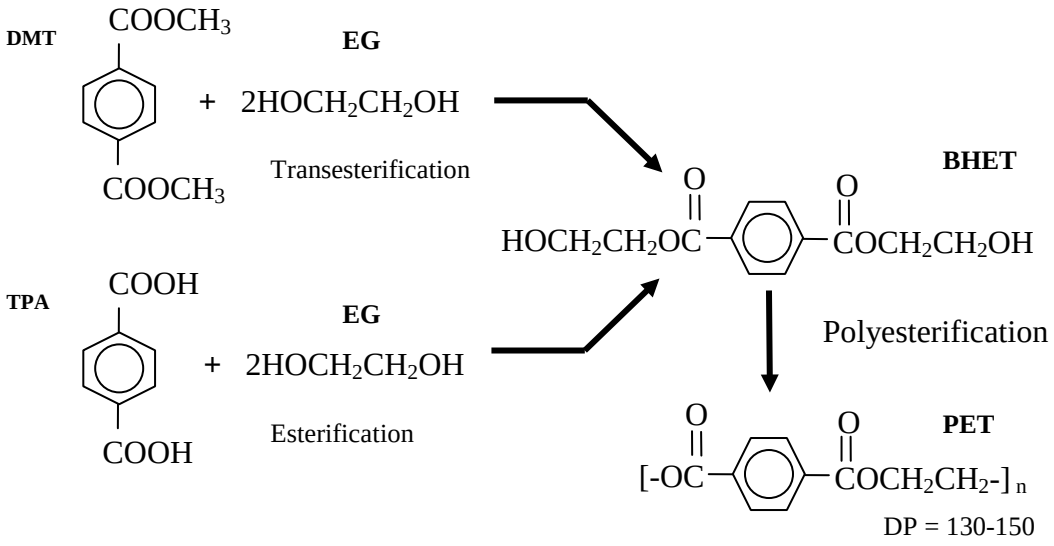

Figure 1.1 PET synthesis reactions.

manufacture of automotive and electronic parts, textile, soft drink containers, and high performance films.

PET is synthesized by step-growth polymerization [2], which requires two reaction steps as shown in Figure 1.1. Initially, the monomer, bis-hydroxyethyl terephthalate (BHET) or PET monomer, is produced by the *trans*-esterification reaction of dimethyl terephthalate (DMT) and ethylene glycol (EG) at a temperature of between 150 and 220°C and a pressure of 100kPa or by the *direct*-esterification reaction of terephthalic acid (TPA) and EG at a temperature of 240-260°C and a pressure of 300-500 kPa. The next step is a pre-polymerization reaction of BHET at a temperature of 250-280°C and a pressure of 2-3 kPa that produces PET with a degree of polymerization (DP, the number of repeat units in an average polymer chain) of 30. A higher molecular weight PET with DP of 100 is made by a further reaction at a temperature of 280–290°C and a pressure of 50–100 Pa. This product is used for the manufacture of fibres and sheets that have a number-average molecular weight (M_n) of 15 to 20kg/mol corresponding to an intrinsic viscosity (IV) of between 0.55 and 0.67 decilitre/gram (dL/g). For a product such as containers, the polymer is produced with a DP of 130-150 by the additional process of solid state polymerization (SSP) at 210°C under vacuum for 12h. The container-grade PET has an average molecular weight ranging from 24 to 36 kg/mol that corresponds to an IV of between 0.75 and 1.00 dL/g. Today, more than 70% of global PET manufacture is based on TPA. Fibre-grade and bottle-grade PET account for most of the global production of PET.

In the packaging industry, one of the main markets for PET is plastic bottles for carbonated soft drinks (CSD), water, and juice. Large quantities of PET resin are used for the production of stretch-blown bottles. The resin is a PET-copolymer that contains 2.3-3 wt% of added comonomers, such as isophthalic acid (IPA) or

cyclohexanedimethanol (CHDM) to disrupt the polymer chains. These resins have a lower melting point (T_m), slower crystallisation and improved clarity particularly in heavy wall applications [3] compared to the homopolymer. Materials with a higher IV offer greater mechanical strength and lower crystallinity relative to materials with a lower IV. Generally, the PET-bottle grade has an IV between 0.70-0.85 dL/g, a glass transition temperature (T_g) of about 69-115°C, a melting temperature (T_m) of approximately 250-260°C, and a density between 1.3-1.4 g/cm^3.

The properties of PET are not dependent on high crystallinity as in Polyamide (PA) and polyoxymethylene (POM) [4]. Its excellent mechanical properties are attributed to molecular orientation in the matrix, achieved by stretching during processing. The mechanical properties of the polymer are greatly enhanced in the orientation direction. The oriented PET molecules can, however, relax and change to random state during cooling process. This relaxation results in the loss of the improvement obtained from the orientation. In order to keep the orientation, the oriented molecules are frozen during the stretching process. Unoriented PET has average tensile strength at yield of 50-55MPa compared with up to 165MPa when PET has an orientation structure. The key properties of PET are attributed to molecular orientation, resulting in PET having the following [5].

- Excellent gloss and clarity
- Very tough and impact resistance
- Low permeability to CO_2
- Good processability
- Good dimensional ability
- High heat resistance

A processing approach for getting the orientation effects is:

- PET film with extremely low crystalline content is produced by melting PET pellets, shaping and then cooling rapidly in ice water.
- The amorphous film is warmed up by 25°C above glass transition temperature (T_g) and then stretched in the machine direction. The PET molecular chains orient in the stretch direction.
- The film is then stretched in the cross direction. Biaxial orientation structure of polymer molecules takes place in the PET film. The alignment of stretched molecules resulted in the formation of tiny crystallites (50-75Å) during the heat-stretching process [6]. This phenomenon is called strain-induced crystallization.
- The film is then cooled down to set the shape. The product is oriented and solidified to keep the orientation locked in place.

PET resins have a slow crystallization rate when this method of treatment is used so a low crystallinity is obtained during processing, resulting in transparent products. Most beverage bottles, such as CSD and water bottles produced by biaxial orientation blow moulding, have 25% crystallinity and heat resistance around 85°C. The bottle from this method can be filled with a hot liquid product with a temperature of 82-85°C. But in hot-fill applications with a temperature of about 91-93°C, for instance juices, sport drinks, and high acid drinks, the properties of the blow moulded PET bottles have to be enhanced by annealing at temperatures between T_g and T_m in a hot mould with a wall temperature of 125-145°C [6]. This process is called heat-setting technique which significantly increases the crystallinity to 39-42% and thus raises the heat resistance to nearly 95°C, enhances the gas barrier property.

Because of the very slow crystallization rate, PET injection moulded parts, for example automotive, electronic, and furniture parts, have poor mechanical properties. To promote crystallization in injection moulded parts, the mould temperature is increased to 140°C and the resin is modified using nucleating agents. Generally, commercial PET resins used in engineering applications are filled with 20-50% of fibreglass to increase strength, stiffness [7].

1.4 Polymer/layered silicate nanocomposites

Nylon-6 was initially used to manufacture polymer-layered silicate nanocomposites (PLSNs) by Toyota in 1986 [8,9]. PLSNs are recognised as nano-materials due to the interactions between organic and inorganic materials at nanoscale level. With 4%wt loadings of modified-layered silicate, the nylon-6 clay hybrid (NCH), that was used to produce timing belt covers for automotive parts, exhibited a significant property improvement with a 40% increase in tensile strength, a 68% increase in tensile modulus, and an increase of 87°C in the heat distortion temperature (HDT) compared with pure nylon-6. The NCH developed via an in situ polymerization method using ϵ-caprolactam as a nylon monomer possessed a fully exfoliated structure [8]. Due to the great improvements in mechanical and thermal properties with relatively small amount of nanoclays, various polymer systems have been extensively used to produce polymer nanocomposites since NCH was developed by Toyota. However, up to now only a few polymer nanocomposite systems such as those using nylon, polyolefin, thermoplastic elastomer (TPE), ethylene vinyl acetate (EVA), and epoxy have reached the market [10]. This is due to the incompatibility between polymers and layered silicates that has consequently made the production of nanocomposites with fully exfoliated structures difficult to achieve [11].

1.4.1 Structure and properties of layered silicate clay

The layered silicate clays or montmorillonite (MMT) usually used for the preparation of PLSNs are a type of 2:1 layered smectite clay mineral with a sheet-like structure in Figure 1.2 [12]. The chemical formula of MMT is $(Na_{1/3}(Al_{5/3}Mg_{1/3})Si_4O_{10}(OH)_2$. The silicate layer consists of one alumina octahedral layer in between the silica tetrahedral layers. The three layers create one clay sheet that is 0.92 nm thick and from 200 nm to several microns wide. Each sheet of the layered silicate stack is bonded together by an interlayer force (van der Waals force). The gaps between layers are called the interlayer or gallery. An important phenomenon occurring between galleries is isomorphous substitution that occurs when some atoms in the crystal structure are replaced with other atoms with different valence, for example Al^{3+} replaced by Mg^{2+}, leading to a decrease in positive charges. The isomorphous substitution results in negative charges on the clay surfaces that are neutralised by exchangeable cations such as Na^+, K^+ or Ca^{2+} ions inside the galleries.

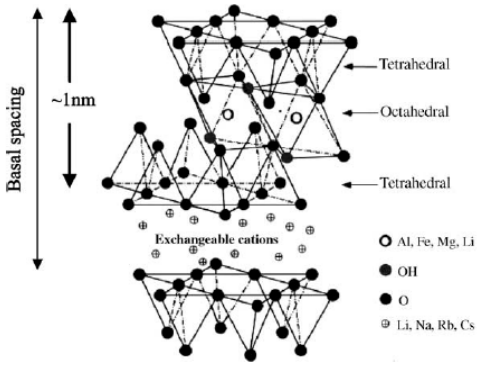

Figure 1.2 Structure of 2:1 layered silicate [12].

Because of the cations in the interlayer, the layered silicates are greatly hydrophilic and thus naturally incompatible with most polymers. However, the

cations in the galleries can be easily replaced with other cations such as alkyl ammonium ions, to make the clay more compatible with polymers. The alkyl ammonium cations play an important role in reducing the surface tension in the interlayer of clay. Furthermore, the alkylammonium ions offer functional groups that can react with a polymer. The amount of cation on the clay surfaces is described by cation exchange capacity (CEC), and usually expressed as mequiv/100g. MMT has molecular weight of 367.06 g. The amount of Na^+ ions on the MMT surface are 0.33. Therefore, the CEC of MMT is (0.33/367.06) x 10000 = 90 meq/100g compared to Cloisite Na^+ that has CEC of 95 meq/100g as shown in Table 1.1.

The smectite clays have a basic lattice similar to talc and mica. However, the exchangeable cations in the interlayer make the smectite clays different from talc and mica that do not have the exchangeable cations [13]. The exchangeable cations are able to be replaced with other cations with long alkyl tails that leads to an increase in the gallery spacing. This phenomenon is not found in talc and mica. The ion exchange property of MMT is an important property for the production of polymer nanocomposites. The smectite group of clay minerals such as MMT, hectorite, and saponite have been mainly used in the production of PLSNs. MMT is chemically categorized as Magnesium Aluminum Silicate, Al^{3+} substituted by Mg^{2+} while hectorite is chemically classified as Magnesium Silicate, Mg^{2+} replaced by Li^+ [14]. This difference in chemical composition produces a difference in the lattice structure. As a result, MMT is likely to have a sheet-like structure while hectorite is likely to have a strip-like structure. The properties of the final nanocomposite depend on the type of clay, clay modifier, type of polymers, and the intercalation methods. These factors affect the degree of exfoliation of layered silicates in a polymer matrix. The

effective exfoliation and dispersion of the layer silicates is important to accomplish the maximum performance of PLSNs.

1.4.2 Structure and properties of organically modified layer silicate

A conventional mixture of polymer and unmodified layered silicates may not achieve nanocomposites with an exfoliated structure. This can be analogous to unsuccessful polymer compounding, resulting in improper dispersion between organic and inorganic materials that tends to lower the mechanical and thermal properties of the composite. However, a good particle dispersion in a polymer is likely to produce a polymer nanocomposite with outstanding properties [12].

Natural layered silicates normally have hydrated Na^+, K^+, or Ca^{2+} in their galleries. Clearly, the unmodified layered silicates are only compatible with a hydrophilic polymer, such as poly (ethylene oxide) (PEO) or poly (vinyl alcohol) (PVA) [15]. To render hydrophilic silicate compatible with other polymers, the cations in the galleries of layered silicates are replaced with organic cations to obtain organophilic layered silicates that would be more likely to be effectively dispersed in many polymers. In general, this can be done by the replacement of the inorganic cations (Na^+, K^+, or Ca^{2+}) with cationic surfactants such as ammonium or phosphonium that have long alkyl chains. The organic cations reduce surface energy within the galleries and consequently will increase the interlayer distance. The layer spacing of modified layered silicates count on the CEC of the layered silicates [16], on chain length of alkylammonium cations [8] and on the number of alkyl chains [17]. Moreover, the functional groups supplied by ammonium ions can easily interact with the polymer matrix and enhance the strength of the interface between the clay and the polymer [18].

Table 1.1 Commercial organoclays

Manufacturer	Product	Surfactant	Surfactant concentration (meq/100g)	Interlayer distance (nm)	Application
Southern Clay Products, Inc.	Na+	-	95	1.17	-
	30B	MT2EtOH	90	1.85	PA
	10A	2MBHT	125	1.92	-
Cloisite®	25A	2MHTL8	95	1.86	-
	93A	M2HT	90	2.36	PA
	20A	2M2HT	95	2.42	PP,PE
	15A	2M2HT	125	3.15	PP,PE

M = methyl, H = hydrogen, B = benzyl, HT = dehydrogenated tallow (saturated long chain hydrocarbon), T = tallow (unsaturated long chain hydrocarbon), EtOH = hydroxyethyl, L8 = 2-ethylhexyl

Table 1.2 Commercial Polymer/clay Nanocomposites

Commercial PLSNs	Manufacturer	Products
Imperm®	Mitsubishi Gas Chemical Co., Inc.	Imperm 103: improved Nylon-MXD6 multi-gas barrier resin for co-injection molded, multilayer bottle
Polypro N.6H	Nanocor Inc.	Polypro N.6H: Homo-Polypropylene with 6% modified MMT
Durethan®	Bayer Corporation	KU2-2601: nylon 6 nanocomposite for films and paper coating
Aegis	Honeywell Polymers	Aegis NC: nylon 6 nanocomposite for film and paper coating Aegis™ OX: barrier and an oxygen scavenger for beer bottles.
Nanoblend™	PolyOne Corporation	Nanoblend Compounds LST 5501:engineering polyolefin Nanoblend Concentration: LST 5571: engineering polyolefin
Nanoblend Concentrations	PolyOne Corporation	MB1001: Master batch PP filled with 40% nanoclay MB1201: Master batch PE filled with 40% nanoclay MB 2201: Master batch PE filled with 40% nanoclay

Surface modified layered silicate clays or ***organoclays*** are available on the market. The various types of commercial organoclays and some polymer nanocomposites with trade names are summarized in Table 1.1 and Table 1.2 respectively. In them, the MMT clays are modified by a conventional chemical treatment with quaternary ammonium salt. The Cloisite series are the trade named

products of Southern Clay Products, Inc. Each grade has a different interlayer spacing that depends on the type of surfactant used and the surfactant content. However, a large gallery height does not necessarily offer a high potential exfoliation of the clay in the polymer matrix. According to Dennis et al. [19], the Cloisite 30B is easier to separate and disperse in nylon-6 than Cloisite 15A, although the interlayer distance of the former, 1.85 nm, is shorter than that of the latter nanoclay, 3.15 nm. The exfoliation of clay depends on the chemical structure of the surfactant on the clay surfaces rather than gallery spacing between silicate layers.

1.4.3 Types of Nanocomposites

Normally, each layered silicate sheet is around 1 nm thick, with a very high aspect ratio, and a large volume-to-weight ratio. In one gram of layered silicates the platelets will have a combined area of 700-800 m^2. Thus, only a small amount of layered silicates could potentially be dispersed throughout a polymer matrix. Three different types of polymer-clay nanocomposites are schematically presented in Figure 1.3 [20].

a. Tactoid nanocomposites: stacks of modified layered silicates are retained after introduction into the polymer. Subsequently, interaction between the nanolayers and polymer is not only unsuccessful but reduces mechanical properties of composite as well.

b. Intercalated nanocomposites: Polymer chains intercalate into layered silicate and separate the gallery spacing by 2-3 nm but the platelets are still in parallel. Only one of the polymer chains is taken in between the clay platelets.

c. Exfoliated nanocomposites: the polymer chains completely separate the clay into individual layers and further expand the interlayer spacing by 8-10 nm. The layer silicates are individually exfoliated and dispersed throughout the polymer matrix. Effective exfoliation can achieve enhanced properties, resulting in a high performance nanocomposite.

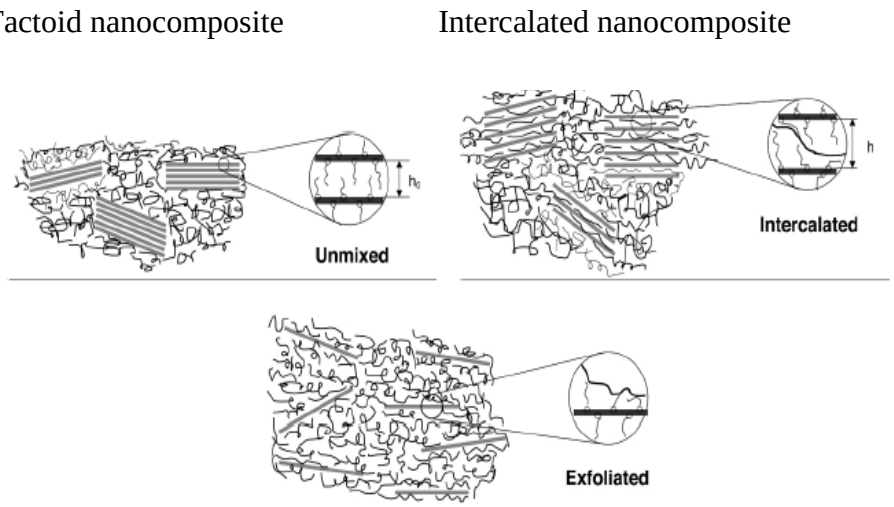

Figure 1.3 Types of polymer layered silicate nanocomposites [20]

1.4.4 Preparation

A number of techniques have been considered to disperse layered silicates in a polymer matrix. In the early stages three successful processes were developed and have been applied broadly. With respect to the starting materials and processing methods, they include [21]:

a) In situ polymerization

In this method polymer monomer is introduced between the silicate layers that swells and separates the layers during polymerization. This approach was first introduced by Toyota. It offered a well-exfoliated nanocomposite and has been widely used to produce various PLSNs.

b) Solution intercalation

Clays are swollen and distributed into a polymer solution. Kim et al. (2005) [22] used this method to prepare a PEO–PMMA clay nanocomposite. PEO and Poly(methyl methacrylate) (PMMA) were dissolved in methylene chloride and mixed with the organoclay using an ultrasonic generator to promote exfoliation. Due to the high price of the solvents and their negative effects for the environment this method is not considered appropriate for the commercial production of PLSNs. Nevertheless, some polymers such as the water-soluble polymers (PEO, PVA, poly(N-vinyl pyrrolidone) PVP and poly(ethylene vinyl alcohol) (PEVA)) can intercalate silicate layers in an aqueous solution [15]. This method has good potential and is viable for the commercial production of nanocomposites due to the low cost of the solvent that is environmentally safe.

c) Melt processing

This method utilizes conventional extrusion technology such as twin screw extruders to mix organoclay into polymers during melt processing. Although nanocomposites produced by using this process are not as good as that of in situ polymerization, the approach is practical and economical.

1.5 PET/organoclay nanocomposite

Over the last decade, PET/organoclay nanocomposites have been developed and their morphological, gas barrier, thermal and mechanical properties have been extensively investigated. PET/organoclay nanocomposites have been prepared by three different methods: in situ polymerization [23-26], melt blending [27-30] and solvent blending [31-33].

1.5.1 In situ polymerization

In situ polymerization involves the swelling of the organoclay by inserting monomer between the clay layers and then expanding and dispersing them into the matrix by polymerization reaction. Figures 1.4 to 1.7 show four different in situ polymerization methods recently used to produce a PET/clay nanocomposite.

Method one in Figure 1.4:

1. Natural clay is coated with an organic modifier with a low thermal stability (due to a lower decomposition temperature of the organic modifier than a melting temperature of PET) such as ammonium-based surfactant or high thermal stability such as dodecyl-triphenyl-phosphonium-chloride (C_{12}PPh).
2. The modified clay or organoclay is intercalated by the PET monomers.
3. The polymerization process takes place between the clay layers and the growth of polymer chains separates the particle stack into small stacks or single layers.

Ke et al. dispersed organically modified clay in PET via method one [34]. The complete separation and distribution of single clay layers was not achieved, but the tensile modulus of the 5 wt% clay nanocomposites increased three times compared with that of pure PET. Results of the non-isothermal crystallization showed that the

nanocomposites had a three times greater crystallization rate than the neat PET. Many research groups have prepared organoclays coated with thermally stable surfactants because of the degradation of alkyl-ammonium cations on the clay surfaces. By using the method one, the PET nanocomposites with 0–3 wt% of C_{12}PPh–clay showed improved thermal degradation and tensile properties compared to the pure PET [35]. Despite the use of a thermally stable surfactant, a fully exfoliated structure was not achieved.

Method two in Figure 1.5:

1. A special organic modifier with compatibilizer is used to coat the clay surfaces. The compatibilizer can react with PET monomers through the covalent bond to initiate the polymerization reaction. By this method it is believed that the PET main chains are tethered to the clay surfaces, resulting in achieving high mechanical performance.
2. The modified clay is intercalated by the PET monomers.
3. The polymerization process, initiated by the reaction between the compatibilizer and the PET monomer, takes place between the clay layers. The growth of the polymer chains separates the clay stacks into thinner stacks or single layers.

Imai et al. [36] developed a novel compatibilizer to modify expandable fluorine mica (ME). The novel compatibilizer (IP10TP, 10-[3,5-bis(methoxycarbonyl) phenoxy] decyl triphenylphosphonium bromide) has two methyl carboxylate groups that can react with PET through covalent bonding by transesterification, and a phosphonium ion group that can interact with the negatively charged mica layer. The ME coated with IP10TP was dispersed in the PET matrix by in situ polymerization of BHET (bis-hydroxyethyl terephthalate). The complete exfoliation of the modified mica in the PET was not achieved as shown by X-ray diffraction (XRD) results, but

the flexural modulus of the nanocomposite increased up to 1.7 times that of PET at its maximum. Similar to this technique, Zhang et al. [37] reported the use of hydroxypentyl trimethylammonium iodide (HPTA) as the clay modifier. HPTA, an ionically charged terminal monomer, was intercalated into the clay very efficiently by ion-exchange with the Na^+ cations on the clay surfaces. The PET/clay nanocomposites were prepared by polymerization of BHET initiated by HPTA on the surfaces of the modified clay. The XRD analysis of the nanocomposites containing HPTA showed exfoliation and the tensile strength was 58% higher than that of the unfilled PET. More work was published on this technique using a bifunctional compound as a compatibilizer and a commercial organoclay, 12-aminododecanoic acid-modified clay (ADA-clay) [38]. The compatibilizer contained an ester group that could covalently bond with the PET chains by transesterification, and an amino group that can form an ionic complex with the carboxylic acid of ADA. The PET/clay nanocomposite prepared by this novel method possessed a significantly higher storage modulus than the neat PET but the dispersed clay was mainly in the form of stacks rather than single layers, as revealed by TEM and XRD results.

Method three in Figure 1.6:

1. The unmodified clay is intercalated by a catalyst.
2. The unmodified clay is further intercalated by PET monomers, which is driven by the catalyst. It is believed that the catalyst in the clay layers increases the amount of the PET monomers between the clay layers.
3. Polymerization process takes place efficiently between the adjacent clay layers and the growth of polymer chains separate the stacks of the clay into smaller stacks or single layers.

This method is used to overcome two disadvantages of using an organoclay: One is the lack of a driving force between the clay layers during PET polymerization that would result in an intercalated morphology; the other is the thermal degradation of the organoclay during polymerization at the polymerization temperature of PET. Choi et al. [39] attempted to intercalate a catalyst directly into the clay interlayers before the polymerization process as seen in Figure 1.6. A chlorotitanium catalyst was directly inserted into the clay interlayers to increase the amount of monomer between the clay layers. This led to an increase in the number of PET chains polymerizing between the clay layers to subsequently break the stacks of clay into smaller stacks. However, a fully exfoliated clay in a PET matrix was not achieved.

Method four in Figure 1.7:

1. The unmodified clay is intercalated by a catalyst and an organic modifier.
2. The clay is further intercalated by the PET monomers, which is driven by the presence of the catalyst.
3. The polymerization process takes place efficiently between the adjacent clay layers and the growth of the polymer chains separates the stacks of the clay into smaller stacks or single layers.

In this method, Tsai et al. [24] treated the natural clay with the catalyst, antimony acetate [$Sb(OAc)_3$] and the long chain organic cation (SB, acidified sodium cocoamphophydroxypropylsulfonate). The function of the catalyst-treated clay created active sites between the clay layers during the polymerization process. The purpose of the SB-modified clay was to increase the compatibility and opportunity of a bond forming between the clay and the polymer. The resultant nanocomposites showed a significant improvement in the flexural strength and modulus, CO_2 gas

barrier properties and heat distortion temperature over the neat PET but complete exfoliation was not achieved.

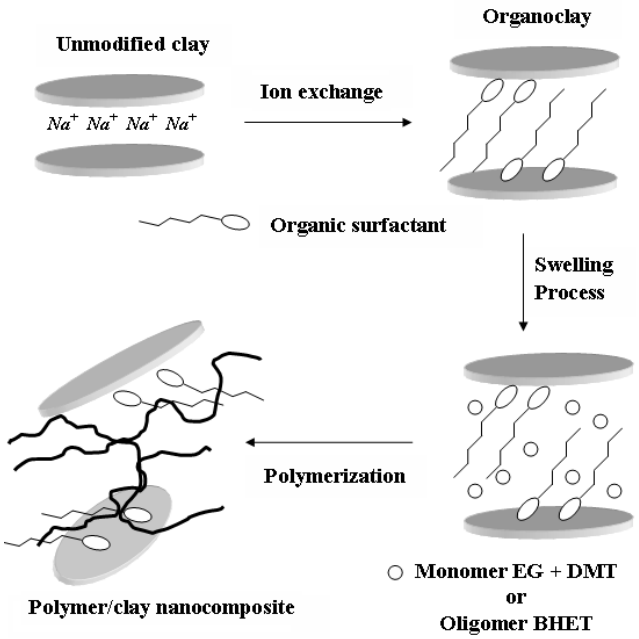

Figure 1.4 Method one: Polymerization process in the presence of a modified clay to produce a PET/organoclay nanocomposite.

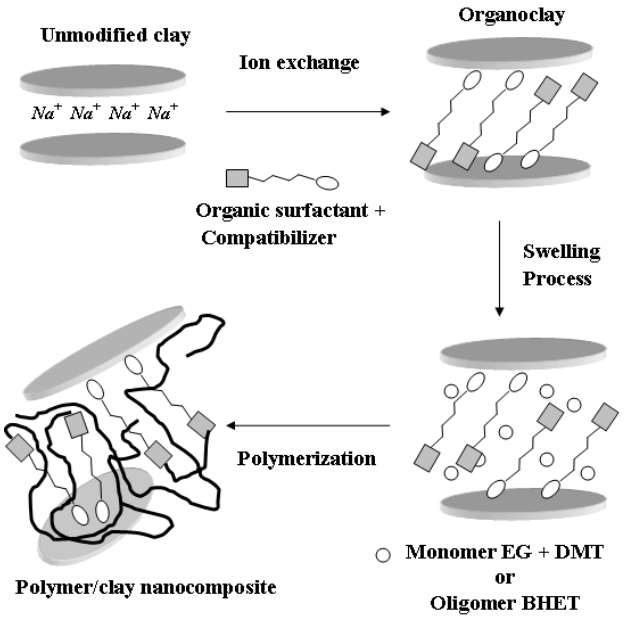

Figure 1.5 Method two: A modified clay has a compatibilizer that can react with the PET monomer through a covalent bond by the polymerization process to produce a PET/organoclay nanocomposite.

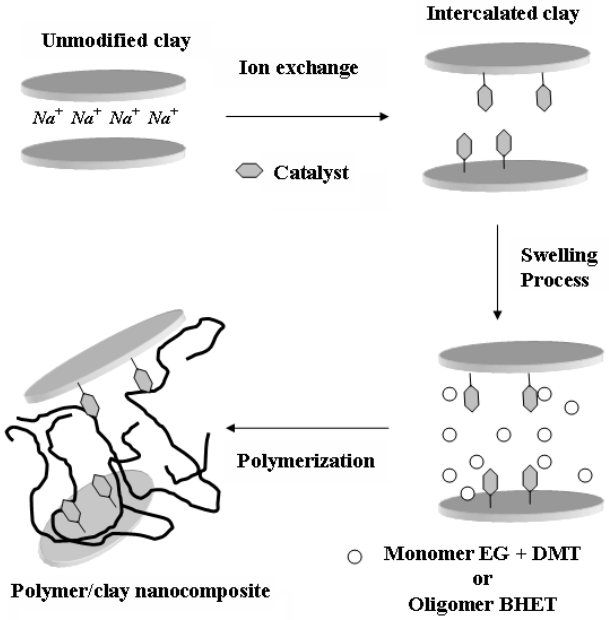

Figure 1.6 Method three: The catalyst is intercalated between the unmodified-clay layers before the polymerization process.

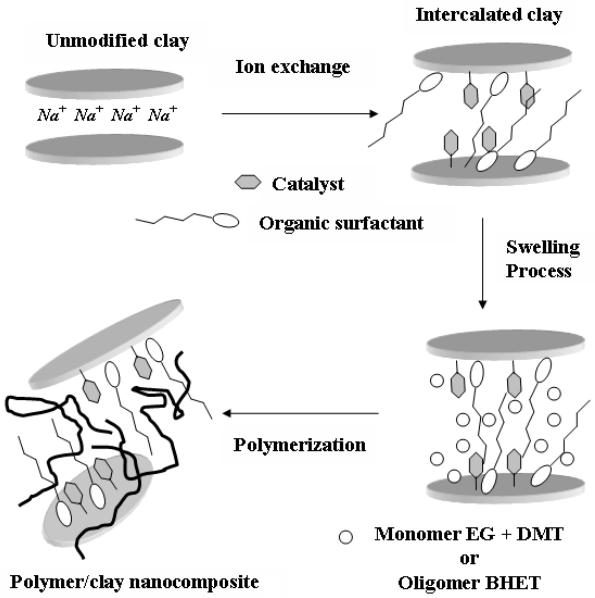

Figure 1.7 Method four: The catalyst intercalates the modified-clay layers before the polymerization process.

1.5.2 Melt blending

As well as in situ polymerization, a large preparation of the work to date on PET/organoclay nanocomposites has been based on melt blending. Matayabas et al. [40] prepared PET nanocomposites with varying amounts of Claytone-APA [41] by melt blending. The mixture of organoclay and PET was dried in a vacuum oven at 120°C and then extruded at 280°C on a twin screw extruder. The result showed that the inherent viscosities of the PET/organoclay nanocomposites decreased with increasing clay loading, indicating degradation of the PET matrix. The degradation was even higher when a high molecular weight PET was used. These experiments demonstrated that the degradation was attributed to the low decomposition temperature (250°C) of the organic modifier on the clay surfaces.

Davis et al. [42] dispersed two different organoclays in PET via melt blending in a co-rotating mini twin-screw extruder operating at 285°C. The nanocomposites produced with N,N-dimethyl-N,N-dioctadecylammonium treated MMT, which has a decomposition temperature of 250°C, were black, and brittle resulting from the modifier degradation at the processing temperature. The other sample compounded with 1,2-dimethyl-3-N-hexadecyl imidazolium treated MMT (hexadecyl-MMT), which has a decomposition temperature of 350°C, showed an intercalated structure in TEM and XRD. The TEM images of hexadecyl-MMT/PET nanocomposite showed that a lower screw speed (21 rad/s) and a shorter residence time (2 minutes) provided a better dispersion of clay than a higher screw speed (31 rad/s) and a longer residence times (5 minutes). A high degree of exfoliation by melt processing seems to require a specific residence time in the extruder with the appropriate shear history. Until now, there is only one published report [Davis et al. 42] that demonstrates the effect of processing conditions on the morphology of PET/organoclay nanocomposite.

Although the decomposition of the surfactants is inevitable, it might be reduced by processing at a lower temperature between 255 and 265°C instead of at 280°C. Recently, there has been more work with the commercial organoclays dispersed in PET [43-45] and recycled PET [46-50] by melt blending at a temperature of 250-265°C. All the commercial organoclays dispersed in the PET matrix showed a similar final interlayer spacing as seen in Table 1.3, suggesting that the chemical structure of the surfactants slightly affects the degree of the PET intercalation into the clay layers. Additionally, the increases in the tensile moduli for PET nanocomposites with 5-6 wt% of organoclay are in the range of 20 to 40% that of the pure PET.

Table 1.3 The composition and tensile modulus of PET nanocomposites based on quaternary ammonium organoclay prepared by melt blending

Sample description	Organoclay	Clay Interlayer spacing (nm)		Clay (wt)%	Relative tensile modulus	Ref
		without PET	with PET			
PET	-	-	-	0	1	[51]
PET-Cloisite 10A	2MBHT	1.92	3.56	5	1.36	
PET-Cloisite 15A	2M2HT	3.15	3.41	5	1.23	
PET-Na^+	Cloisite Na^+	0.98	-	5	1.13	
PET	-	-	-	0	1	[29]
PET-Cloisite 30B	MT2EtOH	1.91	3.75	6	1.4	
PET- Cloisite 15A	2M2HT-125	3.15	3.57	6	1.3	
PET- Cloisite 20A	2M2HT-95	2.51	3.43	6	1.4	
Recycled PET	-	-	-	-	1	[50]
rPET- Cloisite 30B	MT2EtOH	1.85	3.04	5	1.33	
rPET- Cloisite 20A	2M2HT-125	1.92	2.94	5	1.16	
rPET- Cloisite 25A	2MHTL8	1.86	2.85	5	1.37	
Recycled PET	-	-	-	-	1	[46]
rPET- Cloisite Na^+	Cloisite Na^+	0.98	1.2	5	1.14	
rPET- Cloisite 25A	2MHTL8	1.86	3.21	5	1.32	
PET	-	-	-	0	1	[47]
PET- Cloisite 25A	2MHTL8	1.86	3.0	5	1.2	
PET	-	-	-	-	-	[28]
PET-DK2	2MTEtOH	2.62	3.2	5	-	
rPET	-	-	-	-	1	[48]
rPET-67G	2M2HT	3.4	3.4	5	1.25	

M = methyl, H = hydrogen, B = benzyl, HT = dehydrogenated tallow, T = tallow, EtOH = hydroxyethyl, L8 = 2-ethylhexyl, rPET = recycled PET

Table 1.4 The composition and tensile modulus of PET/organoclay nanocomposites with compatibilizer

Sample	Compatibilizer	Organoclay	Clay (wt)%	Clay Interlayer spacing (nm)	Relative tensile modulus	Ref
PETI	Ionomer	-	-	-	1	[51]
PETI-10A		2MBHT	5	no peak	1.34	
PETI-15A		2M2HT-125	5	no peak	1.30	
PET-E-MA-GMA	E-MA-GMA	-	-	-	1	[44]
PET-E-MA-GMA						
PET-25A		2MHTL8	5	no peak	2	
rPET-25A	Silane	2MHTL8	5	30.4	1.29	[50]

The compatibility or interaction between the organoclay and the PET matrix can be enhanced by modifying the polymer with a polar function or adding a third component, as summarised in Table 1.4. Barber et al. [51] increased the polarity of PET by adding ionomers such as sulfonated groups and then compounded the PET ionomer blend (PET-I) with two commercial organoclays, Cloisite 10A and Cloisite 15A, by melt extrusion. The PET-I/organoclay nanocomposites exhibited an exfoliated structure, as detected by XRD. But when observed in TEM, the nanocomposites exhibited a combination of intercalated and exfoliated structures with some large stacks of clay layers. It was found that the addition of 5 wt% clay in the PET-I nanocomposites led to an increase in the tensile modulus of 35% and lowered the crystallization rates compared with neat PET-I. In addition, the improvement in the dispersion and the tensile moduli demonstrated that Cloisite 10A has stronger interactions with the PET-I than Cloisite 15A.

Alyamac et al. [44] added an impact modifier in the preparation of PET nanocomposites with Cloisite 25A by melt blending. From an X-ray diffraction analysis, the absence of a peak suggested that PET/organoclay with 5 wt% of the impact modifier exhibited the exfoliated structure. The impact modifier used was ethylene–methyl acrylate–glycidyl methacrylate (E-MA-GMA) terpolymer [52].

GMA has an epoxy group to react with the carboxyl and hydroxyl end groups of PET in the melt phase to form a graft copolymer. For this reason, the impact modifier may also be called a 'functionalized polymer' used as a compatibilizer. Moreover, it was found that the addition order of the three materials significantly affected the morphology and mechanical properties of the nanocomposite. Among the addition orders investigated, mixing PET and E-MA-GMA prior to the addition of the organoclay was the best sequence. The reason for this was that the melt viscosity of PET with E-MA-GMA was significantly improved, leading to an increase in the shear stress applied to disperse the clay.

Milan et al. [50] modified three commercial organoclays of Cloisite 10A, 25A, and 30B with silane, [3-(glycidyloxy)-propyl] trimethoxysilane. The modified organoclay was dispersed in recycled PET by melt blending. The modification of Cloisite 25A with the silane increased the homogeneity of the clay layers in recycled PET. An additional modification of Cloisite 10A and Cloisite 30B led to a lower level of exfoliation concomitant with a melt viscosity reduction. Cloisite 25A treated with silane revealed a combination of high stiffness and extensibility that could be utilized for the production of high-performance materials by spinning, extrusion, and blow molding technologies.

Further work has mixed the PET and organoclays coated with thermally stable surfactants in a twin screw extruder. Two organoclays were coated with alkyl-quinolinium and vinylbenzyl-ammonium surfactants that had a degradation temperature high enough to allow melt processing with PET (280°C) [53]. Although both organoclays were stable at the processing temperature, the morphologies of the nanocomposites obtained had rather poor dispersions as observed by TEM and XRD.

1.5.3 Solvent blending

By far, most of the work to date on PET/organoclay nanocomposite is based on in situ polymerization and melt intercalation rather than solvent intercalation. PET/organoclay nanocomposites prepared via in situ polymerization in general give a higher degree of clay intercalation and exfoliation than melt processing. Melt processing is, on the other hand, a convenient and flexible process. Both processes, however, are carried out at the processing temperature of 260-280°C for PET and this combined with a long residence time, consequently causes degradation of the ammonium-based surfactants in the organoclay that resulted in a limited intercalation of the polymer chains into the clay layers. Solution blending that does not require such a high processing temperature could, therefore, be used to prepare the nanocomposites with the possibility of an improved exfoliation of the clay.

A nanocomposite of Cloisite 30B (30B) in PET produced by solvent blending has formed a partially intercalated structure, but the 30B-PET nanocomposite with an addition of ionomer possessed a partially exfoliated structure as evidenced by XRD [31]. In the experiments on solution blending, the clay was organically modified with the intercalation agent cetyltrimethylammonium chloride (CMC) [32] and cetylpyridinium chloride (CPC) [33], and was dispersed in the PET solution. The PET nanocomposites with both organoclays showed high levels of dispersion without an agglomeration of particles at a low organoclay content (5 wt %).

1.6 Scope of the Thesis

Despite the intensive research in this area, the degree of clay intercalation/exfoliation achieved in PET is still relatively low compared with other successful polymer/clay systems, such as nylon and polypropylene [54]. PET/organoclay nanocomposites have possessed partially exfoliated structure rather than the fully exfoliated structure. Currently, the preparation of a fully exfoliated organoclay in the PET is the challenge. The main aim of this work was to prepare PET/organoclay nanocomposites via two different methods with the following objectives.

1. To prepare fully exfoliated organoclay/PET nanocomposites via solvent blending with the assistance of ultrasonication and a compatibilizer. The effects of the sonication time, compatibilizer, organic modifiers, and the percentage of organoclay on the morphological, rheological, mechanical, and thermal properties were to be studied. The structure-rheological correlation and the effect of a clay network structure on the tensile properties were also to be investigated.

2. To investigate the effect of a surfactant content on the morphological, rheological, tensile properties, crystal morphology, and isothermal crystallization kinetics of PET nanocomposites prepared by melt blending.

Chapter 2

Background

2.1 Introduction

This chapter provides a technical background to the contents of the thesis. The rheology-morphology relationship, mechanical properties, crystallization behaviour and crystal structure of PET/clay nanocomposites are also discussed. An understanding of the melt rheological properties of polymer-clay nanocomposites is crucial to gaining a fundamental understanding of the processability and structure-property relations of these materials [20]. The prediction of the processing behaviour or the solution of processing problems can be achieved by understanding/using the melt rheological properties. A knowledge of a structure-property relationship is of fundamental importance in designing/developing materials with desired properties [55]. In order to predict the modulus of nanocomposites based on nanoclay, the theoretical modulus (Halpin-Tsai) is described in this chapter. The effect of the nanoclay on the isothermal crystallization kinetics of polymer/clay nanocomposites was studied by using the Avrami equation and details of this are also presented in this section.

2.2 Melt rheology and structure-property relationship

Rheology is the scientific study of the deformation of materials when the materials are subjected to forces [56,57]. There are two main aspects for the rheological studies. The first is the determination of a quantitative relationship between the deformation

(strain) and force (stress) for the materials of interest. The second is the determination of the relationships that show how the structure and composition of the material combined with the temperature and pressure affect the rheological behaviour.

The general rheological behaviour that can be exhibited by materials involves the properties of elasticity, viscosity, and viscoelasticity. Elastic materials can return to their original shape whenever a deforming force is removed. The amount of force on the elastic material is proportional to the *amount* of deformation.

For simple shear

$$\sigma = G\gamma \tag{2.1}$$

where σ is shear stress, γ is shear strain and G is the shear modulus.

In viscous materials, the deformation is permanent. Unlike the elastic material, the amount of force on the viscous materials is not related to the *amount* of deformation but to the *rate* of deformation.

For simple shear

$$\sigma = \eta \dot{\gamma} \tag{2.2}$$

where η is the shear viscosity and $\dot{\gamma}$ is the shear rate.

Polymeric materials including solutions, melts, and crosslinked elastomers exhibit viscoelastic deformation because they show both viscous and elastic deformation. The viscoelastic properties of polymers are strongly influenced by the structure of the materials. Thus, in order to understand of the rheology of polymer composites, it is essential to determine the interaction between of polymer and filler and the structure-property relationship.

The simplest type of viscoelastic response is linear viscoelasticity. In linear viscoelastic behaviour, *when the strain is very small*, the shear modulus (G) is independent of the shear strain and the shear viscosity (η) is independent of the shear rate.

For linear viscoelastic: $G(t), \eta(t)$

where t is time.

The linear viscoelastic properties of polymers can be examined by several methods including, stress relaxation (constant strain), creep (constant force), and small amplitude oscillatory shear. Among these, small amplitude oscillation shear has been the most widely used technique to determine the linear viscoelastic properties of a polymer liquid.

In this method, a sample of melt polymer is subjected to a *small shear strain* as a sinusoidal function of time which is given by:

$$\gamma(t) = \gamma_o \sin(\omega t) \tag{2.3}$$

where γ_o is the small strain amplitude and ω is the frequency.

The resultant-shear stress is then measured as a function of time and has the same frequency as the strain.

$$\begin{aligned} \sigma(t) &= \sigma_o \sin(\omega t + \delta) \\ &= \sigma_o \sin(\omega t)\cos(\delta) + \sigma_o \cos(\omega t)\sin(\delta) \end{aligned} \tag{2.4}$$

where σ_o is shear-stress amplitude and δ is a phase shift angle.

Multiply the right-hand term of equation (2.4) by $\frac{\gamma_0}{\gamma_0}$

$$\sigma(t) = \frac{\gamma_o}{\gamma_o}\sigma_o \sin(\omega t)\cos(\delta) + \frac{\gamma_o}{\gamma_o}\sigma_o \cos(\omega t)\sin(\delta)$$

$$\sigma(t) = \gamma_o[G^{'} \sin(\omega t) + G^{"} \cos(\omega t)] \tag{2.5}$$

$$G^{'} = \frac{\sigma_o}{\gamma_o}\cos(\delta) \text{ and } G^{"} = \frac{\sigma_o}{\gamma_o}\sin(\delta) \tag{2.6}$$

where G' and G'' are storage (elastic) and loss (viscous) moduli.

The complex modulus (G^*), an evaluation of a material's overall resistance to deformation can be evaluated from

$$G^* = G^{'} + iG^{"} \tag{2.7}$$

where i is the imaginary unit.

The ratio of the viscous modulus to the elastic modulus is the tangent of the phase angle shift (δ) between the stress and the strain

$$\tan(\delta) = \frac{G^{"}}{G^{'}} \tag{2.8}$$

Alternatively, these experiments can be used in terms of an oscillation shear rate ($\dot{\gamma}$) which leads into a definition of a dynamic viscosity. The shear rate is the derivative of the shear strain.

$$\dot{\gamma} = \frac{d\gamma}{dt} = \gamma_o \omega \cos(\omega t) = \dot{\gamma_o} \cos(\omega t) \tag{2.9}$$

The viscosity function is the ratio of the stress to the shear rate.

Multiply equation (2.4) both sides by $\frac{\dot{\gamma_\circ}}{\dot{\gamma_\circ}}$

$$\sigma(t) = \frac{\dot{\gamma}}{\dot{\gamma}_o}\sigma_o \sin(\omega t)\cos(\delta) + \frac{\dot{\gamma}}{\dot{\gamma}_o}\sigma_o \cos(\omega t)\sin(\delta)$$

$$\sigma(t) = \dot{\gamma}_o[\eta'' \sin(\omega t) + \eta' \cos(\omega t)] \tag{2.10}$$

$$\eta'' = \frac{\sigma_o}{\dot{\gamma}_o}\cos(\delta) = \frac{\sigma_o}{\gamma_o \omega}\cos(\delta) = G'/\omega \tag{2.11}$$

$$\eta' = \frac{\sigma_o}{\dot{\gamma}_o}\sin(\delta) = \frac{\sigma_o}{\gamma_o \omega}\sin(\delta) = G''/\omega \tag{2.12}$$

where η' and η'' are the viscous and elastic dynamic viscosities respectively.

The complex viscosity (η^*) is a measure of a material's overall resistance to flow as a function of shear rate and can be calculated from

$$\eta^* = \eta' + i\eta'' \tag{2.13}$$

During the last decade, this method has been extensively used to probe dispersion states of organoclay in polymer matrices [58-61]. Figure 2.1 shows the schematic rheological behaviour to the different level of clay dispersion in polystyrene nanocomposites [62]. Figure 2.1(a) shows the linear viscoelastic response, storage modulus (G') and loss modulus (G'') of the pure polymer melt as a function of the testing frequencies (ω) plotted in log-log scale. The useful parameter is the power-law exponent (β) which describes the low-frequency response of G' and G''. In low frequency zone or terminal zone, the magnitudes of G' and G'' gradually decrease with decreasing frequency by $G' \propto \omega^{\beta \to 2}$, $G'' \propto \omega^{\beta \to 1}$. And finally they approach a value of 0 at very low frequency, indicating that the polymer chains fully relax or totally change from elastic deformation to viscous deformation. This

phenomenon signifies that the molten polymer exhibits liquid-like behaviour (or viscous deformation).

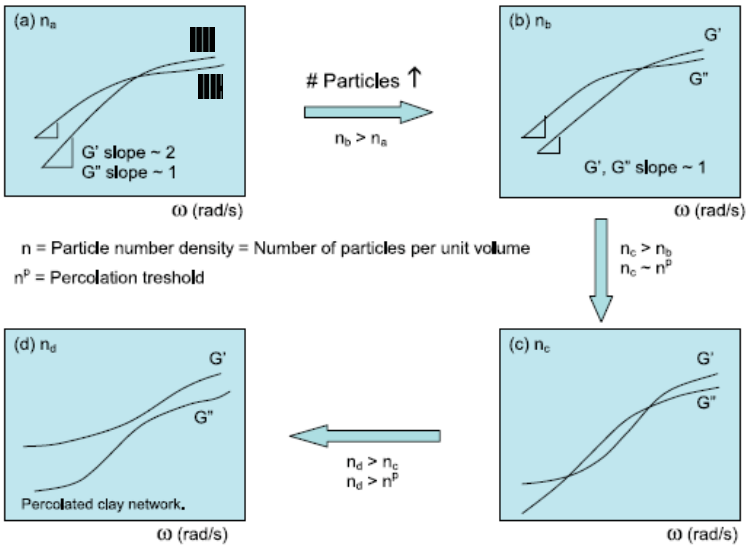

Figure 2.1 A schematic diagram of the speculated rheological behaviour of a PS composite melt with respect to an increase in the number of particles per unit volume [62].

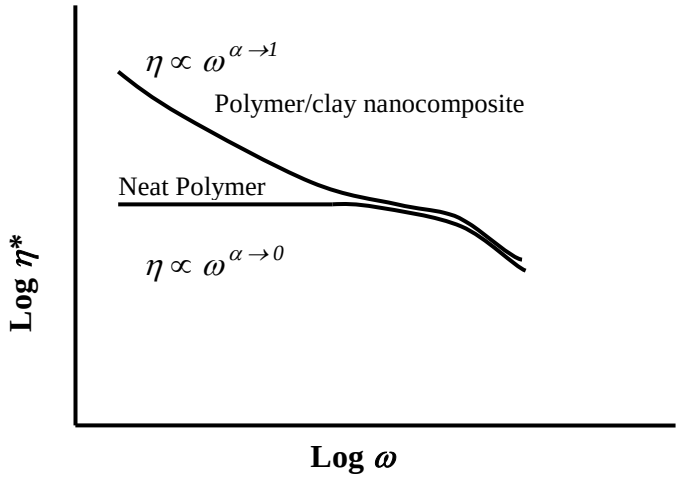

Figure 2.2 Schematic diagram of comparison of the complex viscosity between the neat polymer and its nanocomposite.

In the case of polymer/clay nanocomposite, adding clay particles results in a reduction of the low-frequency dependence with $G' \propto \omega^{\beta \to 1}$ in Figure 2.1(b). It indicates that the viscoelastic behaviour changes from liquid-like (viscous deformation) for the neat polymers to a more solid-like (elastic deformation) for the nanocomposites at low frequencies. When the degree of clay dispersion increases, G' and G'' exhibit a more solid-like behaviour at low frequency zone by $G' > G''$ and $G' \propto \omega^{\beta \to 0}$ as shown in Figure 2.1(c). A further increase in the clay dispersion, G' and G'' in Figure 2.1(d) shows plateau behaviour at the low frequencies by G', $G'' \propto \omega^0$. In this frequency range, G' and G'' do not change significantly with frequency. The values of G' and G'' do not approach 0 at very low frequencies. This indicates that the polymer chains in nanocomposites are unable to relax completely. Moreover, G' is greater than G'' over the whole frequency range, indicating a percolated clay network in which the clay layers are unable to freely rotate, due to physical interaction between the dispersed nanoclay particles [60].

Figure 2.2 shows the complex viscosity (η^*) of the neat polymer and the nanocomposite. The shear-thinning index (α) of complex viscosity was used to determine the degree of exfoliation of clay [63]. The complex viscosity can be defined by the following equation:

$$\eta^* = A\omega^{-\alpha} \tag{2.14}$$

where A is a sample-specific pre-exponential factor. A and α can be calculated from the plot of $\log(\eta^*)$ vs. $\log(\omega)$ as

$$\log(\eta^*) = \log(A) - \alpha\log(\omega) \tag{2.15}$$

and the shear-thinning index is determined from the slope of the straight line.

Typical polymer melts exhibit Newtonian behaviour with a shear-thinning index of 0 at low frequencies and shear thinning behaviour (Non Newtonian) at high frequencies. The nanocomposites, however, exhibit shear thinning at low frequencies with a shear-thinning index approaching 1. The shear-thinning index increases from near zero for the pure polymer to a value close to 1 with the increase in the concentration and dispersion of clay.

2.3 Tensile properties of polymer/clay nanocomposites

The tensile modulus of the PA6/clay nanocomposites has been predicted using the theory of Halpin-Tsai [64]. The predictions were compared to experimental data from the nanocomposites. It was found that in theory the stiffness of the fully exfoliated clay PA6 nanocomposites can be satisfactorily described. The Halpin-Tsai equation has been developed for predicting the modulus of composite material based on the geometry and orientation of filler and the modulus of the filler and matrix. The longitudinal modulus ($E_{//}$) and transverse modulus ($E_{\perp}$) are the composite moduli parallel and perpendicular to the filler direction respectively. These are calculated from the Halpin-Tsai equation,

$$\frac{E}{E_m} = \frac{1+\xi\eta\phi_f}{1-\eta\phi_f} \tag{2.16}$$

where E and E_m are the Young's modulus of the composite and matrix, respectively. ξ is a shape parameter dependent on filler geometry and loading direction as seen in Figure 2.3.

If clay layers are parallel in the direction of force, $\xi = 2l/t_p$ is for the longitudinal modulus, where l and t_p are the length and thickness of the clay layers, and therefore

$$\frac{E_{//}}{E_m} = \frac{1+(2l/t_p)\eta\phi_f}{1-\eta\phi_f} \tag{2.17}$$

ϕ_f is volume fraction of filler (MMT with density of 2.83g/cm^3 [64]) and given by

$$\phi_f = V_f/(V_f + V_m) \tag{2.18}$$

where V_f, V_m are volume of the filler and the matrix.

Practically, the volume fraction of clay in the polymer nanocomposites is obtained by placing the nanocomposite pellets in a furnace at 900°C for 45 minutes. The clay ash was weighed and actual clay weight is calculated by the following equation [64].

$$\%MMT = \frac{\%MMT_{ash}}{0.935} \tag{2.19}$$

where $\%MMT_{ash}$ is the mass after completely burning relative to the original nanocomposite mass. The factor of 0.935 corrects for the loss of structural water during burning [65].

And η is given by

$$\eta = \frac{E_f/E_m - 1}{E_f/E_m + \xi} \tag{2.20}$$

where $\xi = 2l/t_p$ is for the longitudinal modulus and E_f represents the modulus of filler

For fully exfoliated and well oriented clay layers

$$E_f = E_{MMT} \tag{2.21}$$

and for partially exfoliated clay [66]

$$E_f = \phi_{MMT} E_{MMT} + \phi_{gallery} E_{gallery} \tag{2.22}$$

where ϕ_{MMT} and $\phi_{gallery}$ are volume fraction of clay (MMT) and gallery space in the stack of clay, while E_{MMT} and $E_{gallery}$ are modulus of clay and modulus of the polymer in the gallery. From Figure 2.4, the volume fraction of clay and gallery are calculated by equation (2.23) and (2.24).

$$\phi_{MMT} = \frac{t_{layer}}{d_{001}} \tag{2.23}$$

$$\phi_{gallery} = \frac{(n-1)(d_{001} - t_{layer})}{d_{001}(n-1) + t_{layer}} \tag{2.24}$$

where t_{layer} is the thickness of clay layer, d_{001} is interlayer distance.

The modulus of the polymer in the gallery is much smaller than that of clay layers (178GPa for MMT [64]) and therefore, equation (2.22) reduces to

$$E_f = \phi_{MMT} E_{MMT} \tag{2.25}$$

There are some assumptions in the use of this equation [67]:

(i) The matrix and filler are linearly elastic, isotropic, and firmly bonded.

(ii) The filler is perfectly aligned, asymmetric, and uniform in shape and size.

(iii) The properties of the matrix and filler are identical to those of the pure component.

As $\xi \to \infty$, the equation (2.16) reduces to the upper bound of modulus in equation (2.26) and conversely, as $\xi \to 0$ the equation (2.16) reduces to the lower bound of modulus in equation (2.27).

Upper bound of modulus

$$E_1 = E_f \cdot \phi_f + E_m \cdot (1 - \phi_f) \tag{2.26}$$

Lower bound of modulus

$$E_2 = \frac{E_m \cdot E_f}{\phi_f \cdot E_m + (1 - \phi_f) E_f} \tag{2.27}$$

In the case of randomly oriented layers in the matrix (Figure 2.5), the following equation was proposed [64]:

$$E_{ran-3D}^{layer} = 0.49 E_{//} + 0.51 E_{\perp} \tag{2.28}$$

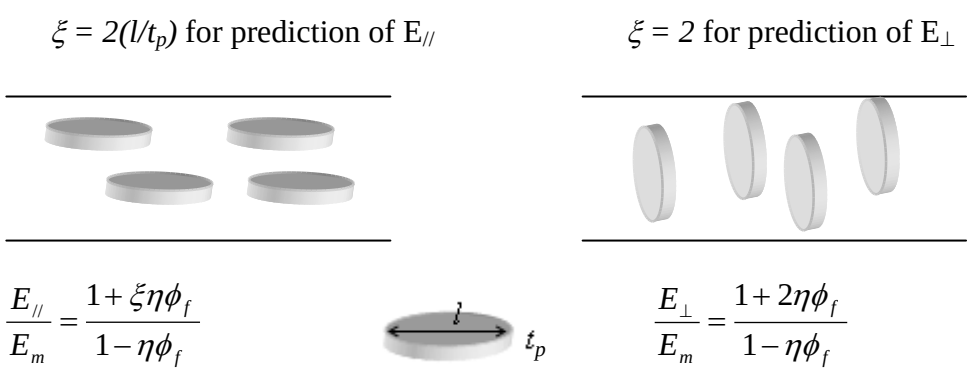

Disk-like particles in a polymer matrix parallel to the direction of force

Disk-like layers in a polymer matrix perpendicular to the force direction

Figure 2.3 Shape parameter (ξ) for the prediction of $E_{//}$ and $E_{\perp}$, where l = layer diameter, $t_p = (n-1)\, d_{001} + t_{layer}$

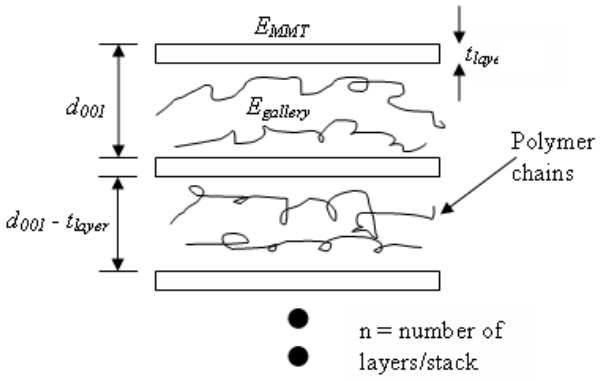

$$E_f = \phi_{MMT} E_{MMT} + \phi_{gallery} E_{gallery}$$

$$\phi_{MMT} = \frac{t_{layer}}{d_{001}} = \frac{0.94}{d_{001}}$$

$$\phi_{gallery} = \frac{(n-1)(d_{001} - t_{layer})}{d_{001}(n-1) + t_{layer}}$$

Figure 2.4 Detail of an intercalated clay for estimating its tensile modulus

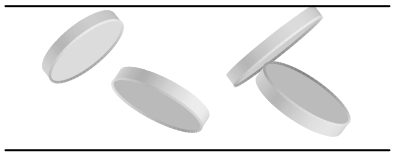

Figure 2.5 Randomly oriented layers in the polymer, $E_{ran-3D}^{layer} = 0.49E_{//} + 0.51E_{\perp}$

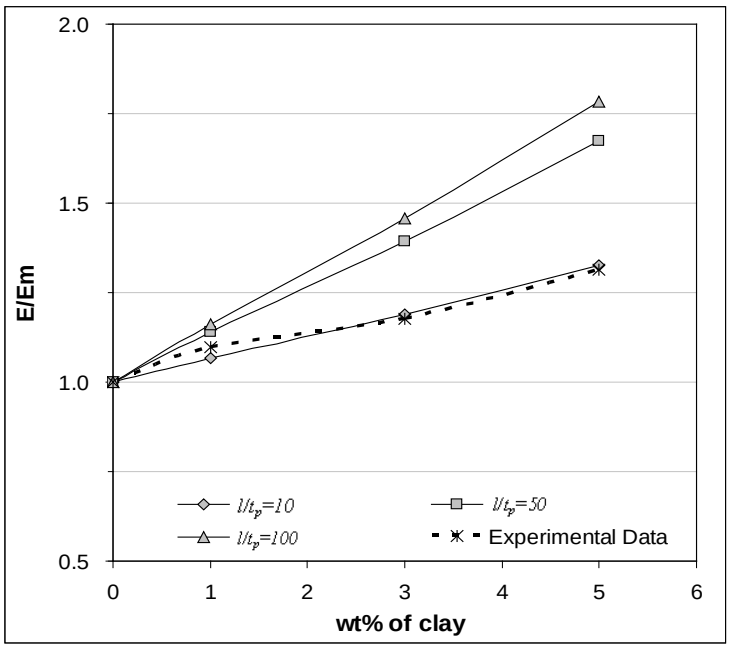

Figure 2.6 The relative moduli of recycled PET nanocomposites as a function of wt% clay [47] compared with the relative moduli calculated by using the Halpin-Tsai Eq. (2.17) with different aspect ratios (*l*/*t*).

Figure 2.6 compares experimental data of the relative moduli as a function of the wt% clay for recycled PET-Cloisite 25A nanocomposites [46] with the Halpin-Tsai calculation, equation (2.17) and (2.20), using aspect ratios between 10 and 100. The recycled nanocomposites had an interlayer distance (d_{001}) of 3.2nm as shown in Table 1.3, so ϕ_{MMT} was estimated using equation (2.23) to be ϕ_{MMT} ~ 0.94nm/3.2nm = 0.293, where 0.94nm is the thickness of a single clay layer. The modulus of an incompletely exfoliated clay particle is estimated by using equation (2.25), so E_f = ϕ_{MMT} x E_{MMT} = 0.293 x 178GPa = 52.3GPa. The value of E_m is 2.55GPa for the recycled PET. In Figure 2.6, the experimental data is close to the Halpin-Tsai prediction at the aspect ratio of 10. It indicates that Halpin-Tsai model can predict the unexfoliated morphology of recycled PET nanocomposites. A fully exfoliated system such as PA6 nanocomposites exhibits an aspect ratio of 50-100 [64]. With an aspect ratio of 50-100, the Halpin-Tsai model estimates the relative modulus of the PET nanocomposites to be in the range of 1.7 to 1.8 at 5 wt% clay loading.

2.4 Crystallization state of PET/organoclay nanocomposites

The presence of a high degree of crystallinity with small and regular spherulites in injection moulded PET parts in Figure 2.7(a) enhances mechanical properties compared to PET with large and irregular spherulites [68]. However, PET has a relatively slow crystallization rate and consequently requires a long cycle time to obtain high level crystallinity that could result in a high modulus but lower impact strength. Effective nucleating agents for PET are added to induce a small and regular spherulitic structure and to increase the crystallization rate.

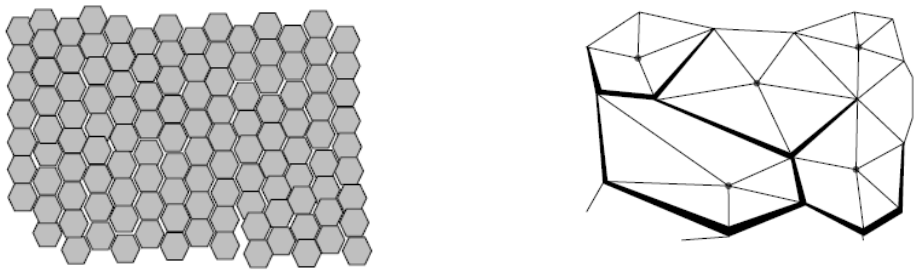

a b

Figure 2.7 Spherulitic structure of PET (a) with and (b) without nucleating agent [68]

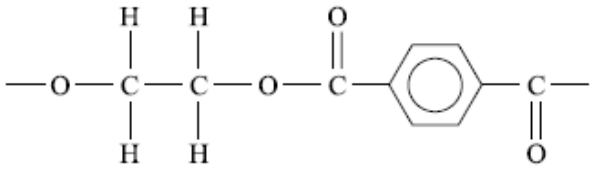

Figure 2.8 repeat unit of PET [69]

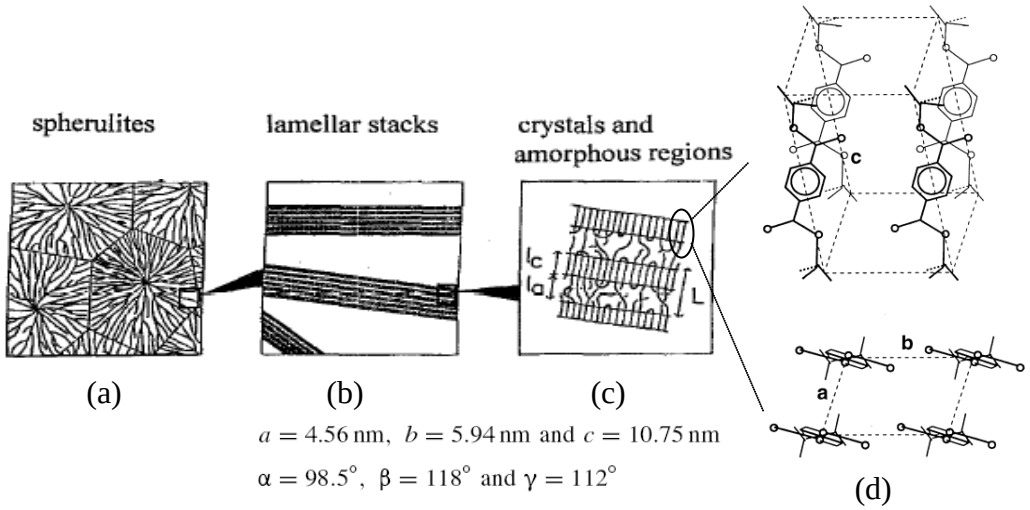

Figure 2.9 Schematic diagram of the spherulites, showing macro scale structure (a), the arrangement of fibrils (b), the chain folding with amorphous material between the lamellar stacks (c), and the PET triclinic structure of the folded chains within the unit cell and the unit dimension (d) [70,71]

Many research groups have prepared PET/clay nanocomposites and investigated the crystallization kinetics. It was found that the introduction of nanoclay into PET can act as an effective heterogeneous nucleating agent by increasing the crystallization rate [34,72].

The chemical formula of the repeat unit in a PET molecular chain is shown in Figure 2.8. The combination of the aromatic rings and short aliphatic chains provides a relatively high modulus, in relation to more aliphatic structures such as a polyolefin and polyamide. PET can be processed into an amorphous or semicrystalline form. In the semicrystalline state, the PET molecular chains fold back and forth on themselves to form the crystal structure with a triclinic unit cell as seen in Figure 2.9(d). In Figure 2.9(c), the chain-folded crystals also form stacks of lamellae that are separated by non-crystalline materials (or tie molecules) to form the semicrystalline structure of the polymer.

When PET crystallizes from the melt or from the glassy state, there are two processes involved, the formation of nuclei and then the growth of the crystals around the nuclei to form a spherulitic structure. In Figure 2.9(b), each spherulite consists of many lamellae crystals growing radially from the central nucleus outward. The spherulites stop growing when they impinge on each other, forming the clear boundary lines or impingements as shown in Figure 2.9(a).

The crystallization process is usually separated into two main stages, primary and secondary crystallization. The primary crystallization ends when the spherulites start to impinge on each other. This is followed by the secondary process that has a much slower crystallization rate. The primary crystallization kinetics of the PET from the melt or glassy state under isothermal conditions is usually represented by the Avrami equation [73,74].

$$1 - X(t) = \exp(-Kt^n) \tag{2.29}$$

where *X(t)* is the relative crystallinity at time *t*, *K* is the overall crystallization rate constant, and *n*, the Avrami constant that is generally an integer between 1 and 4 depending on the nucleation mechanism and growth dimensions (Table 2.1). The value of *n* and *K* are generally obtained from the following logarithmic form of the equation (2.29).

$$\log[-\ln(1 - X(t)] = \log K + n \log t \tag{2.30}$$

The overall crystallization rate (*K*) is composed of two elements, the rate of nucleation and the rate of crystal growth. Each of these can dominate the rate of crystallization. Generally, there are two types of nucleation, heterogeneous and homogeneous. Heterogeneous nucleation occurs instantaneously at the beginning of crystallization on the surface of foreign particles or containing materials while homogeneous nucleation takes place spontaneously in the body of the melt continuously through the crystallization process. With homogeneous nucleation, the crystallization rate is mainly controlled by the nucleation growth rate rather than the crystal growth rate. Conversely, with heterogeneous nucleation, the crystallization rate is mainly controlled by the crystal growth rate.

From Table 2.2, the *n* values are in the range of 3.1-3.4 for the neat PET, and reduce to the range of 2.1-2.6 for the nanocomposites. The Avrami constant states in Table 2.1 that when *n* is 3 this indicates the crystallization mechanism is a three-dimensional growth from instantaneous nucleation or two-dimensional growth from sporadic nucleation. Hsu et al. [75] demonstrated that the spherulites grew from residual unmelted PET which acts as instantaneous nuclei. Therefore, for *n* = 3, the crystals of the neat PET should be three dimensional spherulites rather than two-

dimensional disks. When MMT clay was introduced into PET, *n* decreased from 3 to 2 [72]. This indicated that the crystallization mechanism was two-dimensional growth from instantaneous nucleation.

Table 2.1 Avrami exponent for various types of nucleation and growth [76]

Avrami constant	Growth dimension	Nucleation mechanism
3+1 = 4	Spherulite growth (3)	Sporadic nuclei (1)
3+0 = 3	Spherulite growth (3)	Instantaneous nuclei (0)
2+1= 3	Disk-like growth (2)	Sporadic nuclei (1)
2+0 = 2	Disk-like growth (2)	Instantaneous nuclei (0)
1+1 = 2	Rod-like growth (1)	Sporadic nuclei (1)
1+0 = 1	Rod-like growth (1)	Instantaneous nuclei (0)

Note. The instantaneous (heterogeneous) nuclei make all the crystals start growing at the same time, while for the sporadic (homogeneous) nuclei, new crystals grow throughout the crystallization process

Table 2.2 Avrami constant and relative $t_{1/2}$ for PET containing nanoparticles under isothermal crystallization from the melt state

Filled and unfilled PET	*n*	Temperature (°C)	Relative $(t_{1/2})^{-1}$	Ref.
PET	3.1-3.3	210-218	-	
PET + 3 wt% modified-MMT (In-situ polymerization process)	2.1-2.3	220-230	-	[72]
PET	3.1-3.4	208-223	1.0	
PET + 4 wt% ME (fluorine mica) (In-situ polymerization process)	2.6-2.3	208-223	1.8	[77]
PET	-	194	1.0	[34]
PET + 5 wt% organoclay	-	194	3.0	
PET	-	220	1.0	
PET + 5 wt% Cloisite Na^+	-	220	4.5	[51]
PET + 5 wt% 10A	-	220	4.0	
PET + 5 wt% 15A	-	220	1.5	

The crystallization rate can be evaluated by the crystallization half-time ($t_{1/2}$) in which *X(t)* is 50% of the maximum possible crystallinity and can be calculated from the following equation,

$$t_{1/2} = \left(\frac{\ln 2}{K}\right)^{1/n} \tag{2.30}$$

The values of the relative half-time crystallization, listed in Table 2.2, for all nanocomposites are lower than those of neat PET. The lower the values of half time, the higher the crystallization rate. The values of the relative $(t_{1/2})^{-1}$ indicate that the nanocomposites exhibit a higher crystallization rate than the neat PET. In addition, the crystallization rate of the composites depends on the chemical structure of the surfactant.

The influence of the nanoparticles on the crystal structure and crystallinity of PET was further investigated by using wide angle x-ray scattering (WAXS) [72,78]. The WAXS results in Figure 2.10 show that the crystal unit cell of PET is not affected by the presence of nanoparticles.

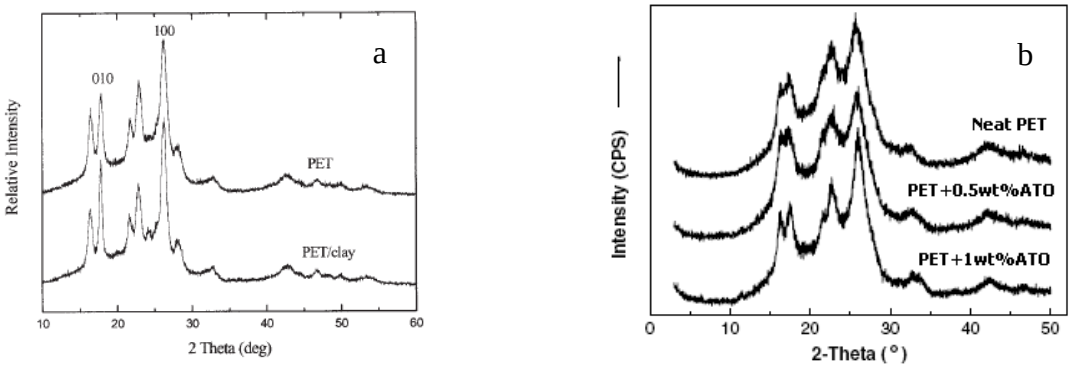

Figure 2.10 WAXS patterns of (a) neat PET and PET/clay nanocomposites isothermally crystallized at 226°C [72] and (b) neat PET and PET containing different content of antimony tin oxide (ATO) isothermally crystallized at 194°C [78].

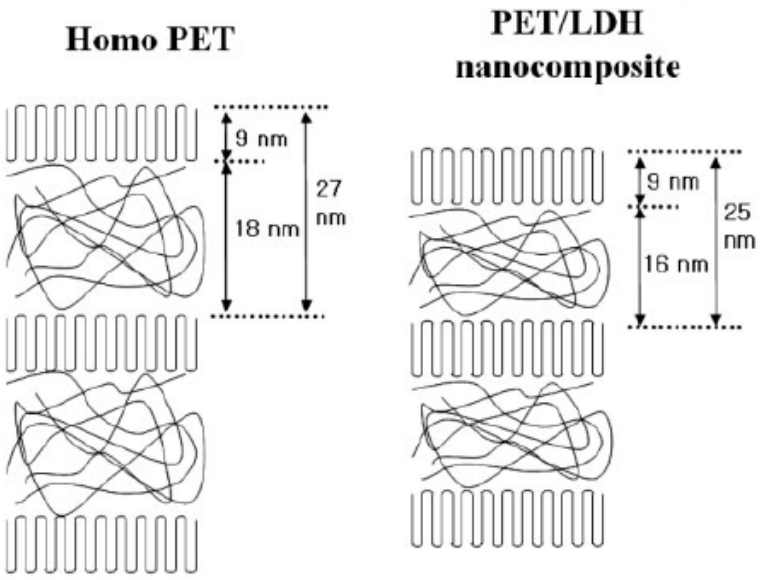

Figure 2.11 Schematic diagram of lamellar structures for the isothermally crystallized PET and PET/LDH nanocomposite [79].

In 2007, Lee and Im [79] prepared PET nanocomposites containing layered double hydroxide (LDH) and investigated the changes of lamellar stack parameters of the PET in the nanocomposites, including long period (L), lamellar thickness (l_c), and amorphous thickness (l_a) as shown in Figure 2.9(c). It was found that the L and l_a decreased with increasing LDH loading, while l_c did not change as shown in Figure 2.11. The decrease of l_a possibly led to the reduction of amorphous phase or tie molecules that connect the lamellar stacks [80].

2.5 Conclusion

The PET/organoclay nanocomposites will be developed by solvent blending and melt blending. The thesis focuses on the effect of the dispersed nanoclay on the rheology, tensile properties and crystallization behaviour of PET nanocomposites. The degree of nanoclay dispersion in the polymer matrix is the key factor to enhance the properties of the material. The different level of the nanoclay dispersion is related to the

rheological and tensile properties. The modulus of the nanocomposite is compared to the value predicted by the Halpin Tsai equation. The effect of the percolated nanoclay network on the tensile properties of the nanocomposite is also investigated. The investigation of the relationship between the spherulitic microstructure and the mechanical properties of the unfilled and filled PET based on nanoclay is discussed. The effect of two organoclays with different amounts of surfactant on the isothermal melt-crystallization kinetics of the nanocomposite is studied using the Avrami equation.

Chapter 3

Experimental

3.1 Introduction

This chapter describes the materials and experimental methods used in the preparation of PET-organoclay nanocomposites via solvent blending and melt blending.

3.2 Materials

The two PET resins used were (a) virgin PET with IV of 0.54 dL/g and (b) with IV of 0.75 dL/g. These polymers were kindly supplied by Wellman International Ltd., Ireland. The four commercial organoclays used were all based on montmorillonite. Nanofil-2 and SE3010 were kindly supplied by Süd-Chemie, Germany. Cloisite 10A and Cloisite 15A were supplied by Southern Clay Products, Texas, USA. Phenol (detached crystals), chloroform 99+%, Trifluoroacetic acid (TFA) were purchased from Fisher Scientific U.K. Ltd. Epoxy (Bisphenol A diglycidyl ether with equivalent weight of 172-176 g/eq) was purchased from Sigma-Aldrich Co. U.K.

3.3 Solvent blending

The organoclays and PET (IV of 0.75 dL/g) were dried at 80°C and at 120°C respectively in an oven for 24 hours. The nanocomposites were produced by blending the organoclay with ground PET in a mixture of phenol and chloroform. Initially, the organoclay was blended with the solvent using a magnetic stirrer until the solution became clear. Samples of the mixture of organoclay and solvent were then subjected to ultrasonic vibrations with a frequency of 33 kHz (using an Ultrasonic bath

Fisherbrand FB11022) for a range of set times at room temperature. After sonication, the finely ground PET was added to the mixture. This was stirred into the suspension at 70°C for 3 hours or until the resin was completely dissolved. The homogeneous solution was then dried at 80°C in a vacuum oven for 72 hours to extract the phenol and chloroform.

3.4 Melt blending

The organoclays and PET (IV of 0.54 dL/g) were dried at 80°C and at 120°C respectively in an oven for 24 hours. The PET was blended with 2.5 wt% of the organoclay in a co-rotating intermeshing 40 mm diameter twin screw extruder and the modular screws were assembled with a semi severe screw profile and a devolatilisation zone three quarters down stream. The extrusion blending was carried out with barrel temperatures of 240, 245, 250, 255, 260, 265°C, from the hopper to the die and a screw speed of 350 rpm. The PET compound was extruded through a 6 mm die and pelletized.

3.5 Scanning Electron Microscopy (SEM)

The structures of the solvent blended and melt blended samples were observed on the sample surface and a fracture surface as shown in Figure 3.1. This figure shows how SEM samples were fractured from the cast films of the solvent blended samples (Figure 3.1(a)) and from compression films of the melt blended samples (Figure 3.1(b)). The dispersion of the layered clay in the PET was examined by using, a Zeiss Supra 35VP instrument at 12kV accelerating voltage. The sample surfaces of the composites were prepared for examination by etching under a vacuum in an oxygen

plasma for 8 minutes at 75 watts. This treatment removed a small amount of the surface layers of the composite samples and clearly revealed the 3-D dispersion of clay particles in the PET. The etched surfaces were coated with gold using sputter coater for 30 seconds prior the SEM observation.

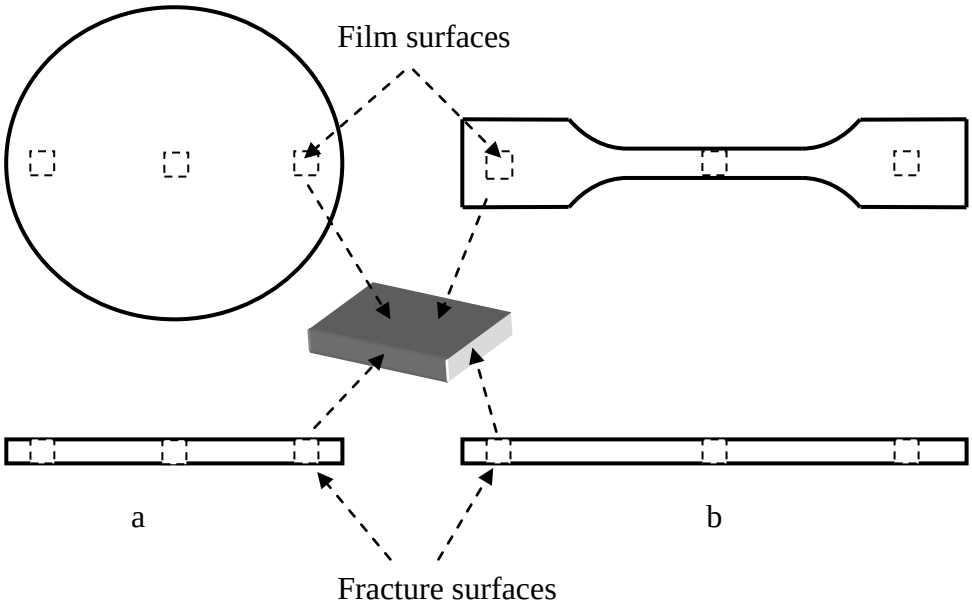

Figure 3.1 Illustrations of SEM sampling sites for (a) solvent blended film and (b) melt blended tensile film cut from a compression moulded film.

To observe spherulitic microstructures, the samples were etched with a solution of potassium hydroxide/methanol (5/95 by weight) for 1 hour. The etched samples were sputter coated with gold and then observed in the SEM. The test details are summarized below.

Oxygen plasma etching equipment	K1050X Plasma Asher
Etching time	8 minutes
Etching power:	75 watts
Coating equipment	SC7640 Sputter Coater
Coating	Platinum/Gold
Coating time	30 seconds
SEM instrument	Zeiss Supra 35VP
Accelerating Voltage	12 kV
Working distance	5-7 mm
Detectors	Secondary Electron
Magnification:	500x-100000x
Aperture size:	30
Minimum sample number	2

3.6 Transmission Electron Microscopy (TEM)

Nanocomposite samples were embedded in epoxy resin and then sectioned using a microtome with a glass knife at room temperature to obtain section 150 nm thick. After sectioning, the ultra-thin sections were floated onto water and were collected onto 200 mesh copper grids. These observations were carried out in a JEOL 2000FX TEM with an accelerating voltage of 100kV as detailed below.

TEM instrument	JEOL 2000Fx
TEM CCD camera	ORIUS 600
Accelerating voltage	80
Magnification	3000x and 10000x
Minimum sample number	2

3.7 Polarized Light Microscopy (PLM)

PLM observations were carried out using a Zeiss-Axioskop-2 microscope using 10x and 20x objective lenses. Thin films with an average thickness of 0.06 mm were produced by a similar method as that used for the preparation of tensile specimens. The granules were dried under a vacuum at 120°C for 24 hours. The granules were melted and compressed between polyimide films at 280°C for three minutes to

remove any previous thermal history. In order to obtain the films with different levels of crystallinity, some of the melt films were then cooled at a rate of 40 °C/min to a temperature of 215, 210 or 200°C and then rapidly quenched. Others were cooled down to 200°C at 40 °C/min and then allow to crystallize for 10 minutes before quenching to room temperature. The test details are shown below.

POM instrument	Zeiss-Axioskop-2
Magnification	10x and 20x
Minimum sample number	2

3.8 Rheological Measurement

All of the rheology properties were measured using a dynamic rheometer manufactured by TA instrument (Advanced Rheometer Expansion System or ARES). The test samples were dried under a vacuum at 120°C for 24h. Measurements were conducted between a pair of 25 mm diameter parallel plates with a constant gap spacing of 0.5 mm at 270°C. Although the shear rate in the parallel-plate system is not constant as that in the cone-plate system, the rheological results from the former system can be used to compare the degree of clay dispersion of the nanocomposites. A 350 mg sample was first placed in the preheated parallel-plate fixture at temperature 255°C and then the gap setting was adjusted to about 0.7 mm by squeezing the sample. Immediately, the temperature was increased to 270°C and then the gap was gradually decreased to the desired distance of 0.5 mm.

Prior to the dynamic frequency sweep tests, dynamic strain sweep tests were performed to determine the linear viscoelastic region of the samples. The dynamic strain sweep was carried out at 270°C at 5 Hz in the range of 0.1-100% strain. From this, the strain amplitude for the dynamic frequency sweep tests was chosen from the

strain limit under which *G′* remained constant. The strain amplitudes determined were 10% for the PET with IV of 0.54 dL/g (chapter 5) and 1% for the PET with IV of 0.75 dL/g (chapter 4) to keep the dynamic frequency sweep measurements within the linear viscoelastic range over the frequency range 0.1-500 rad/s in a dry air environment.

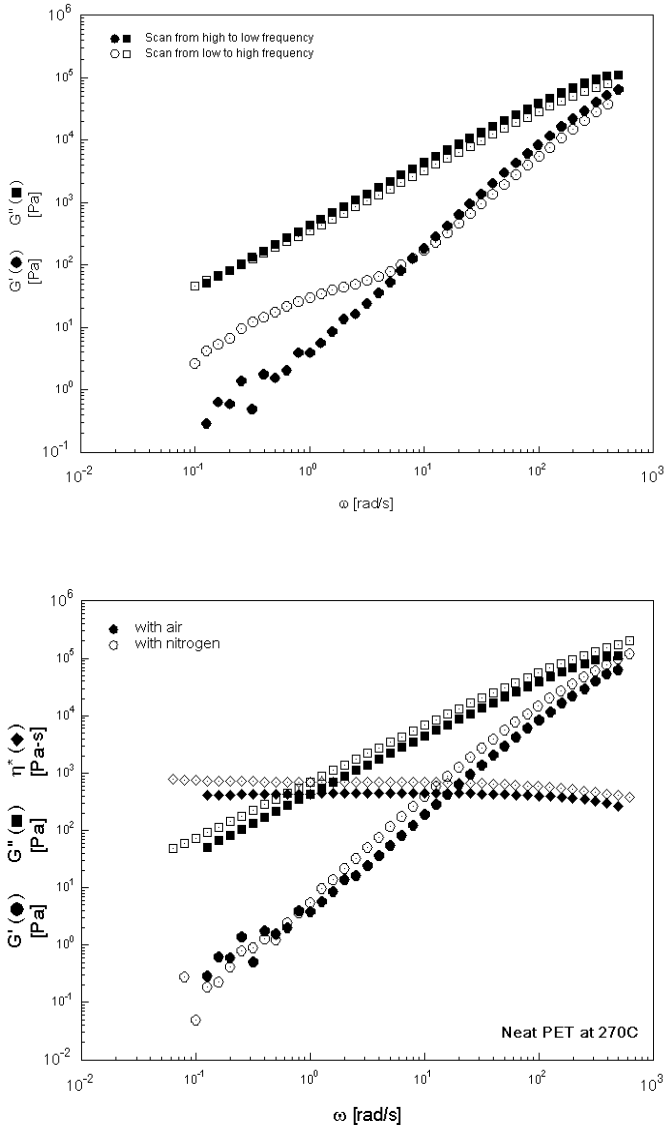

Figure 3.2 Comparisons of the rheological responses of the neat PET (a) between the low-to-high and high-to-low frequency sweep and (b) of high-to-low frequency sweep under a nitrogen and dry air atmosphere.

Because all measurements were conducted in a dry air environment, thermo-oxidative degradation in PET occurred over the time during the dynamic frequency sweep test. The change of PET structure due to the degradation was inevitable and greatly affected the rheological results. In order to reduce the effect of the thermally oxidative degradation as much as possible, the measurements needed to be carried out under a nitrogen atmosphere and scanned from high to low frequency. Unfortunately, it was not possible to make the measurements in the nitrogen atmosphere because the ARES instrument in this laboratory was unable to be operated with a nitrogen atmosphere. This study, therefore, performed the tests by scanning from high to low frequency in a dry air environment.

Figure 3.2(a) shows the rheological results of the tests with different frequency scanning directions, low to high frequency sweep (L-H) and high to low frequency sweep (H-L). At the low frequencies, G' from the L-H sweep test was significant greater than that from the H-L sweep test due to the PET degradation. Generally, the measurement took a long time at low frequencies and a short time at high frequencies. The L-H sweep measurement started at the low frequency that took a longer measuring time at the beginning of the run. This run resulted in the severe degradation of the polymer matrix due to the long measuring time at the beginning of the measurement. On the other hand, the H-L sweep measurement took a shorter measuring time at the beginning of the run that resulted in a lower degradation of the polymer matrix. Figure 3.2(b) shows the rheological results of the H-L sweep tests under nitrogen and dry air. The measurements in the dry air and nitrogen atmosphere showed a slight difference in G' and G''. It suggested that the high to low frequency scan in the dry air environment significantly reduced the effect of thermo-oxidative

degradation of PET on the rheological measurement. The table below shows the details of the measurement.

Rheological instrument	Advanced Rheometric Expansion System (ARES)
Plate geometry	∅25 mm Parallel plates
Gap	0.5 mm
Temperature	270°C
Small strain amplitude	1% for PET with IV of 0.54 dL/g 10% for PET with IV of 0.75 dL/g
Frequency sweep range	500-0.1 rad/s (Scan from high to low frequency)
Atmosphere	Dry-air
Minimum sample number	2

3.9 Intrinsic viscosity (IV)

The polymer degradation during melt blending was evaluated by measurements of intrinsic viscosity according to ASTM D4603 standard. The IV was estimated from a single point measurement of relative viscosity (η_{rel}) and using the equation (3.1). A mixture of phenol and 1,1,2,2-tetrachloroethane (1:1 by weight) was used as the solvent for the neat PET, the extruded PET and the nanocomposites. The samples were previously ground to accelerate the dissolution and were dried in an oven for 24 hours at 120°C before dissolving. The solutions with a concentration of 0.5 g/dL were prepared by dissolving the ground samples at 70°C in the solvent mixture. The nanocomposite solutions were centrifuged for 30 minutes at 3500 rpm and filtered to remove the nanoclay sediment. The measurements of the IV of the nanocomposite samples were, therefore, not affected by the nanoclay. The relative viscosity of the solution was determined using an Ubbelohde viscometer at 30°C. The flow time of the pure solvent and the sample solution was measured and used to evaluate the relative and intrinsic viscosities.

$$\eta_{rel} = t_1 / t_0$$

$$IV = (1/c)[2(\eta_{rel} - 1) - 2\ln(\eta_{rel})]^{1/2} \qquad (3.1)$$

where t_1 is the average flow time of polymer solution (s), t_0 is the average flow time of pure solvent mixture (s) and c is the polymer solution concentration (g/dL). The test details are shown below.

Glass capillary Viscometer	Cannon-Ubbelohde Type 1B
Solvent	60/40 w % mixture of phenol and 1,1,2,2-tetrachloroethane
Solution concentration	0.5 g/dL
Testing temperature	30°C
Sample size	25 ml
Minimum number of sample	2

3.10 Tensile Test

Tensile specimens were obtained by compression moulding. The PET granules were placed between polyimide films and heated between metal platens to the desired melting temperature (255, 260, 270 and 280°C) and kept at this temperature for two minutes. The melt was then pressed for three minutes to get a uniform thickness of about 0.15 mm. The amorphous samples were obtained by rapidly quenching the molten films. To produce the semicrystalline films, the molten films were cooled to the desired crystallization temperature (200°C) with cooling rate of 40 °C/min, and held at this temperature for 10 minutes and then immediately quenched to room temperature. Dog-bone shaped samples for tensile test were cut from the compression moulded films. Mechanical testing was carried out on a Hounsfield H10KT tensile testing machine. The specimens had a gauge length of 25 mm, a width of 4 mm and a thickness of 0.15 mm. The cross head speed was set at five mm/min with a pre-load of

1 N. The tests were carried out in an air conditioned room at 23°C and a relative humidity of 43%. The tensile modulus was calculated between 0.05 to 0.25% strain values. At least seven specimens of each sample were measured following ASTM D882-02. The test details are summarised below.

Tensile machine	Hounsfield H10KT
Load cell	10 kN
Sample size	50 x 4 x 0.15 mm
Gauge length	25 mm
Cross head speed	5 mm/min
Pre-load	1 N
Minimum number of specimen	7

3.11 Thermo Gravimetric Analysis (TGA)

Thermo gravimetric analysis tests were carried out on the samples of the organoclay under a nitrogen flow of 50 mL/min using a TA Instruments (TGA500) to determine their thermal stability. All of the samples were heated up to 800°C at heating rate of 20 °C/min. Evaluation was carried out using Universal Analysis 2000 V4.3. The details are summarized below.

TGA instrument	TA instruments TA Q500
Inert Gas	Nitrogen
Gas flow rate	50 mL/min
Heating range	35-280°C
Heating rate	20° C/min
Minimum sample number	2

3.12 Differential Scanning Calorimetry (DSC)

DSC analyses were carried out using a TA instruments DSC Q1000. The test samples were dried under a vacuum at 120°C for 24h. The dried samples were encapsulated in aluminium pans and placed in the DSC cell. Initially, the samples were heated and

kept at 280°C for 5 minutes under nitrogen to destroy their prior thermal history. They were then quickly removed from the cell and quenched in an aluminium block. The samples were then run through a heat/cool/heat program to examine their thermal properties. In the first heating scan, all of the samples were heated to 280°C at a ramp rate of 10°C/min under a nitrogen atmosphere. Afterwards, the cooling trace was recorded from 280°C to 30°C at rate of 10 °C/min. This was following by the second heating scan at rate of 10 °C/min. The percentage crystallinity (X_c) for neat PET and PET nanocomposites was calculated from the following equation.

$$X_c(wt\%) = 100\frac{\Delta H_m - |\Delta H_c|}{\Delta H_m^0}$$

where ΔH_m^0 of 136 J/g is the heat of fusion of a 100% crystalline PET [81], ΔH_m is heat of fusion and ΔH_c is cold-crystallization heat.

Isothermal hot-crystallization experiments were performed in the temperature range 183-224°C. The samples were melted at 280°C for five minutes to remove thermal history. The melt samples were then cooled at a rate of 80 °C/min to the desired crystallization temperature and kept at that temperature for ten minutes. Evaluation was carried out using Universal Analysis 2000 V4.3. The conditions of the test are summarised below.

DSC instrument	TA instruments DSC Q1000
Sample weight	5-8 mg
Inert Gas	Nitrogen
Gas flow rate	50 mL/min
Heating range	35-280°C
Holding time	5 minute at 280°C
Heating and Cooling rate	10 °C/min
Minimum sample number	3

Chapter 4

PET/organoclay nanocomposites by solvent blending

4.1 Introduction

One of the most important issues in polymer/clay nanocomposites must be the problem of how to break down stacks of clay layers into single layers and disperse them throughout the polymer blend. The fully dispersed/exfoliated nanoclay in PET would greatly improve the properties of the nanocomposites. A major challenge with PET/clay nanocomposites is to achieve a high degree of exfoliation in a matrix that has a lack of polar groups in the chemical structure, such as -COOH and –OH [82]. Although in situ polymerization usually provides fully exfoliated clay nanocomposites, PET/clay nanocomposites via this method have only exhibited a partially exfoliated structure, as evidenced by XRD results [37]. So far, no research group has claimed to produce fully exfoliated nanoclay/PET composites as have been reported for the PA-6/ [83] and polypropylene/ [54] clay nanocomposites that are commercially available.

Solvent blending has been a widely used technique to prepare polymer-organoclay nanocomposites and is one of the methods that consistently provides exfoliated clay nanocomposites [15,84-89]. The organoclay in the solvent is usually subjected to ultrasonication in order to improve the separation and dispersion of the clay before adding the polymer. Morgan and Harris [90] reported a synthesis of organoclay/polystyrene (PS) nanocomposites via the solution intercalation route aided by sonication. It was found that sonication during the solvent blending produced an

exfoliated PS/organoclay nanocomposite. Chen and Tolle [91] reported the preparation of epoxy/organoclay nanocomposites via solution blending in acetone with a combination of high-shear mixing and ultrasonication at 50°C for 6-7 hours. Using this technique, their epoxy/clay nanocomposites exhibited a fully exfoliated structure.

Epoxy of diglycidyl ether of bisphenol A (DGEBA) has been widely used as a compatibilizer to enhance the separation and the dispersion of organoclay in Poly(butylene terephthalate) (PBT) [92,93] and poly(ethylene terephthalate-co-ethylene naphthalate) (PETN) [94] nanocomposites. The dispersion of an organoclay in epoxy via solvent blending with ultrasonication for several hours before adding PET should lead to a fully exfoliated clay PET nanocomposite. Although this blending method is not practical, it is useful in the research and development of new materials.

The objective of this work was to produce a fully exfoliated organoclay PET nanocomposite. The effects of sonication time, a compatibilizer, organic modifiers, and the percentage of organoclay on the morphological, rheological, mechanical, and thermal properties were studied. The structure-rheological behaviour and the relationship between a clay network structure and tensile properties were also investigated. The effect of residual solvent on the crystallization of cast filled and unfilled system was also investigated.

4.2 Exfoliation of organoclay in the PET matrix

4.2.1 Preliminary experiments

During the preliminary studies, a solvent blending technique with ultrasonication was optimized for the preparation of exfoliated clay based PET nanocomposites. The sonication time strongly affects the separation and dispersion of the organoclays in polymer matrices [90,91,95]. Hence, the effects of the sonication time and degree of dispersion of the organoclay were initially investigated. 5 wt% of Cloisite 10A (10A), was added and stirred in a mixture of phenol and chloroform (3:1 by weight) [32] and then sonicated for different times. Ground PET (IV of 0.75 dL/g) was then added and dissolved in the organoclay suspension at 70-80°C for three hours. The nanocomposite suspension was dried in a vacuum oven at 80°C for 48 hours or longer if necessary to extract the phenol and the chloroform and to obtain the nanocomposite films.

The degree of the clay dispersion in the nanocomposite films was observed using SEM. The SEM results showed the degree of separation and distribution of the clay particles in the matrix with different sonication times. It was clearly observed that the clay dispersion strongly depended on the length of the sonication times as shown in Figure 4.1. Figure 4.1(d) reveals that sonication for 60 minutes greatly separated the large clay particles into thin stacks of clay layers. The thin stacks were, however, not uniformly dispersed. It appeared, therefore, that for further dispersion of the particles a longer sonication time was necessary.

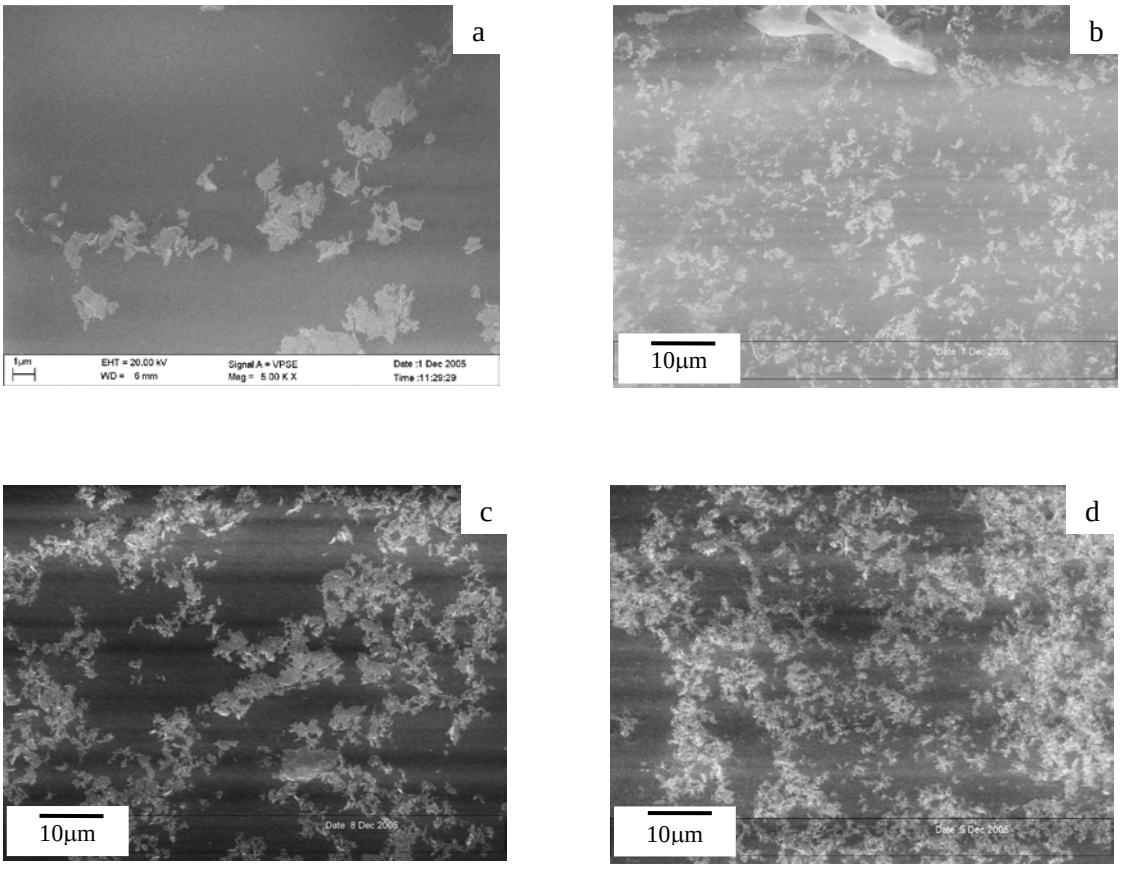

Figure 4.1 SEM images of PET nanocomposites containing 5 wt% of 10A by solution blending with sonication times of (a) 10, (b) 15, (c) 30, and (d) 60 minutes.

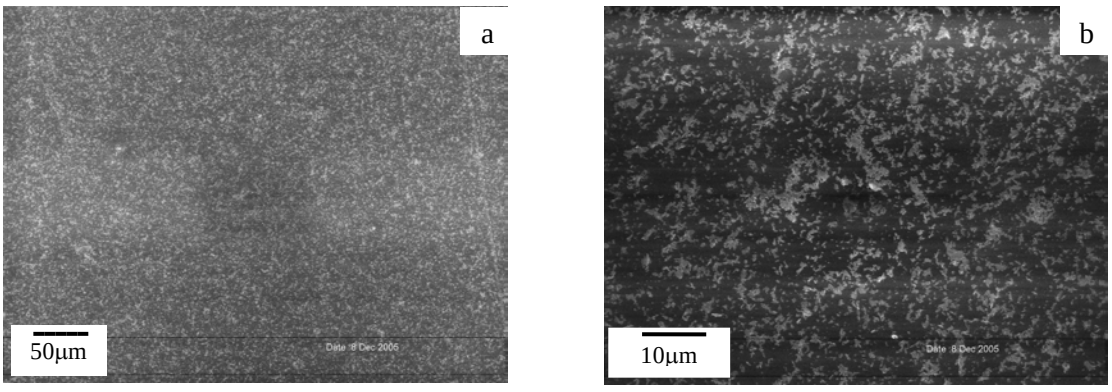

Figure 4.2 SEM images of PET nanocomposite containing 5 wt% of 10A by solution blending with sonication for 5 minutes before and after addition of PET at (a) low and (b) high magnification

Figure 4.2 shows SEM images of the nanocomposite sample with a 5-minute sonication before and after the addition of PET. The low magnification image in Figure 4.2(a) shows clay particles that are more uniformly dispersed throughout the matrix compared with the images in Figure 4.1. This indicated that sonication after adding the PET provided a uniform distribution of the clay particles. The higher magnification image in Figure 4.2(b), however, shows that the average distance between the clay particles was still in the micron scale. The reason for this is that 5-minute sonication before adding the PET was not sufficient to break down the large stacks of clay to thin particles or individual layers as observed in the 60-minute sonication sample in Figure 4.1(d). A sonication time after the polymer addition should not be too long because it has been reported that the sonication energy could break the polymer molecules and consequently lower the composite properties [90]. Therefore, it was expected that the use of a long sonication time before and short sonication time after the addition of PET would greatly improve the separation and distribution of silicate layers throughout the polymer matrix with a minimum effect on the condition of the matrix.

In the course of these studies, it was found that the phenol/chloroform solvent became dark in colour when the sonication time was longer than ten minutes. This result corresponded with recent work [96] indicating that the addition of carbon tetrachloride (CCl_4) increased the rate of the ultrasonic degradation of phenol. Since carbon tetrachloride and chloroform (trichloromethane, $CHCl_3$) have similar chemical compositions, logically chloroform might also enhance the rate of degradation of phenol. It was the degradation of phenol during sonication that gave the dark colouration in the final product. To avoid the phenol degradation, the organoclay was

dispersed by using sonication in chloroform and the small amount of phenol was gradually added during the sonication process.

The solubility of PET in the organoclay suspension depended on the ratio of phenol to chloroform. It has been reported that the ratio of 3:1 by weight of phenol/chloroform will completely dissolve the ground PET after three hours at 70°C [32]. For this study the proportion of phenol to chloroform used was 2:1 in order to limit the degradation of phenol and to minimise the use of phenol. It was found that 25 ml of the 2:1 phenol/chloroform solvent could effectively dissolve three grams of fine ground PET.

In addition to the sonication, it was necessary to use a compatibilizer to improve the dispersion of the organoclay in the PET polymer. It has been reported that the use of an epoxy significantly enhanced the dispersion of organoclay during the preparation of PBT nanocomposites [92]. Hence, this work initially made the effort to improve the dispersion of the organoclay by using the epoxy as a compatibilizer. The epoxy used in this study was diglycidyl ether of bisphenol A (DGEBA) with equivalent weight of 172-176 g/eq. At first 1 wt% of the epoxy and 5 wt% of the 10A were sonicated together in the solution of phenol/chloroform for five minutes before blending with the fine ground PET. The morphology of the samples was observed by SEM and is illustrated in Figures 4.3 and 4.4. It was found that the epoxy significantly improved the dispersion of the organoclay in the PET nanocomposites as evidenced by SEM images. This is because the epoxy molecules with the strong polarity of their epoxide groups can strongly interact with hydroxyl groups at the edges of the clay layers and migrate into the interlayers of the clay particles during the ultrasonication. They also lower the surface energy of clay layers and improve the compatibility between the matrix and clay [97]. It is thought,

therefore, that this enables the PET molecules to intercalate easily into the interlayer and break down the clay aggregates into a large number of small clay particles.

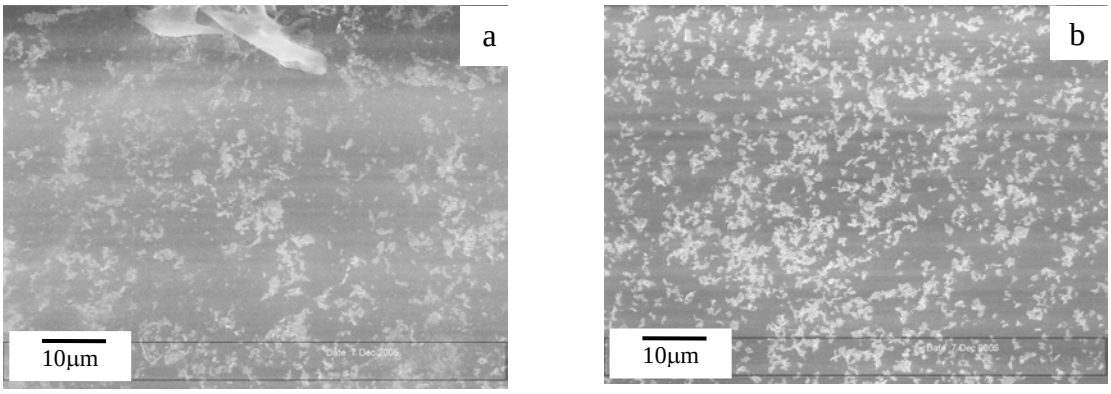

Figure 4.3 SEM images of 5 wt% 10A PET nanocomposites (a) without epoxy and 15-minute sonication (b) with 1 wt% epoxy and 5-minute sonication

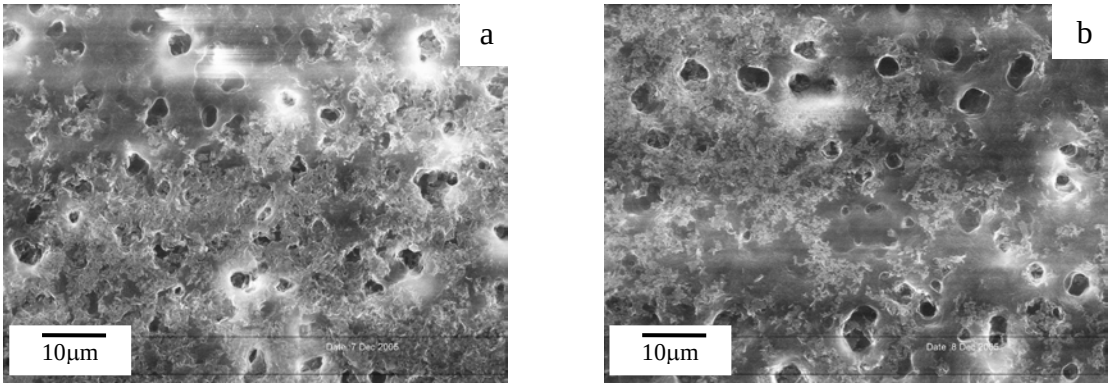

Figure 4.4 SEM images of 5 wt% 10A PET nanocomposites with 2 wt% (a), and 3 wt% epoxy (b) (The samples were sonicated for five minutes before adding PET.)

The effects of the percentage of epoxy on the morphology of the filled PET were initially investigated and the results are shown in Figure 4.4. The increase of the epoxy content from 1 wt% to 3 wt% led to a significant increase in the dispersion of clay. The improvement in the dispersion confirmed that the epoxy increased the compatibility between the 10A and the PET. However, a large numbers of micro-pores (~ ∅3μm) in the matrix occurred when the content of the epoxy was increased.

This would have led to a reduction of the composite properties. Consequently, a 1 wt% epoxy was used to produce the nanocomposites in this research. The theoretical amount of epoxy to be added to the PET was calculated from the following equation:

% epoxy = (Epoxy equivalent weight x 100) / PET equivalent weight

It is assumed that only one carbonyl end group in a PET chain can react with one epoxide group of epoxy. The PET and epoxy have equivalent weight of 23000 g/eq and 172 g/eq respectively. Therefore, the calculated amount of epoxy is (172 x 100)/23000 = 0.75 wt%. This theoretical value was close to the experimental value of 1 wt%

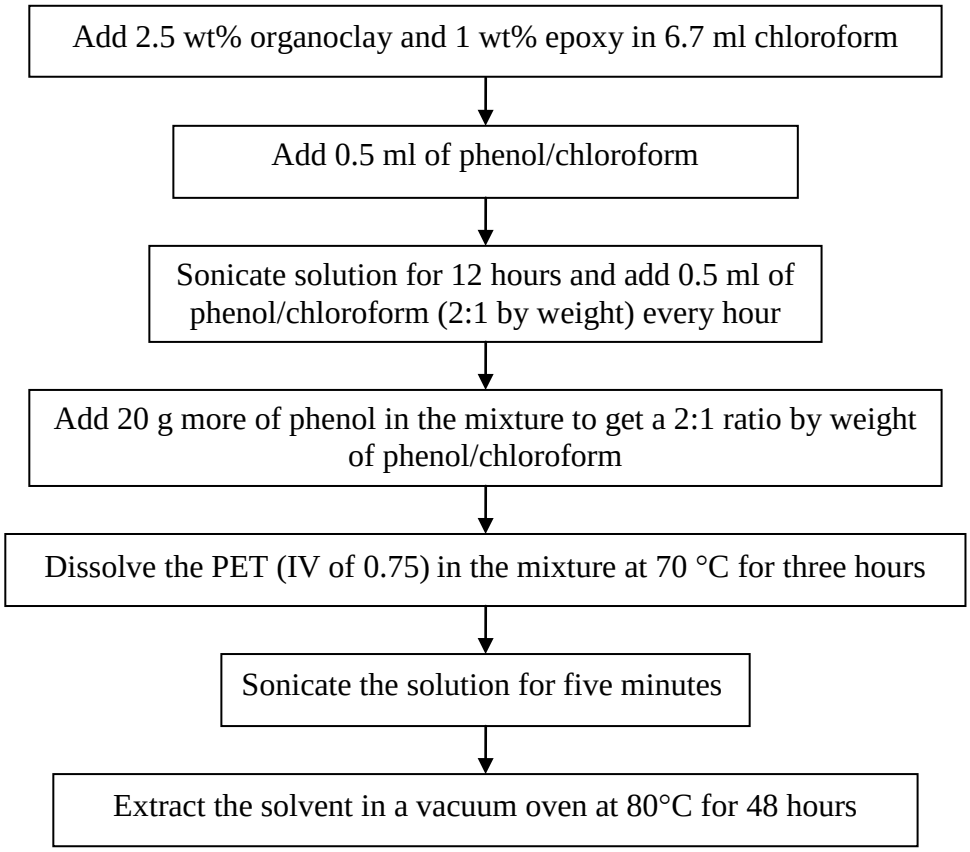

Figure 4.5 Flow diagram of the optimized processing technique for solvent blending to prepare PET nanocomposite based organoclay.

Knowledge from the preliminary experiments was used to establish the optimized processing conditions to prepare the fully exfoliated organoclay (Cloisite 10A) based PET nanocomposites. A flow diagram for the process is shown in Figure 4.5. The quantity of solvent used in the flow diagram was able to prepare not more than three grams of the nanocomposites, which provided the PET solution concentration of about 10 %w/v. Firstly the organoclay and epoxy were added to the chloroform. In order to reduce the phenol degradation and the re-aggregation of the organoclay during sonication for several hours, 0.5ml of a mixture of phenol and chloroform (2:1 by weight) was added every hour. However, by this method some degradation of the phenol was inevitable, and consequently the final product was slightly brown in colour as shown in Figure 4.6(a). The next step was to develop fully exfoliated organoclay nanocomposites by using the optimized processing conditions and to investigate their morphological, rheological and mechanical properties.

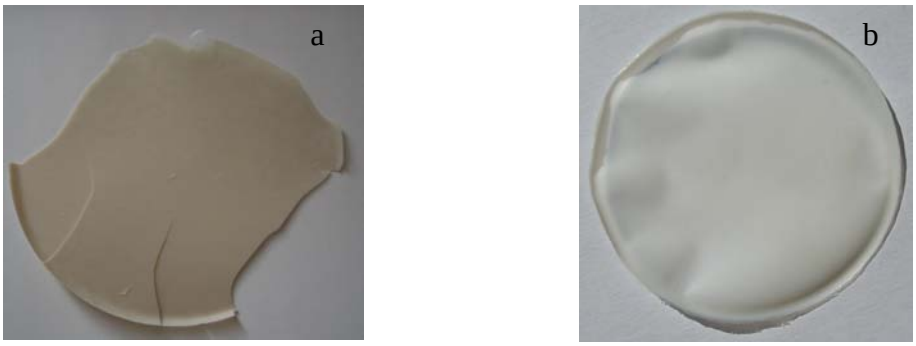

Figure 4.6 Comparison of the colour between the solvent blended PET/clay nanocomposites (a) with sonication for six hours and (b) without sonication.

4.2.2 Morphology

In this section the PET/organoclay nanocomposites were prepared by using the technique shown in Figure 4.5. The degree of the clay dispersion was observed by SEM and TEM. PET nanocomposites based on a 2.5 wt% of 10A were prepared at the different sonication times of one, four, and six hours. Figures 4.7 and 4.8 show SEM images of the film surfaces and the film cross-sections (fracture surfaces), respectively. The detail of the SEM samples of the films and fracture surfaces is shown schematically in Figure 3.1 in chapter 3.

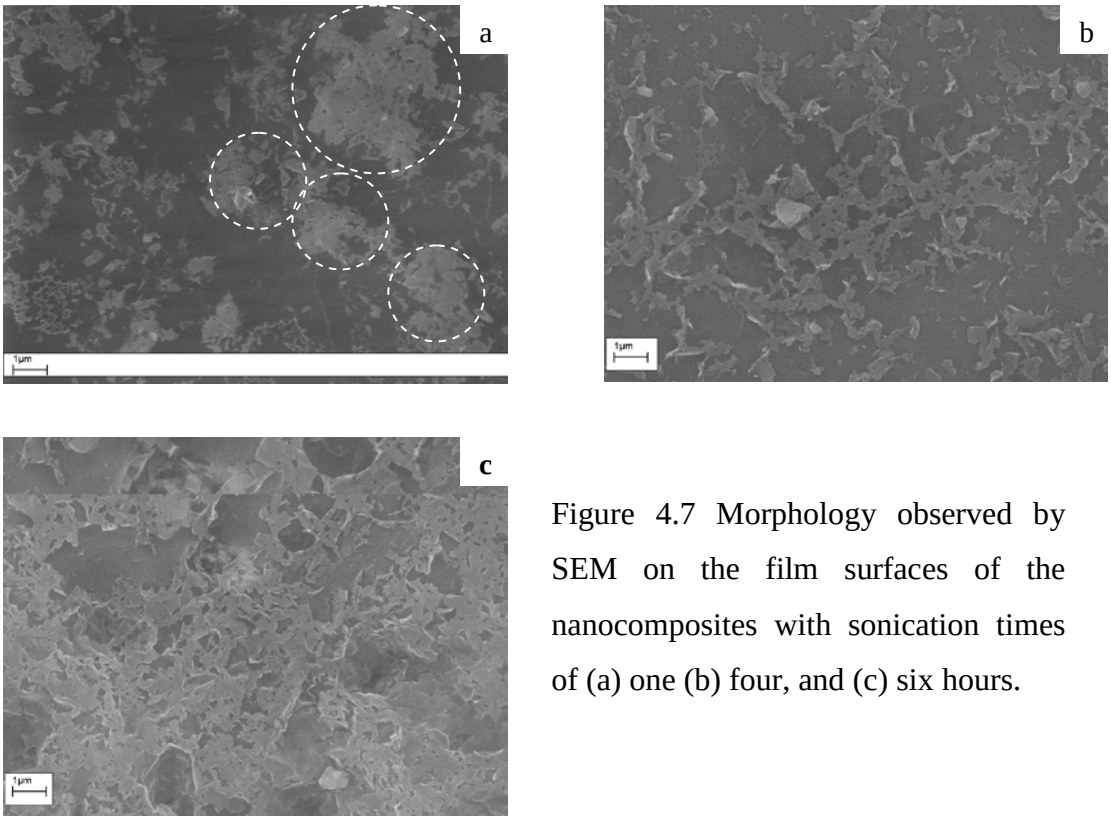

Figure 4.7 Morphology observed by SEM on the film surfaces of the nanocomposites with sonication times of (a) one (b) four, and (c) six hours.

The SEM images of the film surface in Figure 4.7 reveals the planes of clay layers rather than their edges. The light areas are the clay particles, whereas the dark area is the PET matrix. It was not possible to evaluate the thickness of the clay particles using the SEM images of the film surface. The sample subjected to

sonication for one hour exhibited large agglomerates of clay as shown in Figure 4.7(a). The stacks of clay layers were not completely separated and thus formed large groups of particles, as shown in the circles. The increase of the dispersion time to four hours broke the clay agglomerates down further to smaller particles with fewer agglomerates as shown in Figure 4.7(b). When the sonication time was increased to six hours, the number of dispersed particles increased dramatically, resulting in a linked structure of dispersed clay. Consequently the matrix area without clay decreased considerably as shown in Figure 4.7(c). These processing conditions induced the development of the percolated nanoclay network that took place with 2.5 wt% of clay.

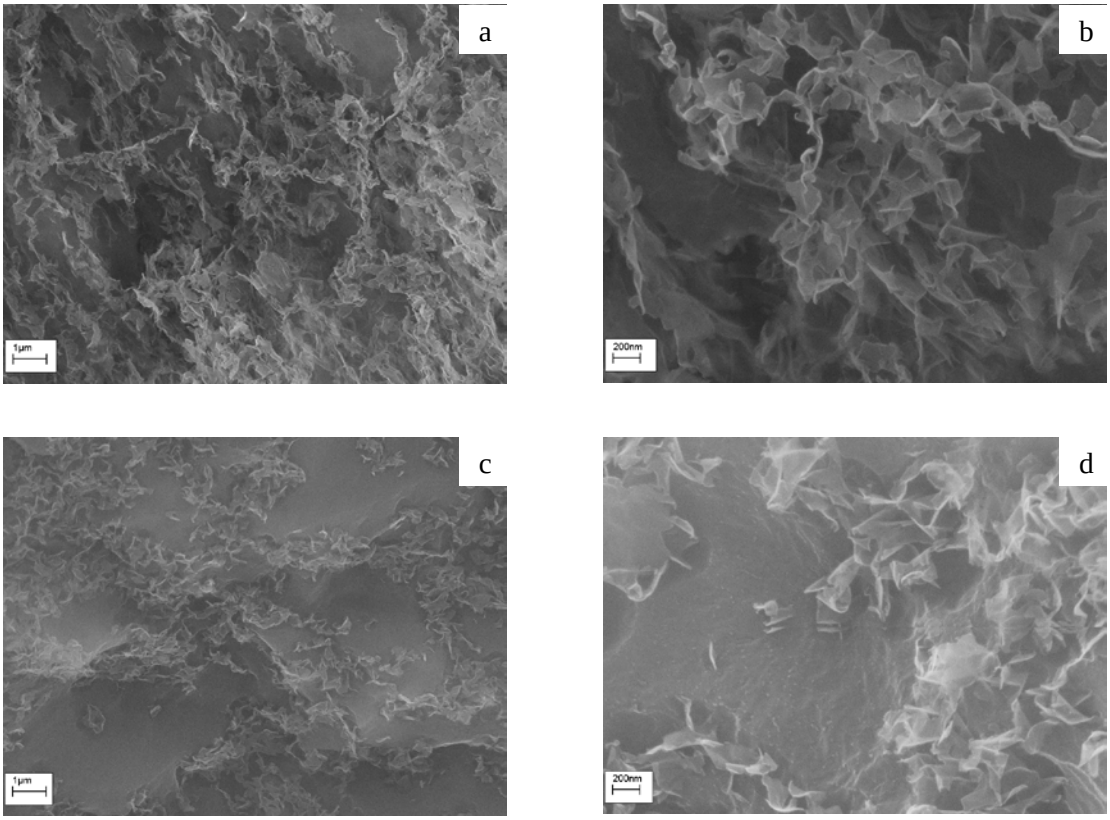

Figure 4.8 SEM images of morphology on the fracture surfaces of the nanocomposites with sonication time of 4 h (a, b), and 6h (c, d).

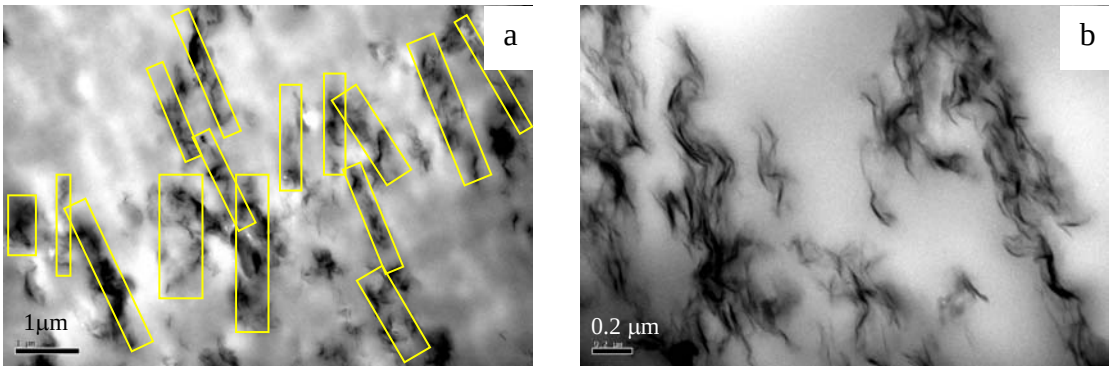

Figure 4.9 TEM images of PET-2.5% 10A nanocomposite sonicated for four hours (a) low and (b) high magnification. (An average aspect ratio (l/t_p) of 4 was estimated from the rectangles that enclosed the clay particles.)

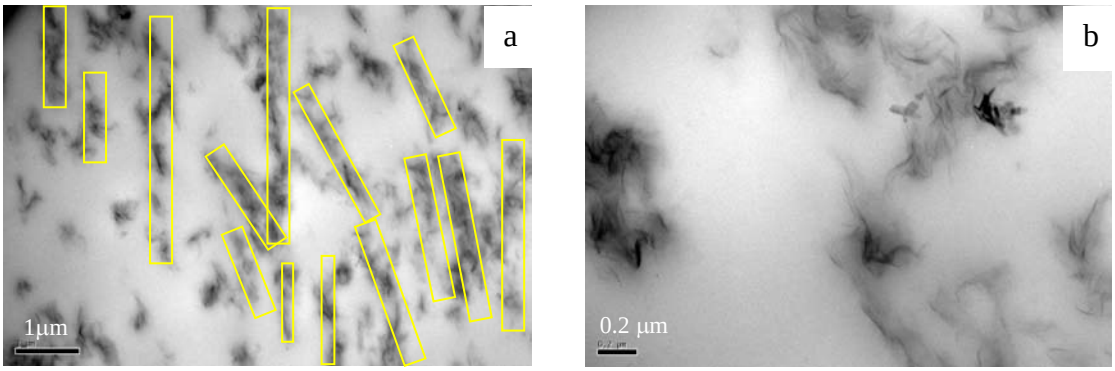

Figure 4.10 TEM images of PET-2.5% 10A nanocomposite sonicated for six hours (a) low and (b) high magnification. (An average aspect ratio (l/t_p) of 7 was estimated from the rectangles that enclosed the clay particles.)

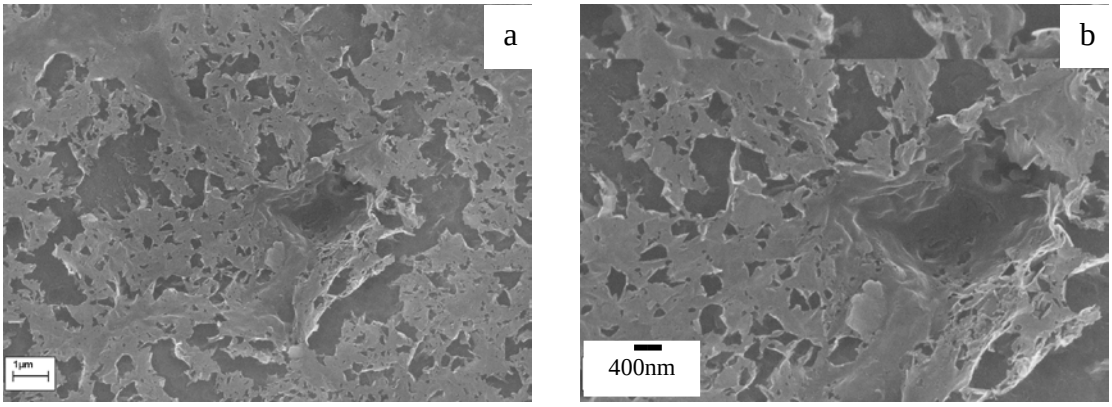

Figure 4.11 SEM images of film surfaces of the 2.5 wt% 10A PET nanocomposite with 1 wt% epoxy at (a) low (b) high magnification show the formation of clay network in the PET.

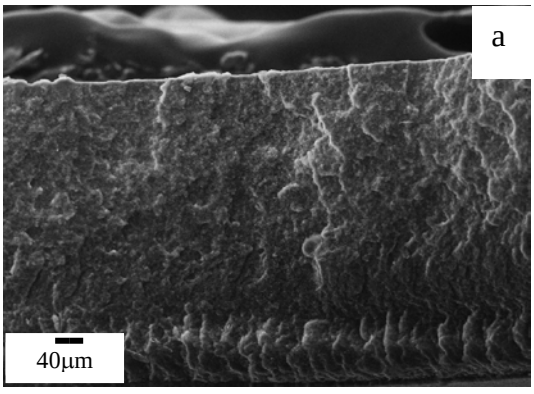

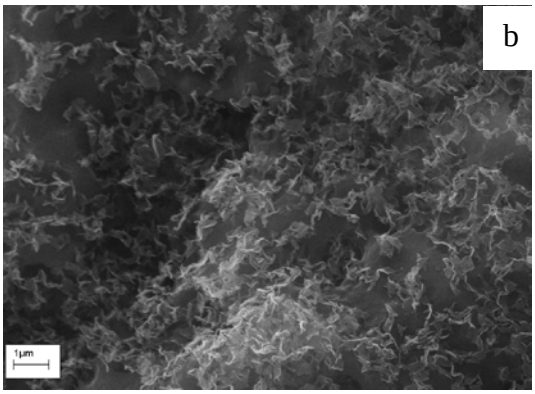

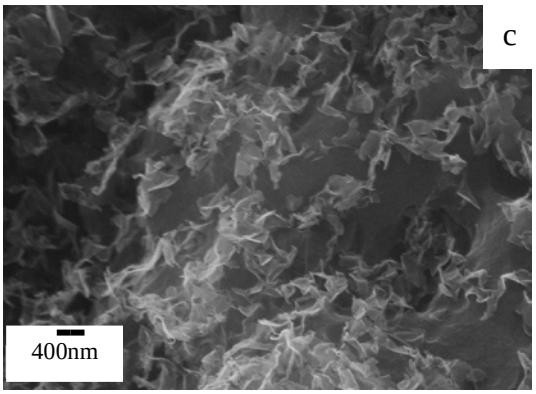

Figure 4.12 SEM images of fracture surfaces of the 2.5 wt% 10A nanocomposite with 1wt% epoxy at (a) very low, (b) low, and (c) high magnification show the 3-D dispersion of the clay nanoparticle in the PET.

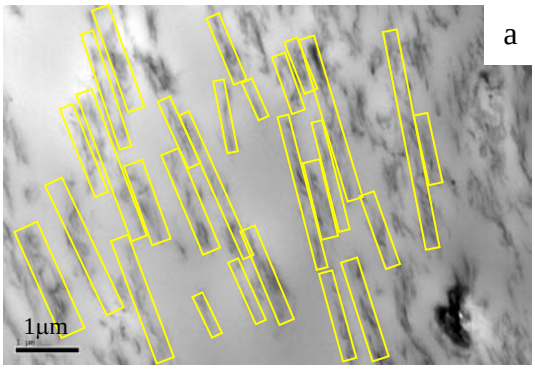

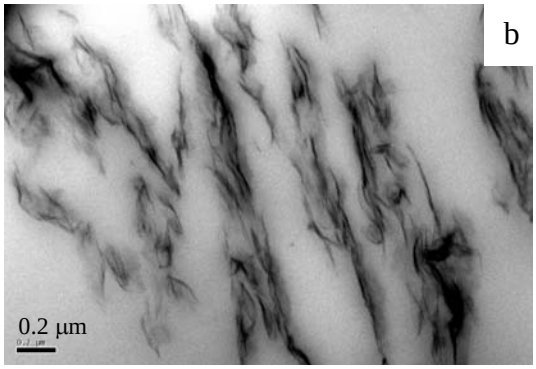

Figure 4.13 TEM images of PET-2.5% 10A nanocomposite containing 1% epoxy with six hour sonication (a) low (b) high magnification. (An average l/t_p of 8 was estimated from the rectangles that enclosed the clay particles.)

The SEM results in Figure 4.8 show the morphology of the fracture surfaces of the 4-hour and 6-hour sonicated samples. The images of the fracture surfaces completely differed from those of the film surfaces. Both samples showed that the stacks of clay layers were broken down into large numbers of thin layered stacks which were finely and randomly dispersed in the matrix. The edges of the clay emerged form the matrix and the clay layers were clearly observed in 3-D view. In the low magnification images in Figures 4.8(a) and 4.8(c), it looks as though the degree of dispersion in the 4-hour sample was higher than that in the 6-hour sample. In the high magnification images, the 6-hour sample, Figure 4.8(d), had a slight higher degree of clay separation than the 4-hour sample, Figure 4.8(b). The combination of the fracture and film images indicated that the 6-hour sample had a better dispersion of the clay than the 4-hour sample. The clay network structure mainly resulted from the network of agglomerations of clay particles rather than that of individual clay layers. Consequently, the maximum properties of a final product might not have been achieved.

Figures 4.9 and 4.10 show the morphology of the 4-hour and 6-hour nanocomposites observed using TEM. An ultra-thin film for the TEM observation was cut from a cross section of the nanocomposite film. From the low magnification images in Figures 4.9(a) and 4.10(a), the 6-hour sample displayed a larger number of particles and less of an area without clay than the 4-hour sample. At the higher magnification in Figures 4.9(b) and 4.10(b), the 6-hour sample had less number of clay layers per stack than the 4-hour sample. The average aspect ratio (l/t_p) of clay particles measured from the TEM images increased from around 4 for the 4-hour sample to around 7 for the 6-hour sample. In this work, the aspect ratio of clay was unable to be accurately estimated because the thickness of the clay particles could not

be estimated precisely from the TEM images. Generally, the precise aspect ratios of clay particles are analysed from TEM images using an image analysis software [66]. Due to a lack of image analysis software, the aspect ratios were estimated from rectangles that enclosed the clay particles as shown in Figure 4.9(a), 4.10(a) and 4.13(a).

From the initial results, the use of epoxy as the compatibilizer significantly improved the dispersion of clay in PET. An exfoliated structure might be achieved by the combination of a long sonication time and the use of a compatibilizer. Epoxy molecules have a strong polarity towards the epoxide group and might penetrate into the interlayer of the clay particles when being subjected to ultrasonic energy. The clay particles would be broken down into large numbers of thinner stacks or even single layers. A 2.5 wt% 10A PET nanocomposite containing 1 wt% epoxy was prepared by solvent blending with ultrasonication for six hours. The morphology of the nanocomposite was observed on the film and fracture surfaces by using SEM as shown by the images in Figures 4.11 and 4.12 respectively.

Figure 4.11 shows the formation of a clay network structure in the sample with the epoxy. Figure 4.12 compared to Figure 4.8(c) and (d) shows that the dispersion state in the sample with epoxy was higher and more uniform than that of the non-epoxy sample. Figure 4.12(a) with very low magnification shows that clay particles were uniformly dispersed throughout the cross section of the film.

The TEM images in Figure 4.13 show higher number of longer and thinner particles than those in Figure 4.9 and 4.10. However, the clay stacks were not completely separated into single layers, resulting in a slight increase of the average aspect ratio from around seven to eight. The network structure developed from the thin stacks of clay layers rather than single clay layers and appeared to be a 2-D

structure lying parallel to the sample surfaces. The TEM images rather than the SEM images showed clay particles oriented parallel to sample surfaces. In summary, the solvent blending PET-clay nanocomposites exhibited intercalated structure with the formation of a percolated clay network at 2.5 wt% clay.

4.2.3 Melt rheology

In chapter 2 (section 2.2) the melt rheological measurement for the investigation of the structure development of polymer/clay nanocomposites was discussed. The rheological behaviour (elastic modulus (G'), viscous modulus, (G''), and complex viscosity (η^*)) strongly depends on the polymer/nanoclay interactions, resulting from the degree of separation and distribution of the organoclay in the polymer matrix. To understand the nanoclay structure in the nanocomposites as observed by SEM and TEM, the linear viscoelastic tests were conducted using a strain of 1% at 270°C in 500-0.1 rad/s frequency range. The rheological results of the neat PET and the nanocomposites with 2.5 and 5 wt% of 10A after ultrasonication for 6 hours are shown in Figure 4.14.

Figure 4.14(a) shows that the neat PET had $G' < G''$ in all the frequency range and a low-frequency dependence (β) with $G' \propto \omega^{\beta = 1.8}$ and $G'' \propto \omega^{\beta = 1}$. The values of β were in the range expected for a homogeneous polymer and suggested that the polymer exhibited liquid-like behaviour (viscous deformation) over the whole frequency range.

When 2.5 wt% of 10A was added and dispersed in the PET to form the nanocomposites, G' and G'' at low frequencies (ω < 1 rad/s) increased and were proportional to the frequency with $G' \propto \omega^{\beta = 0.20}$ and $G'' \propto \omega^{\beta = 0}$ as shown in Figure 4.14(b). The changes in the low-frequency dependence of G' and G'' reflected a

transition from a viscous liquid-like behaviour for the unfilled PET to a more elastic behaviour for the filled PET. Moreover, G' was higher than G'' at the low frequencies. It meant that a percolated clay network structure of the clay nanocomposite prepared by solvent blending with ultrasonication for 6 hours was developed at a clay loading of 2.5 wt%. Xu et al. [98] reported that PS nanocomposites with 3.5 wt% nanoclay exhibited the development of clay network with $G' \propto \omega^{\beta=0.13}$ and G' exceeding G'' at low frequencies ($\omega < 10^{-3}$ rad/s). It has been explained that the percolated clay network was formed when the dispersed clay loading reached a threshold value, at which the dispersed clay did not move freely, due to physical jamming and connections between the dispersed particles [60]. The rheological result confirmed the formation of the clay network structure as observed on the film surfaces of the samples by SEM.

Increasing the clay loading from 2.5 wt% to 5 wt% significantly changed the rheological responses as shown in Figure 4.14(c). The G' and G'' of the 5 wt% samples greatly increased in all of the frequency range and showed more plateau responses at low frequencies (the so-called terminal zone) with a further decrease in β with $G' \propto \omega^{\beta=0.16}$ compared with those of the 2.5 wt% sample. Moreover, $G' > G''$ in all of the frequency range reflected that the 5 wt% sample transformed the viscous liquid-like behaviour to the more elastic behaviour over the whole frequency range, suggesting a stronger clay network structure in the 5 wt% sample compared with the 2.5 wt% composite due to the increased number of clay particles.

The value of the complex viscosity (η^*) showed that the neat PET had Newtonian behaviour in the frequency range < 100 rad/s. The nanocomposites, however, exhibited a pronounced shear thinning response. The degree of the shear thinning is described by the power-law index (α) of the complex viscosity ($\eta^* \propto \omega^{\alpha}$).

The Newtonian fluid of the molten unfilled PET had the power law index of $\alpha = 0$. The shear thinning index of the filled PET increased with increasing the clay loading, $\alpha = 0.79$ for the 2.5% sample and $\alpha = 0.89$ for the 5% sample.

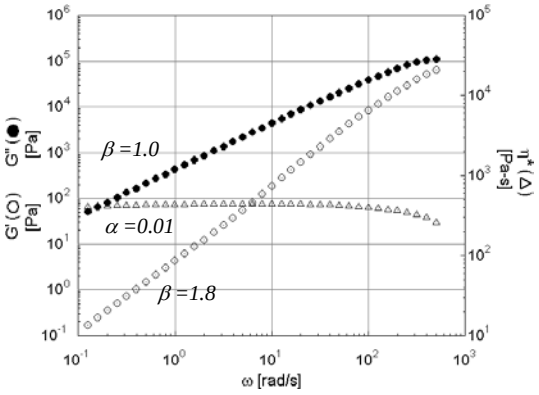

a

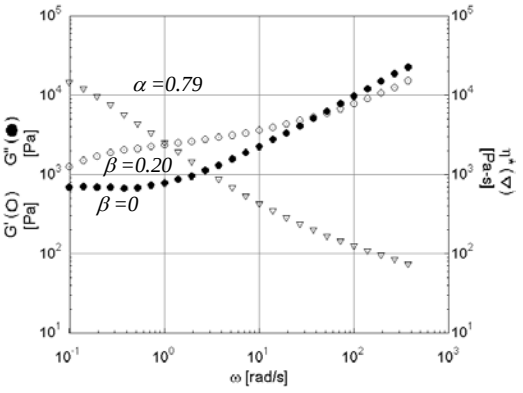

b

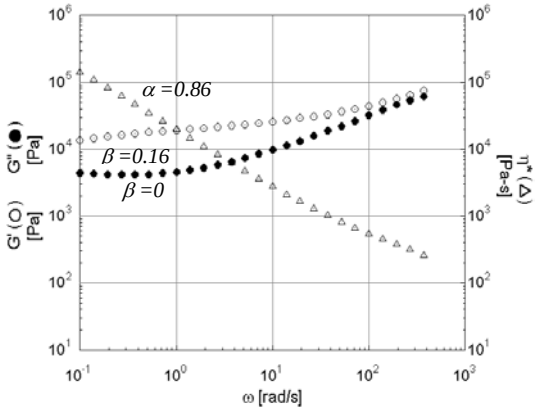

c

Figure 4.14 Rheological behaviour of (a) neat PET and PET nanocomposites with (b) 2.5 wt%, (c) 5 wt% Cloisite 10A (solvent blending with sonication for six hours).

4.2.4 Morphology-Rheology-Tensile property relationship

It has been reported that a clay network structure has a significant effect on the flammability properties of ABS/clay nanocomposites [99]. Previous sections have shown that a clay network structure can be developed in PET nanocomposites with a clay loading of 2.5 wt% (or 1.25 vol %). The following question did, however, arise from this: besides the aspect ratio, did the clay network structure affect the tensile properties of PET nanocomposites? This section reports on the study of the effect of the clay network structure on the tensile properties of the PET/clay nanocomposites.

2.5 wt% 10A PET/clay nanocomposites with different degrees of clay dispersion were prepared with sonication times of one, four, and six hours. All the tensile specimens were prepared as thin amorphous films by compression moulding. The molten films were rapidly quenched after compression at 260°C for three minutes to obtain the amorphous films. Figure 4.15 shows the morphology-rheology-tensile property of the PET nanocomposites with different sonication times. There is clear evidence that increasing the sonication time induced an enhancement of the clay dispersion and thus accounted for the change in the rheological and mechanical properties.

As seen in the SEM image, Figure 4.15 or Figure 4.7(a), of the sample after 1 hour sonication, the clay particles were not dispersed throughout the polymer matrix with evidence of small and large stacks of clay layers. The 1-hour sonicated sample also showed weak elastic behaviour (or weak interfacial interactions between the polymer chains and clay layers) with $G' \propto \omega^{\beta=0.52}$ and $G'' \propto \omega^{\beta=0.67}$, G' slightly exceeding G'', and the shear thinning response of $\eta^* \propto \omega^{\alpha=0.5}$. The changes in β and α were low due to the small number of dispersed clay particles interacting with the

polymer matrix. The 1-hour sonicated samples in Figure 4.16 had a higher tensile modulus than the unfilled PET in Figure 4.16 by 11%. The tensile strength did not change. The elongation at break decreased from 250% to 12%.

With the longer sonication time of four hours, the nanocomposite possessed a higher dispersion of the clay without any large particles compared with the 1-hour sonicated sample. In addition, the rheological result showed G' exceeding G'' at low frequencies, a low-frequency slope of $G' \propto \omega^{\beta=0.23}$, and shear thinning response of $\eta^* \propto \omega^{\alpha = 0.75}$. The changes in β and α indicated that the melt rheological properties of the 4-hour sonicated sample changed from a viscous liquid-like to a more elastic response with the formation of a clay network structure. Compared with the 1-hour sonicated sample, the 4-hour sonicated sample exhibited a slight increase in the tensile modulus and strength. The elongation at break increased from 12% to 25%.

An increase of the dispersion time from four to six hours significantly increased the values of G' and G'' (at ω = 0.1 rad/s) and changed the low-frequency dependence of $G' \propto \omega^{\beta=0.20}$ and the shear thinning index of $\eta^* \propto \omega^{\alpha = 0.79}$. The SEM image of the 6-hour sample, Figure 4.15, revealed a higher dispersion of clay and a more developed clay network structure. The change in the morphology and rheology led to increases in the modulus of 17% and the strength of 13% relative to the cast pure PET. However, the elongation at break did not further increase despite the significant changes in the morphological and rheological properties.

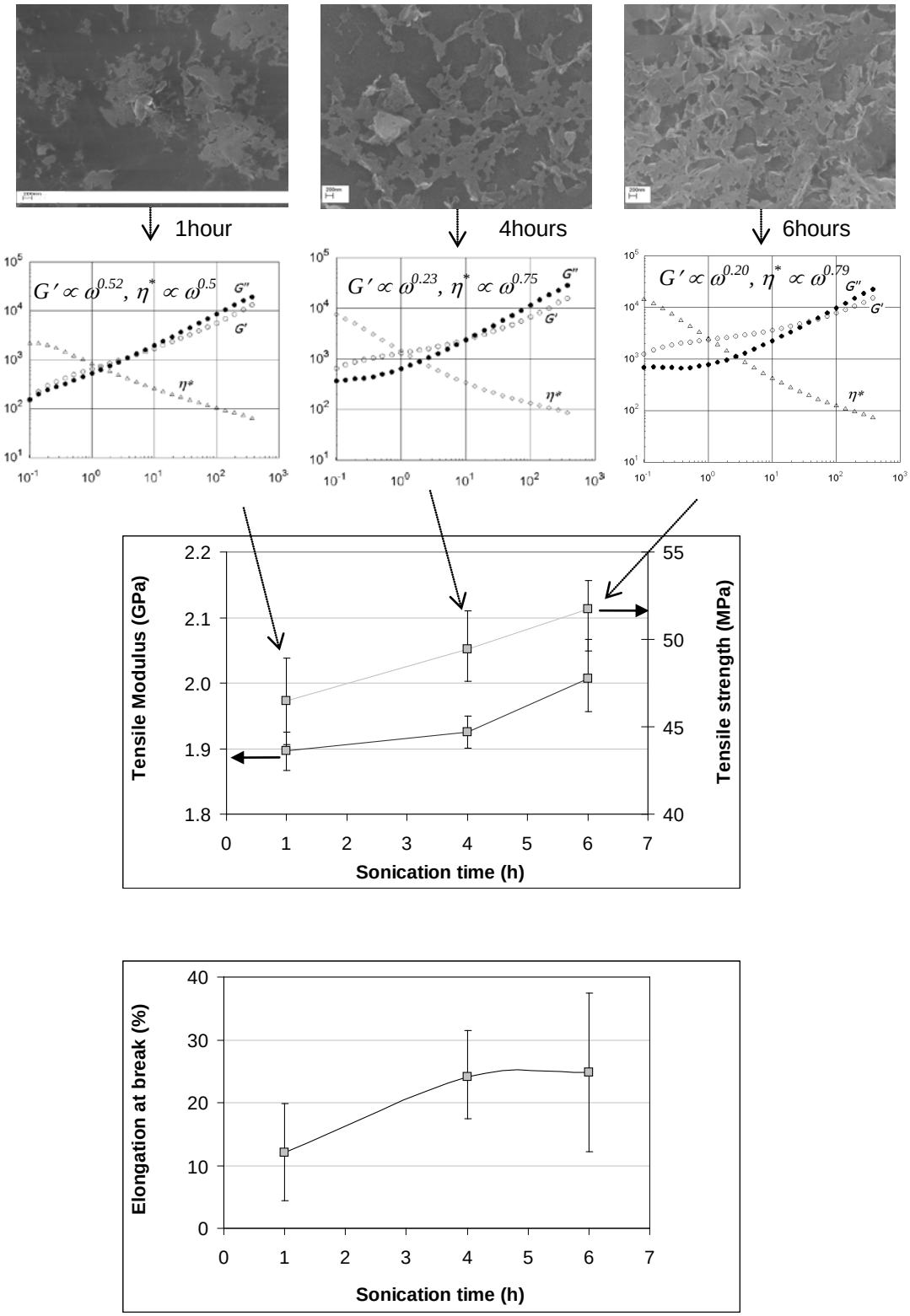

Figure 4.15 Morphology-rheology-tensile properties of the amorphous PET nanocomposite films containing 2.5 wt% 10A with sonication times of one, four, and six hours.

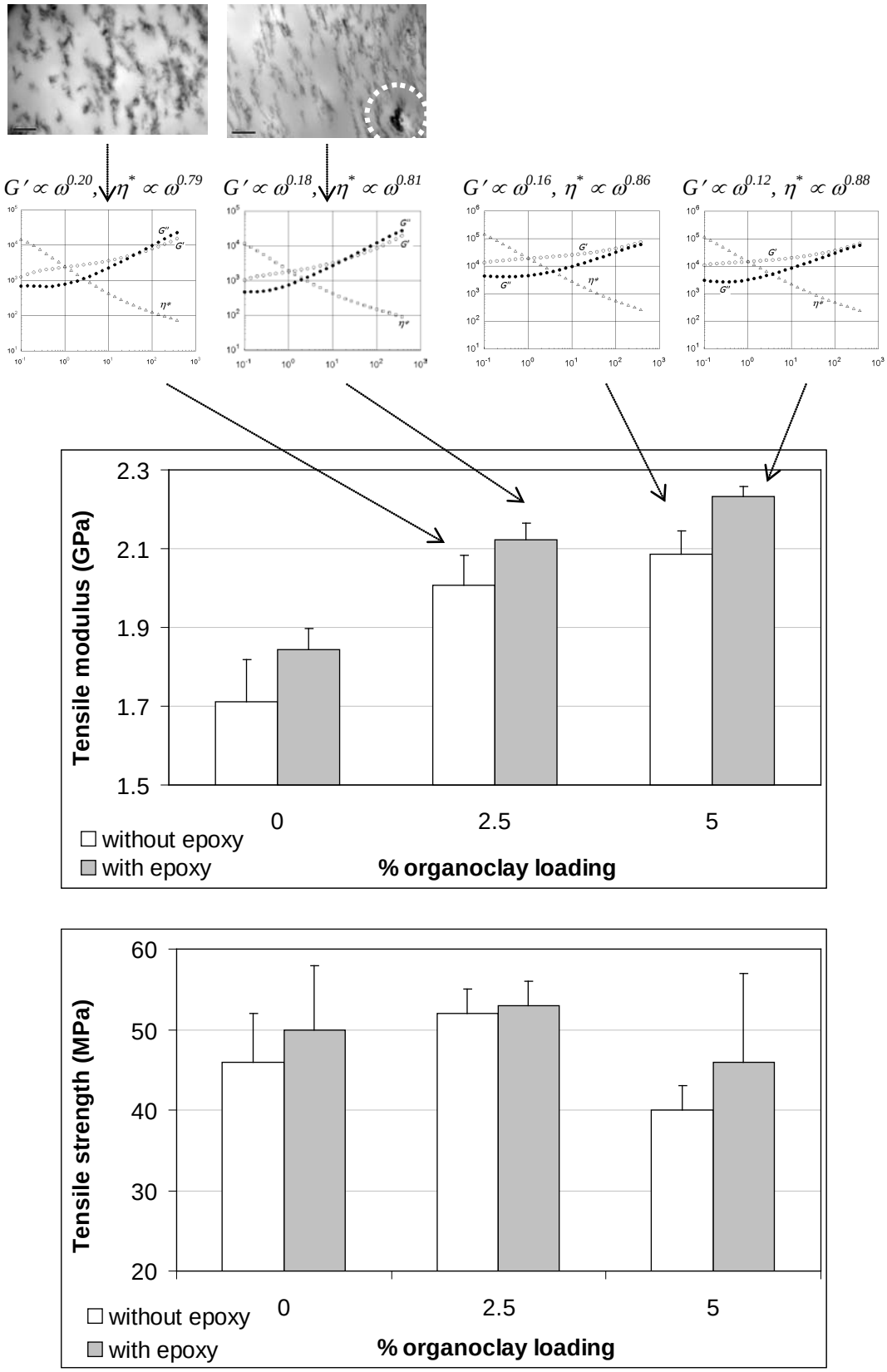

Figure 4.16 The effect of the epoxy addition on the morphology-rheology-tensile properties of films of amorphous PET and 2.5 and 5wt% 10A-PET nanocomposites with a sonication time of six hours.

The development of the clay network structure began during the first hour of the sonication time and improved with increasing the sonication time, resulting in a significant change in β and α at low frequency. The difference between 4-hour and 6-hour nanocomposites in the low-frequency dependence ($\beta \rightarrow 0$) and in the shear thinning index ($\alpha \rightarrow 1$) was slight. The values of G', G'', and η^* at low frequency (ω = 0.1 rad/s), however, significantly increased.

Although the clay network structure significantly influenced the rheological properties, the tensile modulus increased by only 17%. This % increase in modulus was similar to the value predicted by the Halpin-Tsai equation using a clay aspect ratio of ten as discussed in chapter 2 (section 2.2). It appeared that the network structure did not affect the tensile properties.

Figure 4.16 illustrates the morphology, rheology, and tensile properties of 2.5 and 5 wt% PET nanocomposites with and without 1 wt% epoxy. All the solvent blended nanocomposites were subjected to ultrasonication for six hours. TEM images of the 2.5 wt% nanocomposites with and without epoxy showed that the larger numbers of thinner particles were finely dispersed in the nanocomposites with epoxy. A large particle in the dashed circle was, however, observed in the matrix and would probably cause premature failure under a tensile stress.

The tensile test results in Figure 4.16 show that adding 1 wt% epoxy increased the tensile modulus and strength of the cast pure PET. This improvement can be attributed to a chain-extension reaction between epoxy and PET. In Figure 4.17, the two functional end groups of carboxyl (-COOH) and hydroxyl (-OH) in a PET molecule can react with two epoxide groups in one epoxy molecule [100,101], resulting in an increase of the molecular weight of PET. This reaction was supported by previous workers who presented FTIR (Fourier Transform Infra-Red) spectra of an

epoxy blend with PBT [92]. The FTIR results indicated the formation of hydrogen bonds between the epoxide groups and the carboxyl or hydroxyl end groups in the PBT. Figure 4.18 shows that the elongation at break decreased with the addition of the epoxy compared with the cast pure PET.

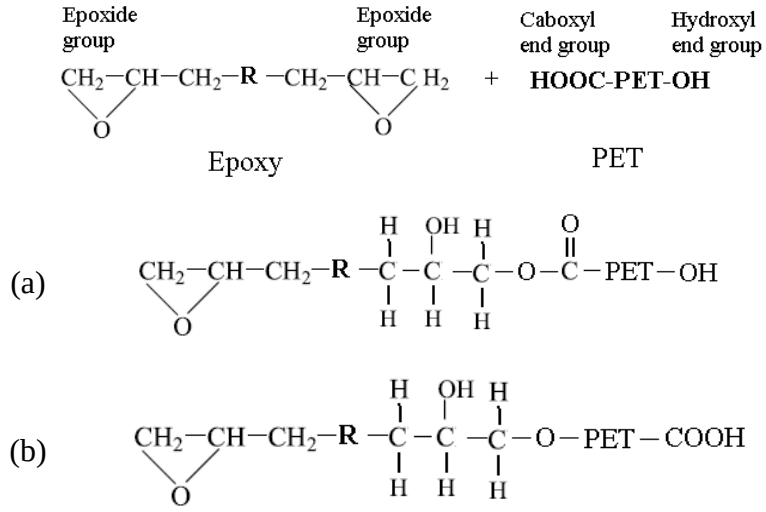

Figure 4.17 Possible reactions between PET and epoxy, diglycidyl ether of bisphenol A or DGEBA, (a) -COOH and epoxide groups (b) -OH and epoxide groups based on work done on PBT [102]

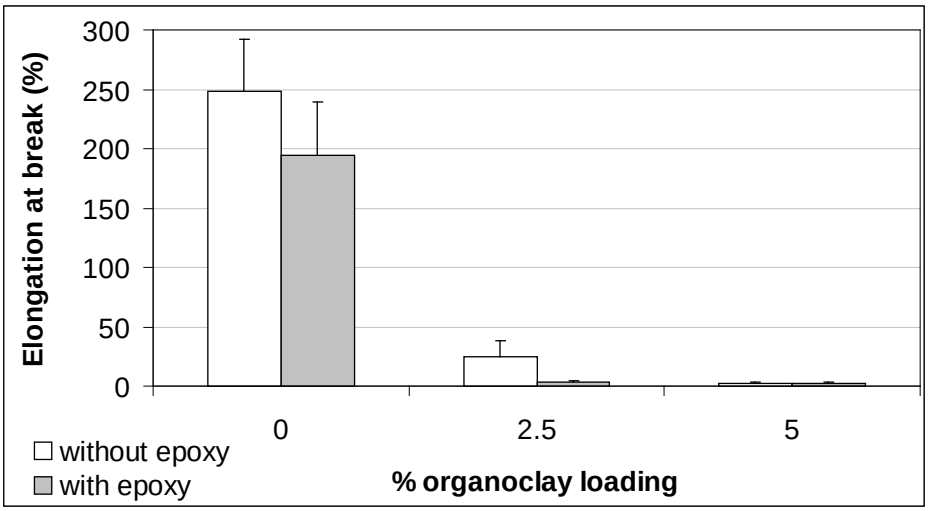

Figure 4.18 Elongation at break of films of amorphous PET and PET nanocomposite films containing 2.5 and 5 wt% 10A with and without epoxy.

Adding epoxy to the nanocomposites increased their tensile modulus and strength. Because the aspect ratio of the dispersed clay particles in the 10A-epoxy-PET nanocomposite only slightly increased as explained in section 4.2.2, the improved tensile property was attributed to the reaction between the epoxy and the PET rather than an improvement of the clay dispersion. When the organoclay content was 5 wt%, the tensile strength of the nanocomposite was lower than that of the cast pure PET. This indicated that an optimum amount of organoclay was needed to balance the properties.

With the addition of the epoxy, the nanocomposites showed a more elastic response with a further decrease in β of the storage modulus and an increase in α of the complex viscosity. The values of G', G'' and η^* did not increase despite the significant improvement in the dispersed state of the clay as observed by TEM. To find an answer to the discrepancy between rheological and morphological results, the cast PET samples with and without epoxy were prepared by dissolving PET in a solvent of phenol/chloroform and then drying to extract the solvent. The rheological measurement of the cast samples was investigated and the results are compared and shown in Figure 4.19. It is clearly seen that the elastic modulus and complex viscosity of the cast PET with epoxy was less than that of the cast PET. Similarly, a decrease of the intrinsic viscosity of PET via branched chain extension reactions with epoxy (diglycidyl ethers) was reported by Haralabakopoulos et al. [100]. The reason for this is that the branched polymers occupy less volume in solution than linear polymers of the same molecular weight [102] and therefore they have a lower viscosity at the same concentration [103]. These reductions might affect the rheological properties of the nanocomposites with the epoxy. The values of G', G'' and η^* of the nanocomposites with epoxy, therefore, did not increase.

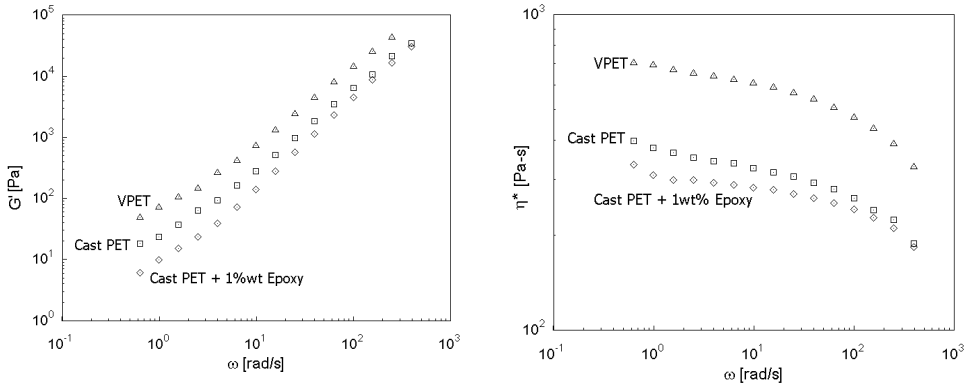

Figure 4.19 Comparison of the storage modulus and complex viscosity of the cast PET and cast PET with 1% epoxy, testing at 250°C.

The improvement in the clay dispersion resulting from the addition of the epoxy can be explained by the following mechanism. The epoxy can react with both the organoclay and the PET molecules, as shown in the schematic in Figure 4.20. The reaction between the epoxy and the organoclay results in an increase in the compatibility between the organoclay and the PET [97]. During the pre-blending of the epoxy and the organoclay, the epoxy molecules attached to the edges of the clay layers via the reaction between epoxide groups of the epoxy molecules and the hydroxyl groups at the edge of the clay layers. When the PET and the organoclay-epoxy were blended, the PET molecules attached to the epoxy molecules at the edge of the clay layers. This led to a strong interaction between the matrix and the clay, resulting in the improvement in the dispersion.

There are two possible reasons for the incomplete separation of the clay particles after the interaction with the epoxy and the polymer during sonication. First, the required shear stress to fully separate the very thin clay particles was not high enough during blending. Secondly, the branched chains inside and outside the clay galleries could still produce a bond between the clay particles that cannot be broken by the forces of sonication. These two reasons could account for the long and thin

clay particle stack in the PET matrix with epoxy as shown in the TEM image in Figure 4.20.

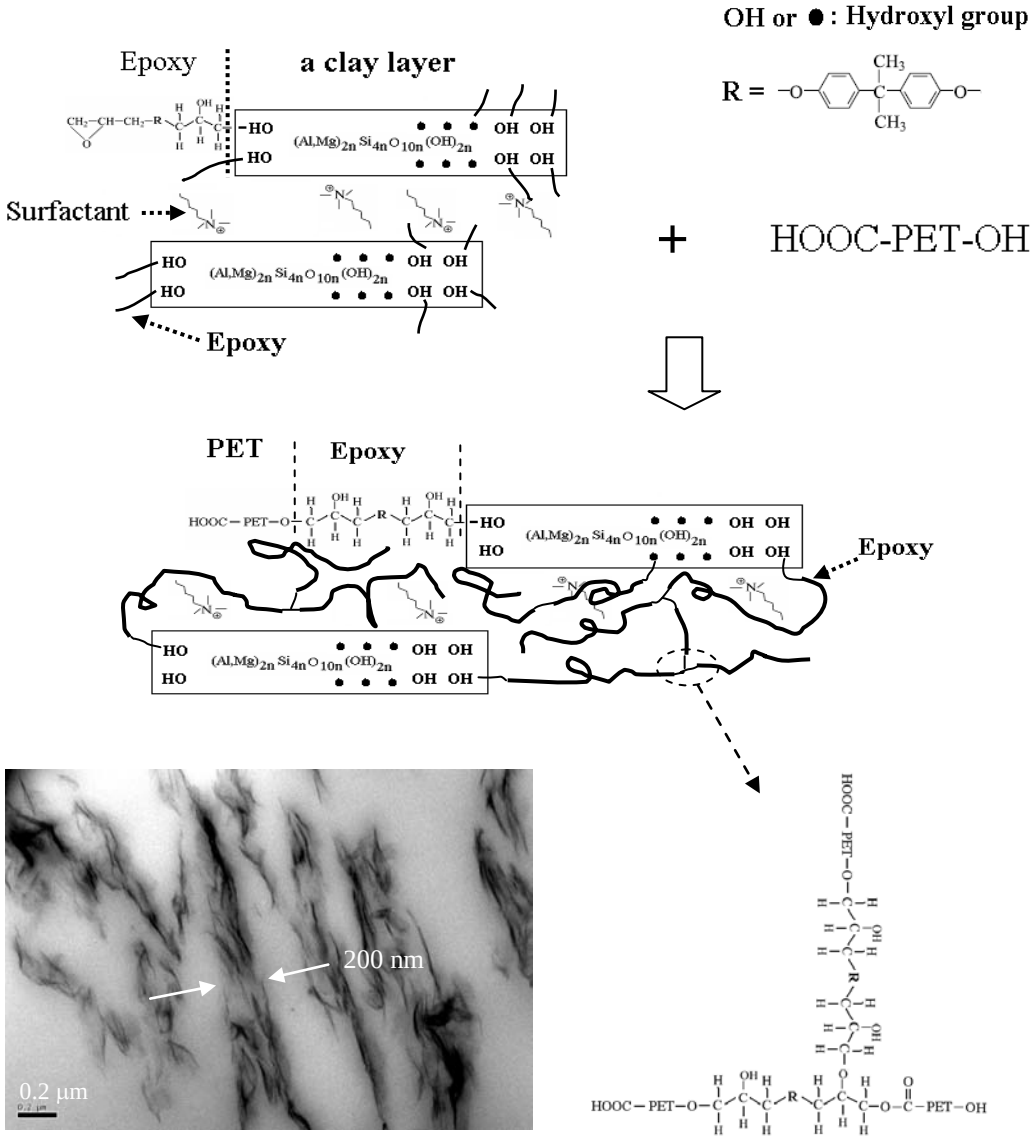

Figure 4.20 Schematic presentations of the possible reaction between the epoxide group and the –OH group at the edge of clay layers, and the reaction between the epoxide group and the –OH in PET, TEM shows the thickness of the clay particles.

For the complete dispersion, a longer sonication time or higher stresses may be effective. In order to verify this, a solvent blended PET nanocomposite with 2.5 wt% of the 10A and 1% of the epoxy was prepared. The nanocomposite was subjected

to sonication for 12 hours. Figure 4.21 shows the SEM images of the nanocomposite. Although the sonication time was increased to 12 hours, the clay particles were still not completely separated. The degree of dispersion of the 12-hour sample did not increase compared with that of the 6-hour sample, Figure 4.12(c). The possible reason for this is that the clay particles were bonded by the branched PET chains. In addition, the large number of the dispersed clay particles were too thin (200 nm thick see Figure 4.20) to be further separated by the frequency (33 kHz) of the ultrasonic power source. To further break the thin clay particles, ultrasonic energy with a higher frequency may be required.

In order to determine the effect of shear stress on the particles, a 50:50 (w/w) of the nanocomposite (12-hour sonication) and neat PET were blended for five minutes using a mini conical counter-rotating twin screw extruder (Thermo Scientific). The screw speed was 60 rpm and temperature was 260°C. The addition of the neat PET was intended to increase the viscosity of the 12-hour sonication nanocomposite that would result in an increase in the shear stress on the nanoparticles during melt blending. The solvent + melt blended nanocomposite contained the 1.25 %wt of the 10A. Figure 4.22 shows the SEM images of the morphology of the solution sonicated/melt blended nanocomposite. It shows that the dispersion state was significantly enhanced by the shear stress imposed by the extruder, despite the reduction in the clay content by the addition of the virgin PET. This was attributed to the increase in the viscosity of the blend that enabled a higher shear stress to be imparted to the clay than was possible with the solvent-only blended composite. Figure 4.23 shows the morphology of the same sample observed using TEM. The images showed that the long clay particles were further separated into the shorter particles compared to the TEM images in Figure 4.20. Some of the agglomerates

were, however, observed in the matrix. This indicates that the solution sonicated/melt blended nanocomposite possessed a partially exfoliated structure.

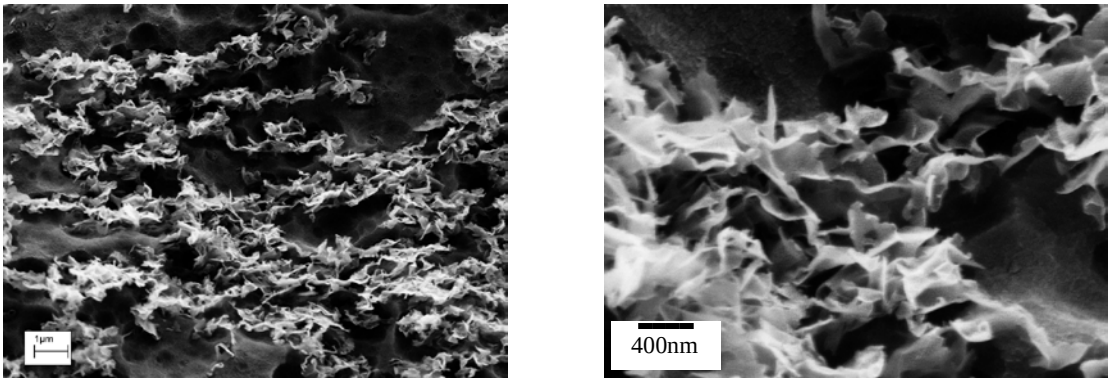

Figure 4.21 SEM images of the 2.5 w% 10A PET nanocomposite prepared by solvent blending with the epoxy and sonication for 12 hours.

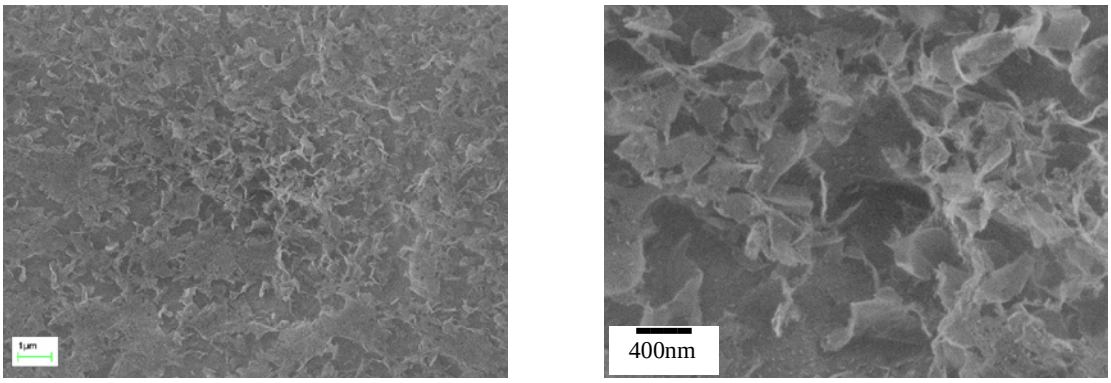

Figure 4.22 SEM images of the 1.25 wt% 10A PET nanocomposite prepared by solvent blending with the epoxy and sonication for 12 hours and then melt blended via a mini twin screw extruder.

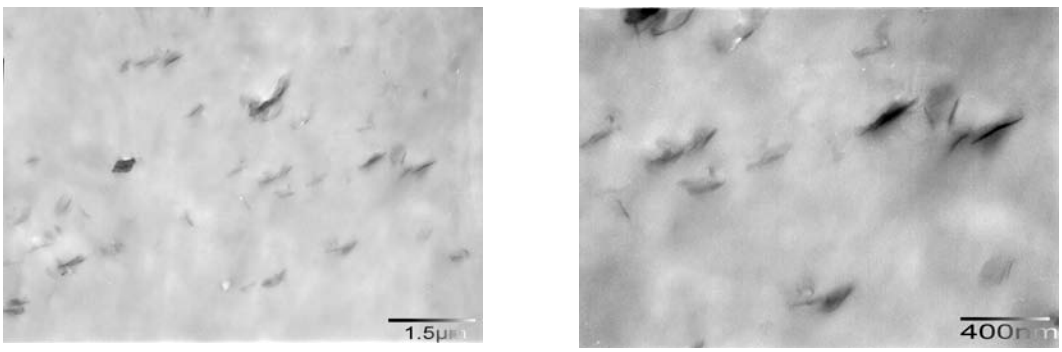

Figure 4.23 TEM images of the same sample as in Figure 4.22.

4.3 Effect of organic modifiers

In this study, the solvent blending technique was used to prepare PET nanocomposites of four organoclays with different chemical structures and amount of surfactant. The four different organoclays that were used were Cloisite 10A (10A), Cloisite 15A (15A), Nanofil 2 (N2) and SE3010 (SE). The N2 and the 10A had the same surfactant shown in Figure 4.24, but in different amounts. The N2 had 75 meq/100g of CEC with an interlayer distance of 1.8 nm, while the 10A had 125 meq/100g of CEC with an interlayer distance of 1.92 nm. This allowed an investigation of the influence of the amount of modifier on the morphology of the nanocomposites.

The 10A, 15A and SE had a different organic chemical structure. The surfactant in the 10A and N2 had one long alkyl group and one relatively polar benzyl group shown in Figure 4.24(a). The surfactant in the 15A had two long alkyl groups and a non-polar methyl group shown in Figure 4.24(b). The surfactant of the SE has not been revealed because there is a patent pending relating to it. The SE3010 organoclay was developed for PA6, PA6.6, ABS, PS, and PC.

Initially, PET was dissolved in a phenol/chloroform solvent combination, and then 5 wt% organoclay was added in the PET solution. The PET/organoclay nanocomposite suspension was sonicated for five minutes. The resultant nanoparticle suspensions of the different organoclays in the PET solution were put into closed containers and left for 24 hours at room temperature. Figure 4.25 shows the nanocomposite suspensions after 24 hours. It was noticed that the 15A nanoparticle suspension turned from clear to milky after 24 hours shown in Figure 4.25(a), indicating that the suspension was unstable. The 10A, N2 and SE nanoparticle suspensions were, however, still clear after 24 hours, Figure 4.25(b), indicating that the suspensions were stable. The result implied that the 15A particles in the

nanocomposite suspension might agglomerate and settle down on the substrate during the drying process in a vacuum oven for 72 hours. The 15A was not, therefore, considered suitable for the preparation of a PET nanocomposite by solvent blending with a mixture of phenol and chloroform.

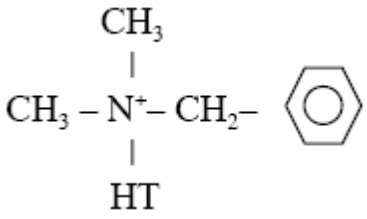

Cloisite 10A and Nanofil-2

(a)

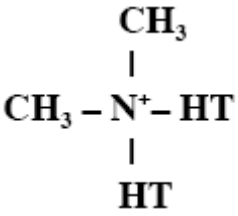

Cloisite 15A

(b)

Figure 4.24 Chemical structures of the surfactant, HT = Hydrogenated tallow, T = tallow.

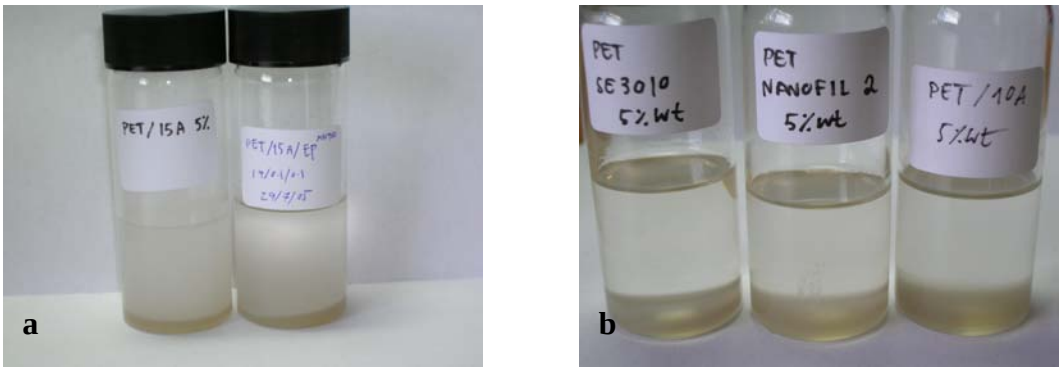

Figure 4.25 PET/organoclay nanocomposite solution using a mixture of phenol and chloroform, containing 5wt% of (a) 15A (Left) and 15A+1wt% epoxy (Right), (b) SE (Left), N2 (Middle), and 10A (Right).

4.3.1 Morphology

The results in the section 4.2.2 and 4.2.3 showed that a clay network structure was formed in a PET nanocomposite with a clay loading of 2.5 wt%. Therefore, all the PET nanocomposites in this section contained 2.5 wt% of the organoclays. The solvent blended nanocomposites were subjected to the ultrasonic treatment for six hours. The SEM images of the nanocomposites in Figure 4.26 show the nanoclay dispersion observed on fracture surfaces. The 10A nanocomposite in Figure 4.26(c) showed the highest degree of clay dispersion in the matrix, while the SE nanocomposite in Figure 4.26(a) had the lowest degree. As explained earlier, the chemical modifiers in the 10A and N2 were similar but the concentration of the modifier was higher in the 10A than that in the N2. This could account for the observation that the N2 nanocomposite, Figure 4.26(b), possessed a lower dispersion of clay than the 10A sample.

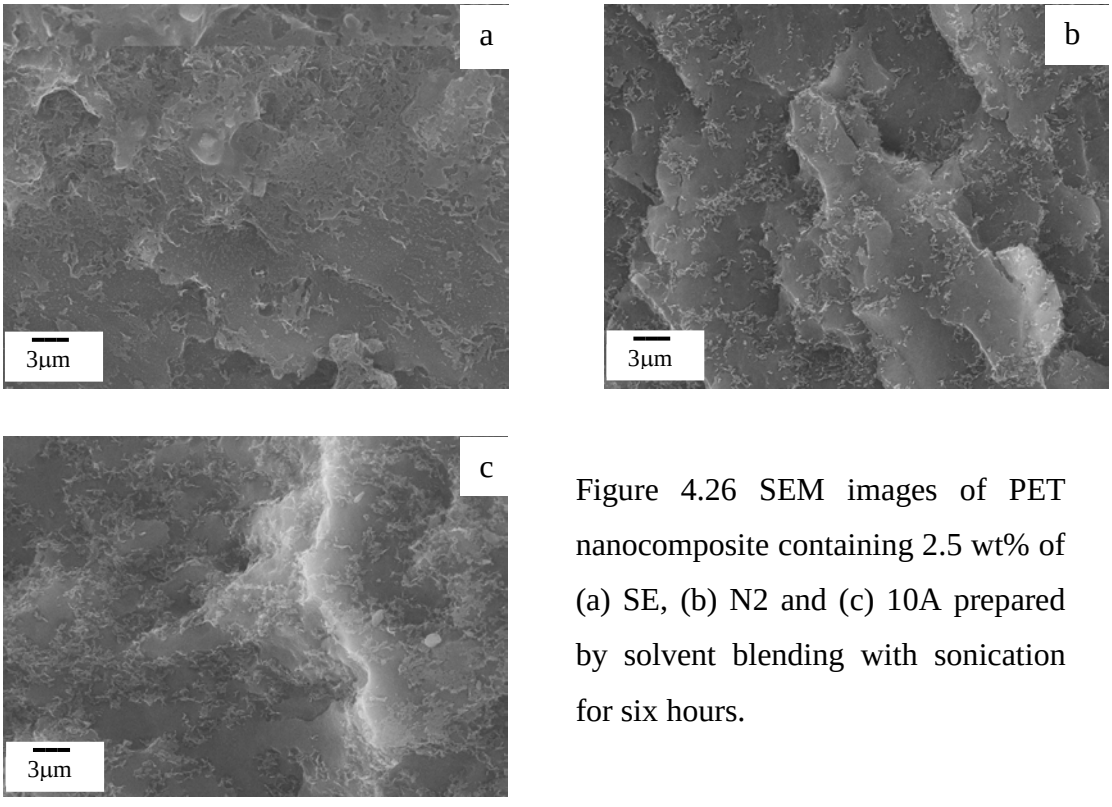

Figure 4.26 SEM images of PET nanocomposite containing 2.5 wt% of (a) SE, (b) N2 and (c) 10A prepared by solvent blending with sonication for six hours.

4.3.2 Melt rheology

The rheological properties for the PET nanocomposites containing 2.5 wt% of SE, N2 and 10A nanoclay are presented in Figures 4.27 (for SE, N2) and Figure 4.14(b) (for 10A) and Table 4.1. The differences in β and α of the three nanocomposites suggested that the solid-like response was highest for the 10A nanocomposite and lowest for the SE nanocomposite. Both 10A and N2 nanocomposites exhibited the formation of a clay network structure at the clay loading of 2.5 wt% with $G' > G''$ at low frequencies as shown in Figure 4.14(b) and 4.27(b). The clay network structure in the 10A nanocomposite was more developed than that in the N2 nanocomposite. This indicated that the 10A was better dispersed in the PET matrix than the N2 clay. For the SE nanocomposite, the development of a network structure was not evident with $G' < G''$ for all the frequencies as shown in Figure 4.27(a). The rheological results indicated that the dispersion of the nanoclay was most developed in the 10A nanocomposite and least developed in the SE nanocomposite. This was in agreement with the SEM results. In summary, increasing the modifier content from 75 meq/100g for the N2 to 125 meq/100g for the 10A clay considerably improved the degree of separation and dispersion of the clay in the PET. Both the 10A and N2 organoclays were more compatible with PET than the SE organoclay.

Table 4.1 Low-frequency index (β) of G', G'' and power law index (α) of η^* for PET nanocomposites containing 2.5 wt% of SE, N2 and 10A organoclays.

Nanocomposite	β of G'	β of G''	α of η^*
SE	0.57	0.58	0.41
N2	0.36	0.26	0.65
10A	0.20	0.00	0.79

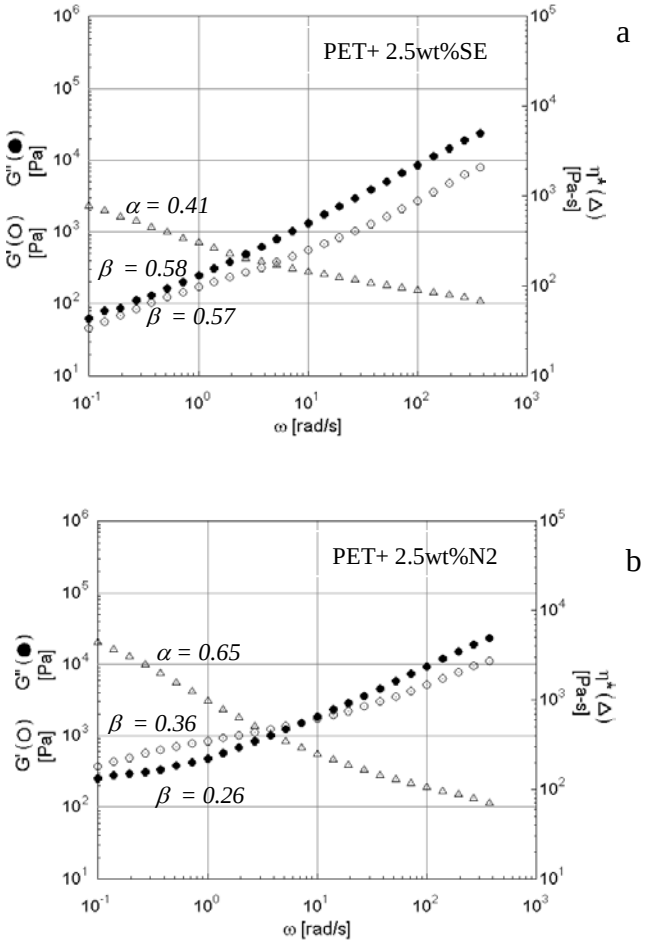

Figure 4.27 Rheological behaviour of PET composites with 2.5 wt% of (a) SE, (b) N2 organoclay prepared with ultrasonication for six hours.

4.3.3 Tensile properties

Figure 4.28 shows the tensile modulus, strength, and elongation at break of the SE, N2, and 10A nanocomposites. The 10A nanocomposite that had the best dispersion of the clay also exhibited the greatest improvement in the tensile modulus and strength compared with PET. The modulus and strength of the N2 nanocomposite were slightly higher than those of the SE nanocomposite. All nanocomposites showed the same breaking strain.

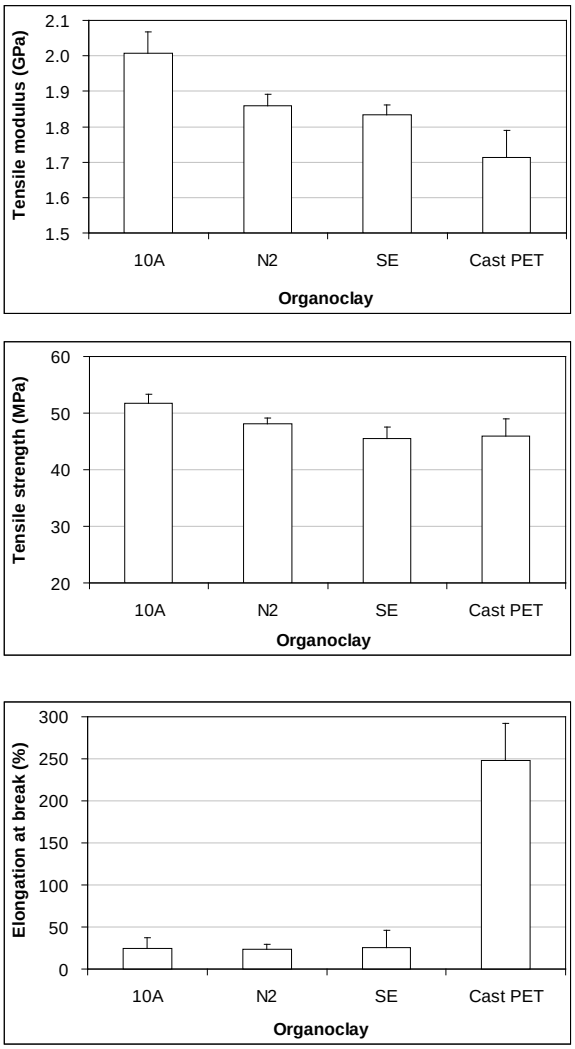

Figure 4.28 Mechanical properties of the cast PET and PET nanocomposite films

4.4 PET/organoclay nanocomposites by melt blending

To compare the extent of nanoclay dispersion between the melt blended and solvent blended nanocomposites, PET (IV of 0.75 dL/g) and 5 wt% of the 10A clay were blended in a twin screw extruder The rheological properties of the nanocomposite were investigated and the results are as shown in Figure 4.29 and Table 4.2 and were compared to those of the solvent blended nanocomposites. A comparison of the rheological properties in Table 4.2 shows that the 2.5 wt% clay solvent blended sample exhibited a stronger elastic behaviour in spite of the lower clay loading compared with the 5 wt% clay melt blended sample. The rheological results clearly demonstrated that solvent blending provided a greater dispersion of the clay in PET than melt blending.

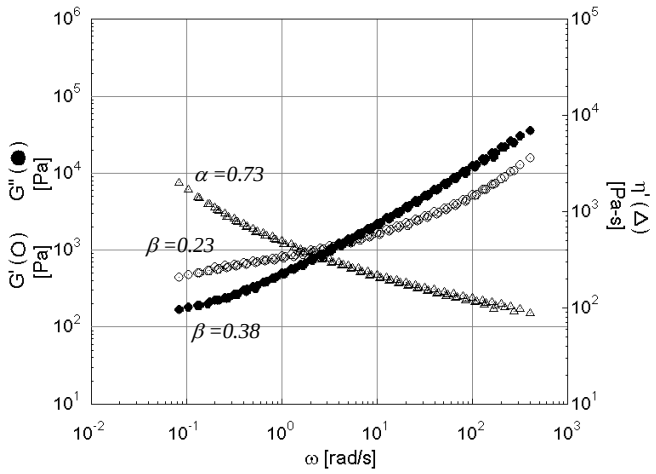

Figure 4.29 Rheological responses of PET nanocomposites with 5 wt% of the 10A prepared by melt blending

Table 4.2 Low-frequency index (β) of G', G'' and the power law index (α) of η^* for PET nanocomposite containing 10A prepared by solvent blending and melt blending.

Nanocomposite	β of G'	β of G''	α of η^*
PET-2.5 wt% 10A by solvent blending	0.20	0.00	0.79
PET-5 wt% 10A by solvent blending	0.16	0.00	0.89
PET-5 wt% 10A by melt blending	0.23	0.38	0.73

4.5 Effect of residual solvent on the thermal properties of cast PET

Ou et al. [32,33] reported the crystallization of solvent blended PET nanocomposites in a mixture of phenol and chloroform. They did not report the effect of residual solvent in the nanocomposites after extracting the solvent in a vacuum oven at 70°C left overnight. In the present study, it was found that there was residual solvent remaining in the sample after the drying process.

In order to study effects of the residual solvent on the thermal properties of PET, cast virgin PET samples were produced by dissolving PET in a mixture of phenol/chloroform. The solution was then evaporated in a vacuum oven at 80°C for 24 hours (PETC-24), 36 hours (PETC-36), and 60 hours (PETC-60), respectively. The thermal properties of the cast virgin PET and unprocessed virgin PET (VPET) were studied using DSC. The samples were heated to 280°C, held at this temperature for three minutes to remove their previous crystals, and then rapidly quenched prior to analysis.

The first heating scan results presented in Figure 4.30(a) and Table 4.3 show significant changes in the glass transition temperature (T_g) from 79°C for the VPET to 68°C for both PETC-36 and PETC-60 and to 63°C for PETC-24. The reduction of the T_g of the cast PET was most likely due to an amount of residual solvent. PETC-24 with the shortest drying time appeared to have a larger amount of residual solvent than PETC-36 and PETC-60. This accounted for the lower T_g of PETC-24 than that of PETC-36 and PETC-60. The residual solvent would act as a plasticizer by swelling the polymer, increasing its free volume. The polymer chain mobility was, therefore, increased and resulted in the reduction of the T_g [104]. A similar phenomenon has

been reported by others in a publication related to the production of PET ionomer/silica nanocomposites with a polymer in situ sol-gel reaction [105].

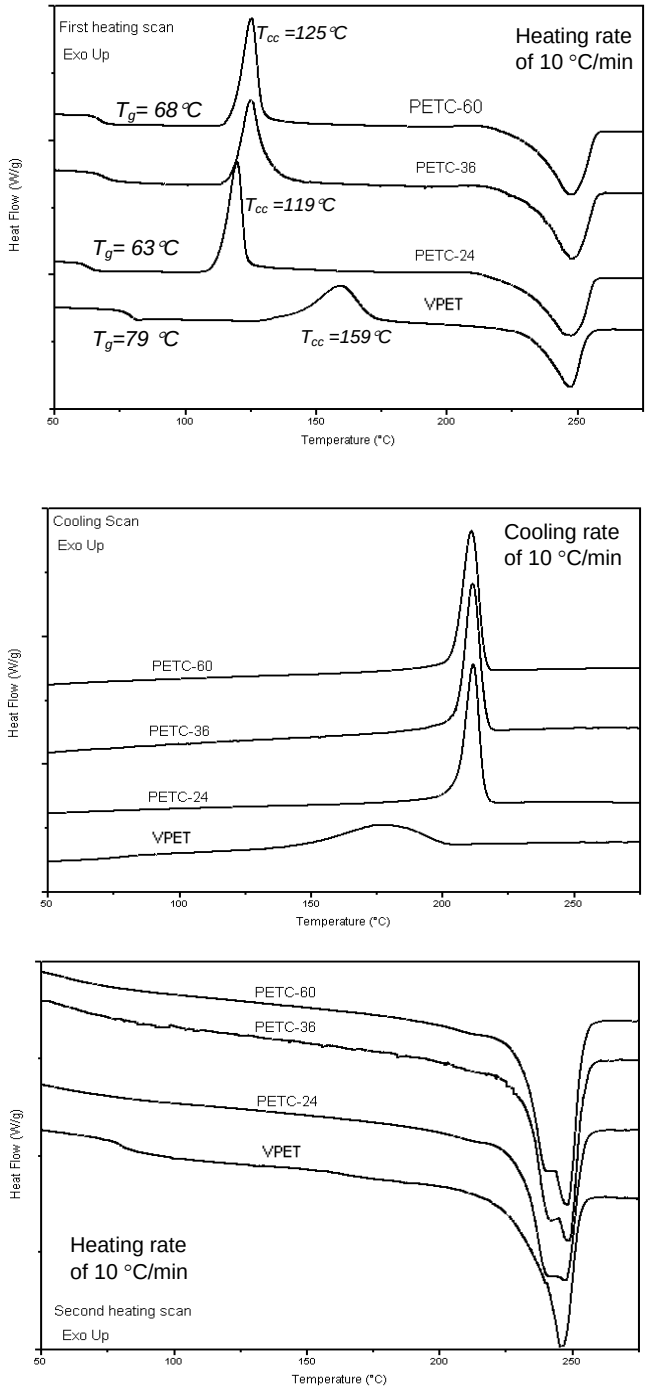

Figure 4.30 1st heating scan (a), cooling scan (b) and second heating scan (c) curves of cast PET dried for 24, 36, and 60 hours and virgin PET.

Table 4.3 First heating scan data of virgin and cast PET

Material	Cold crystallization				Melting		
	T_g (°C)	$T_{cc,onset}$ (°C)	T_{cc} (°C)	$\|\Delta H_c\|$ (J/g)	$T_{m,onset}$ (°C)	T_m (°C)	$\|\Delta H_m\|$ (J/g)
VPET	79	140	159	34	232	247	37
PETC-24	63	112	119	38	229	247	50
PETC-36	68	118	125	39	232	248	53
PETC-60	68	118	125	40	232	248	50

Table 4.4 Cooling and 2nd heating scan data of virgin and cast PET

Material	Hot-crystallization (Cooling scan)			Melting (Second heating scan)		
	$T_{hc,onset}$ (°C)	T_{hc} (°C)	$\|\Delta H_{hc}\|$ (J/g)	$T_{m,onset}$ (°C)	T_m (°C)	$\|\Delta H_m\|$ (J/g)
VPET	201	177	41	235	245	41
PETC-24	216	212	60	230	247	62
PETC-36	217	212	60	231	248	62
PETC-60	216	211	61	230	248	63

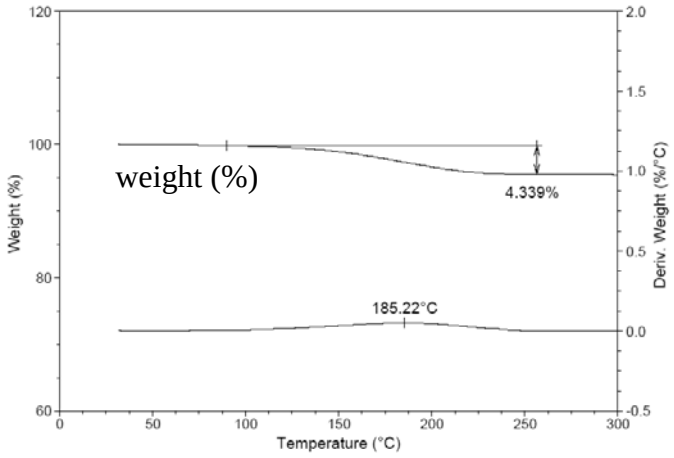

Figure 4.31 TGA result of the solvent cast neat PET which was dried in a vacuum oven for 36 hours. It shows a weight loss of 4.3% due to the residual phenol.

Both PETC-36 and PETC-60 exhibited the same T_g, indicating that they contained the same amount of residual solvent and this was tightly bound to the polymer that prevented its extraction at 80°C. The residual solvent acted as a

plasticizer also lowered the rheological properties of the cast PET compared to the unprocessed PET as shown in Figure 4.19. The presence of the residual solvent in the cast neat PET was supported by the TGA result as shown in Figure 4.31. The mass change with respect to temperature showed its peak at 185°C. This temperature is close to the boiling point of phenol (181.7°C).

From the first heating scan results, shown in Table 4.3, the cold-crystallization temperature, the crystallization from the amorphous state on heating, T_{cc} was 159°C for VPET, 119°C for PETC-24 and 125°C for both PETC-36 and PETC-60. The T_{cc} was, therefore, reduced by the presence of an amount of residual solvent. In general, when a polymer crystallises from the solid amorphous phase, the nucleation rate is high but the overall crystallization rate is limited by the crystal growth rate. The crystal growth rate of the solvent cast polymer increased because the polymer chain mobility increased due to the residual solvent that increased the free volume of the polymer matrix.

These results clearly show that the changes in the T_g and T_{cc} are related to the amount of the residual solvent. All of the cast samples exhibited a higher exotherm of cold-crystallization (ΔH_c) and a narrower cold-crystallization peak width (T_{cc} - $T_{cc,\ onset}$) than those of VPET. It indicated that the residual solvent promoted a greater degree of crystallinity and crystallization rate for PET. It is to be noted that there was no significant change in the melting point of the compound as shown in Figure 4.30(c).

The cooling scan thermograms in Figure 4.30(b) and Table 4.4 show that the hot-crystallization behaviour (i.e. crystallization from melt state during cooling) of VPET significantly differed from that of the PETC samples. The presence of residual solvent in the PET increased the hot-crystallization temperature (T_{hc}), crystallization

rate and degree of crystallinity. All the PETC samples exhibit identical increases of crystallization rate, T_{hc}, and crystallinity. These results indicated that the difference in the residual solvent levels did not affect the level of crystallinity, crystallization rate, and crystallization temperature of the samples tested.

During the second heating cycles shown in Figure 4.30(c), all the PETC samples exhibited double melting peaks, the first peak at 240°C and the second at 247°C. The unprocessed PET that had an equivalent thermal history exhibited only the second melting peak A similar phenomenon was found in PET/clay nanocomposites [106] and it was believed that the first peak observed in the nanocomposites probably originated from melting of the tiny crystals induced by the presence of clay during the cooling scan. In this work, all of the cast samples that were subjected to a similar thermal history showed two identical melting peaks possibly due to the presence of the solvent residue.

4.6 Effect of nanoclay on thermal properties

In order to study the effect of nanoclay on the thermal properties of PET, all of the nanocomposite samples were prepared by solvent blending with different sonication times. The samples were subjected to thermal analysis by DSC and the results are shown in Figure 4.32. The PETS10-24 samples that contained 5% by weight of nanoclay were sonicated for 10 minutes and dried for 24 hours. The other 5 wt% clay nanocomposite samples were labelled in the same way with the numbers relating to the sonication time and drying time respectively. It should be noted that the nanoclay suspension was sonicated before the addition of the polymer.

As described in the previous section, the 24 hour drying time did not extract the solvent from the samples to a base residual level. This was evident from the DSC

results that showed a variation in the values of the T_g and T_{cc} as shown in Figures 4.30(a) and 4.32(a). However both of the T_g and T_{cc} values of all the nanocomposite samples with the longer drying time of 72 hours showed little variation around a base value (Figure 4.32(b)). The presence of the nanoclay in PET did not change the T_g but it did lower the T_{cc} from 125°C for the unfilled cast resin to 108°C for the filled cast resin. The reason for the reduction of the T_{cc} is that the clay particles increased heterogeneous nucleation sites, resulting in an increase in the crystallization rate of PET nanocomposites.

The nanocomposite samples prepared with the use of the solvents did, however, lower the T_g of the virgin resin by 10°C but this was due to the presence of residual solvent in the samples and not from the presence of the nanoclay. Previous studies [106] have reported that the T_g of PET/clay nanocomposites prepared by melt blending was not changed by the addition of different contents of clay within the range of 1 to 5 wt%. Studies of PET nanocomposites filled with unmodified and modified calcium carbonate did, however, show 6°C and 14°C increases in the T_g, respectively [107]. Other workers have shown that a PET/silica nanocomposite synthesized by using an in situ polymerization method had a slight increase in T_g compared to pure PET [108]. For the work described here, it was shown that the degree of clay dispersion did not affect the thermal behavior of PET in the first DSC heating runs.

The cooling scan curves in Figure 4.32(c) revealed that the solvent cast PET with and without nanoclay possessed a similar T_{hc} and crystallization rate, suggesting that the residual solvent increased the crystallization rate during the crystallization from the melt. It was assumed that the residual solvent increased the polymer volume, resulting in an increase of the polymer chain mobility. For this reason, the crystal

growth rate would increase, leading to an increase in the overall crystallization rate. Figure 4.32(d) shows that the melting behaviour was not affected by the clay dispersion state, the residual solvent and its amount.

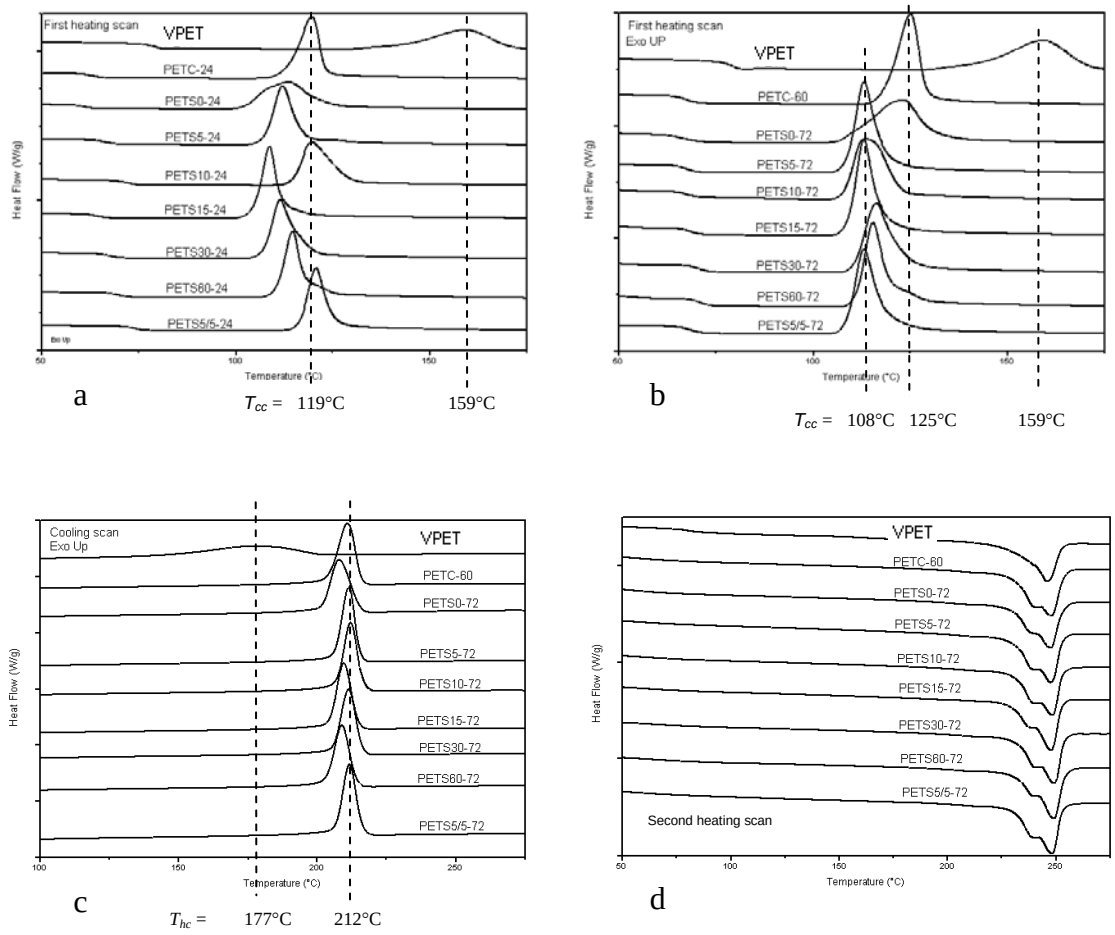

Figure 4.32 1st DSC heating plots of the nanocomposites with (a) 24 hour and (b) 72 hour drying time and the cooling plots (c) and 2nd heating plots (d) of the nanocomposites with a 72 hour drying time. (The heating and cooling rates were 10°C/min.)

4.7 Conclusions

The aim of this work was to produce a fully exfoliated clay/PET nanocomposite by solvent blending with the assistance of ultrasonication and the use of a compatibilizer. The morphological, rheological, mechanical, and thermal properties of the PET/clay nanocomposites were investigated. The conclusions of the study can be summarised as follows.

- The degree of separation and dispersion of the 10A organoclay in the PET matrix significantly increased with increasing the sonication times but did not increase after sonication for six hours.
- With these processing conditions, the development of a percolated network structure in the PET nanocomposite occurred at the 10A organoclay loading of 2.5 wt%.
- A network structure of clay particles was clearly observed on the nanocomposite cast film surfaces but not in the fracture surfaces as observed by SEM.
- The clay network structure was two-dimensional and mainly consisted of agglomerations of clay particles rather than individual clay layers.
- The tensile modulus and strength of the nanocomposite with a network structure increased by 17% and 13% respectively compared with those of the cast pure PET. The modulus improvement was still lower than the Halpin-Tsai evaluation that predicted 30% increase.
- The addition of the epoxy was able to increase the compatibility between the organoclay and the PET, and also acted as a diepoxide chain extender for the PET.

- The nanocomposite with the epoxy possessed a higher dispersion and a stronger network structure with longer, thinner stacks of the clay particles than the nanocomposite without the epoxy.
- The formation of the long, thin stacks was possibly due to the PET extension chains that produced a bond between the clay layers. The long, thin stacks were, therefore, unable to be further separated by sonication.
- The application of melt shearing in a mini twin screw extrusion was, however, able to further break and to disperse the long, thin particles throughout the matrix that resulted in a higher level of separation and dispersion.

This work also attempted to understand the effect of a clay network structure on the tensile properties of a nanocomposite. Figure 4.28 shows a schematic diagram of the relationship between morphology and rheology to the degree of clay dispersion in PET, based on the experimental data in this study. At a low degree of clay dispersion, Figure 4.28(a), the short, thick clay particles changed the viscous liquid-like behaviour of neat PET to an elastic behaviour of the clay-PET nanocomposites. The clay particles in this low-dispersion system had a low aspect ratio of about 4. When the degree of dispersion increased, Figure 4.28(b), the number of clay particles was higher, and size of the particles was thinner and longer with a higher aspect ratio of about seven. The higher-dispersed system exhibited a plateau behaviour with $G' > G''$ at low frequencies. This indicated a much stronger elastic behaviour with the presence of a clay network structure. Despite the significant change in the rheological behaviour especially at low frequencies, the aspect ratio of the particles was not as high as in a fully exfoliated system such as that reported in PA6 nanocomposites(particle aspect ratio of about 50-100) [64]. The excellent potential tensile modulus (30% increase as predicted by the Halpin Tsai equation) for the PET

nanocomposites with 2.5 wt% clay still was not achieved and it implied that the two-dimensional network structure of clay particles that was developed in the processing did not have a strong effect on the tensile properties.

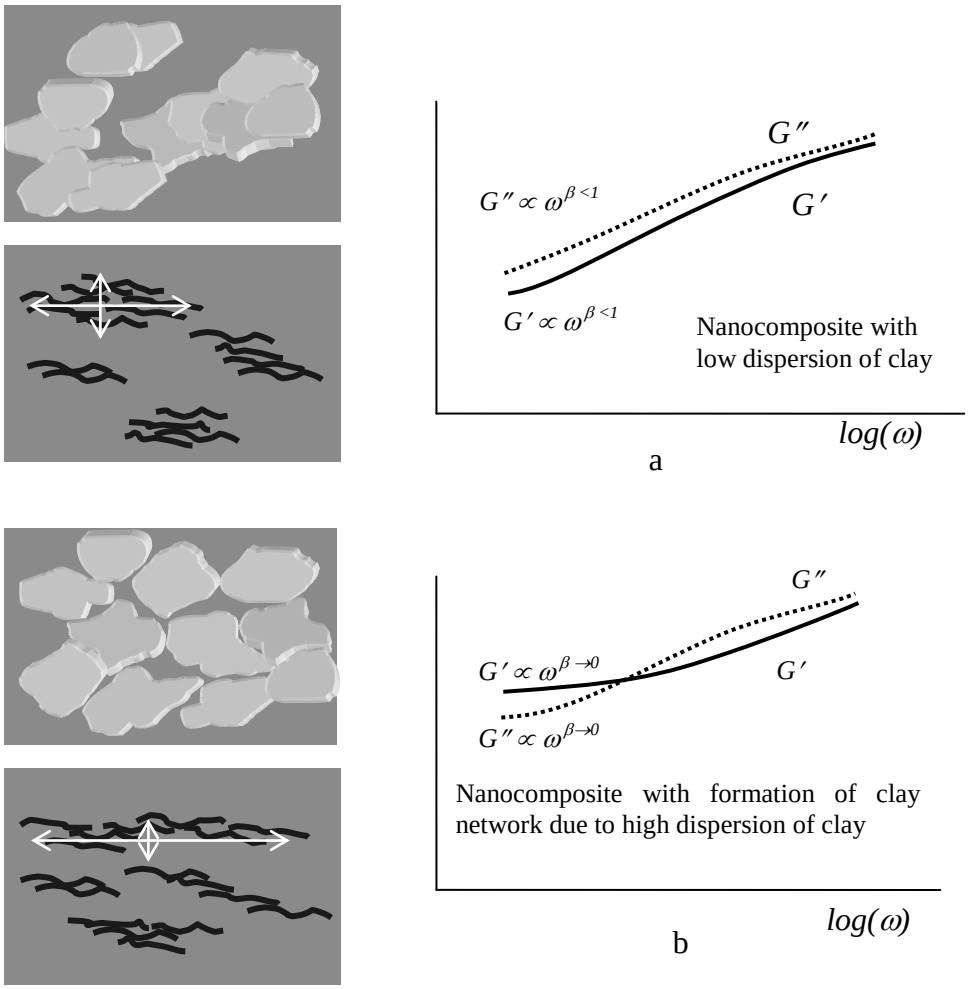

Figure 4.33 The schematic diagram of relation between morphology and rheology to the degree of clay dispersion.

In summary, the degree of dispersion as observed by SEM and TEM was correlated with the rheological behaviour and tensile properties of the PET nanocomposites. This resulted in an understanding of the effect of the processing conditions required to enhance the nanoparticle dispersion/exfoliation in a PET/organoclay nanocomposite.

Chapter 5

PET/organoclay Nanocomposites by melt blending

5.1 Introduction

This chapter describes the effect of the amount of surfactant on the morphological, rheological and tensile properties of the melt blended nanocomposites. The chemical structure and amount of surfactant used in an organoclay strongly affects the exfoliation of clay layers in a polymer matrix [18]. Recently, Urko et al. [29] investigated the amount of the surfactant necessary to produce nanocomposites by dispersing two commercial organoclays, Cloisite 15A (15A) and Cloisite 20A (20A), in PET. The same surfactant was used in both organoclays i.e. dimethyl, dehydrogenated tallow, quaternary ammonium (2M2HT). However, the content of the surfactant in the 20A is less than that in the 15A as shown in Figure 5.1. The surfactant has two long alkyl groups (dehydrogenated tallow) that reduce the potential for the diffusion of the polymer chains between the clay particles [43]. XRD results [29,47] showed that PET chains more easily intercalated the clay layers of the 20A

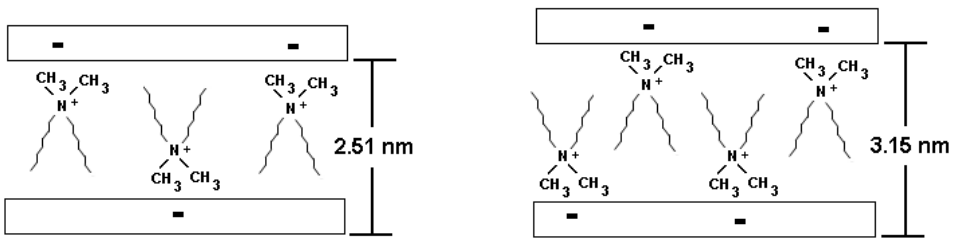

(a) (b)

Figure 5.1 Organoclay surfactant of (a) 20A with CEC of 95 meq/100g and (b) 15A with CEC of 125 meq/100g.

than those of the 15A due to the lower number of non polar groups in the 20A that resulted in an improved dispersion of nanoclay in the PET matrix.

A second pair of commercial organoclays, Cloisite 10A (10A) and Nanofil-2 (N2) were studied. Both of these had been treated with the same surfactant (Figure 5.2), dimethyl, benzyl, hydrogenated tallow, quaternary ammonium (2MBHT). The content of the surfactant in the N2 was, however, less than that in the 10A that resulted in a difference in the interlayer distances (1.8 nm for N2, 1.92 nm for 10A). The surfactant of the 10A and N2 had one long alkyl tail instead of two long alkyl tails, as in that of the 15A and 20A. The polymer molecules were more easily able to intercalate the galleries of the clay with one-tailed surfactant than those of the clay with two-tailed surfactant, as evidenced by XRD [47]. In chapter 4, solvent blending was used to disperse the 10A and the N2 in PET. With this process there was no risk of degradation of the surfactant. It was found that the 10A possessed a higher degree of dispersion than the N2.

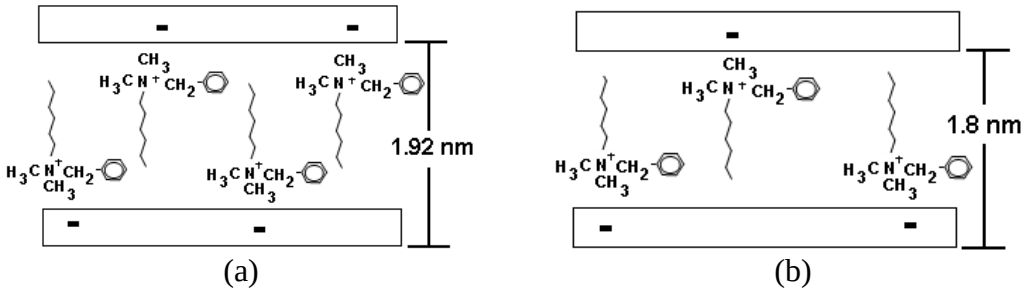

Figure 5.2 Organoclay surfactant of (a) 10A with CEC of 125 meq/100g and (b) N2 with CEC of 75 meq/100g.

In melt blending, the processing temperature of PET was higher than the decomposition temperature of the 10A surfactant based on quaternary ammonium salt [42] and consequently some thermal degradation of the surfactant was expected. It might be assumed, therefore, that the lower surfactant concentration in the N2 may

result in a reduced effect of the degradation of the surfactant, giving the potential for better morphological and physical properties of the nanocomposite than with the 10A clay. The objective of the work described in this chapter work was to disperse the 10A and N2 in PET (IV of 0.54 dL/g) using twin screw extrusion technology in order to investigate the effects of the modifier content on the morphology, rheology, tensile properties, crystal structure, and isothermal crystallization behaviour of the nanocomposites. The effect of the processing temperature in the range 255-280°C was investigated.

5.2 Morphology

Samples for SEM observation were taken from compression moulded films of the extruded PET nanocomposites. The morphology of the samples was observed on both film cross-section (fracture surfaces) and film surfaces (moulded surfaces) as shown in Figure 3.1. The nanocomposite films in the semicrystalline state were brittle. The brittle films were easily fractured to produce the cross section surfaces for examination. Prior to SEM, the surfaces were treated by an oxygen-plasma technique to reveal the clay particles within the PET. The samples were finally coated with platinum to obtain conductive samples for SEM.

SEM micrographs of the fracture surfaces of PET nanocomposites with 2.5 wt% of 10A (C-10A) are shown in Figure 5.3. The clay particles are clearly observed in the treated surfaces. The low magnification image in Figure 5.3(a) reveals that the clay particles are finely and randomly dispersed in the matrix. At a higher magnification in Figure 5.3(b), it is clearly observed that the edges of the clay particles emerge from the matrix.

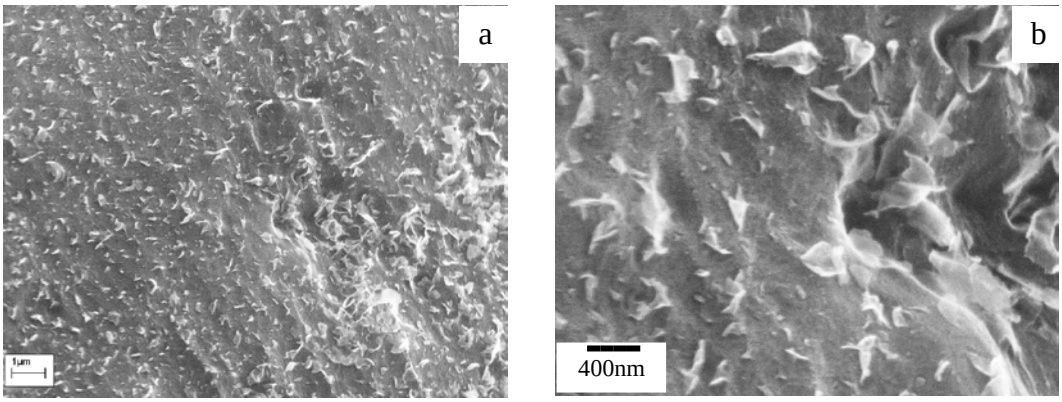

Figure 5.3 SEM images of a fracture surface of C-10A.

Figure 5.4 shows the morphology of the moulded surfaces of C-10A and it reveals the surface areas of the clays rather than the clay edges. The low magnification image, Figure 5.4(a), shows that the organoclay was dispersed throughout the matrix and many large clay agglomerates or tactoids, see in the circles, were observed. At the larger magnification, Figure 5.4(b), the agglomerates of clay are clearly seen. These dispersed particles did not, however, connect together to form a network of clay particles because the number of particles dispersed was not high enough to develop a network of clays. If the agglomerates had been further dispersed, a network of clays could have formed. The combination of the fractured and moulded surface images of the samples indicated that C-10A possessed a mixture of intercalated and tactoid structures without the formation of a network structure of the clay particles.

The morphology of PET nanocomposites with 2.5 wt% of N2 (C-N2) in Figures 5.5 and 5.6 was also observed in the fractured and moulded surfaces of the samples using SEM. The surfaces of C-N2 displayed a larger and greater number of agglomerates of clay particles than C-10A. These results indicate that Cloisite 10A dispersed in the PET matrix better than Nanofil 2, possibly as a result of the higher

content of the modifier in the organoclay of the 10A that gave it a higher hydrophobicity than the N2.

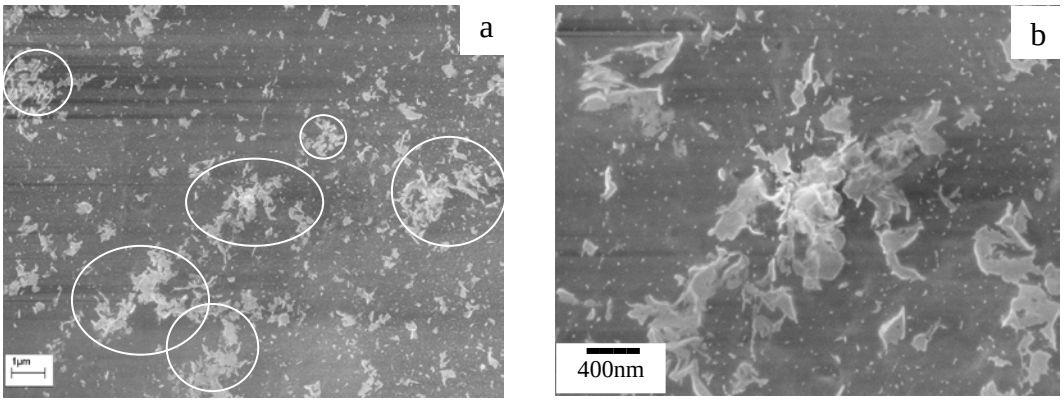

Figure 5.4 SEM images of a moulded surface of C-10A.

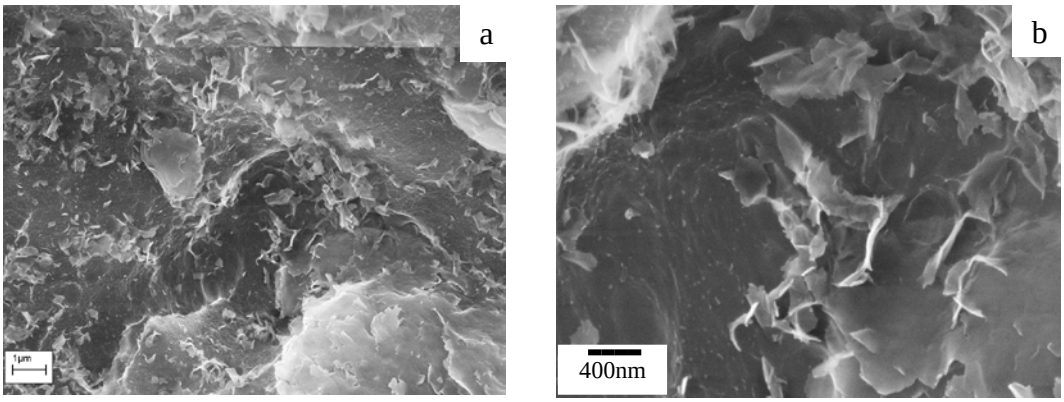

Figure 5.5 SEM images of a fracture surface of C-N2.

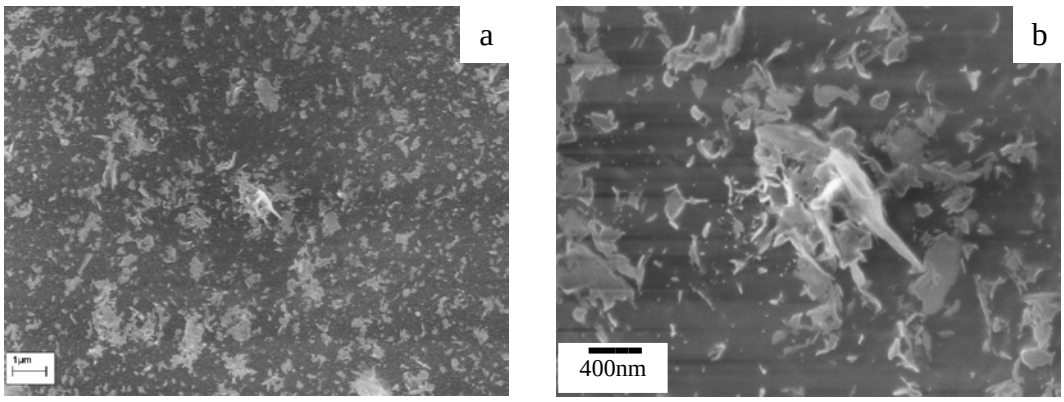

Figure 5.6 SEM images of a moulded surface of C-N2.

5.3 Melt rheology

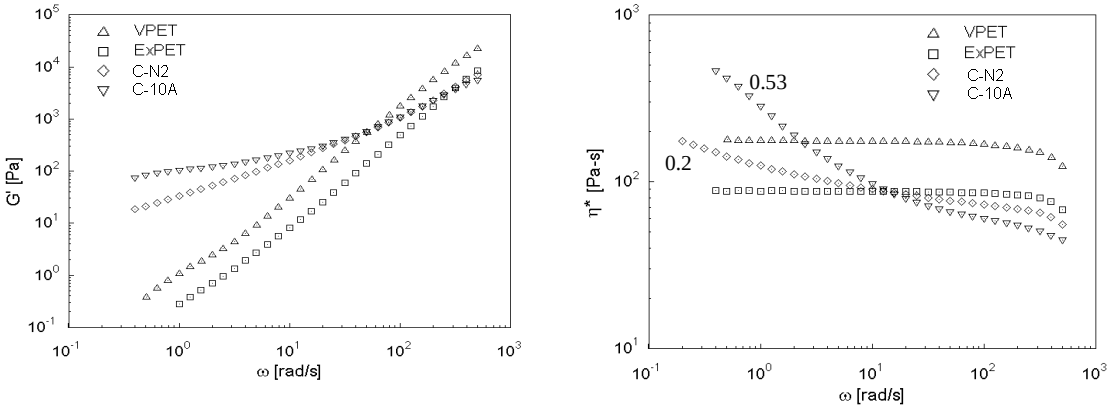

Figure 5.7(a) Storage modulus and (b) Complex viscosity of VPET, ExPET and PET/organoclay nanocomposites.

Figure 5.7 illustrates the storage modulus (G') and complex viscosity (η^*) of the virgin PET (VPET), extruded PET (ExPET), C-10A and C-N2. The samples were tested at 270°C with 10% strain amplitude. The shape of G' curves of the ExPET and the VPET followed a similar trend with the former being less than that for the latter over the whole frequency ranges. The reduction of G' indicated that the PET thermally degraded during the extrusion process [37,105,106]. The decrease in the molecular weight of PET as a result of thermal degradation during the extrusion was examined by intrinsic viscosity (IV) measurements as described in section 3.9. Table 5.1 shows that the IV of the PET dropped from 0.54 to 0.47 dL/g during the melt compounding.

Table 5.1 Intrinsic viscosity of the VPET, ExPET, and nanocomposites

Samples	IV (dL/g)
VPET	0.54
ExPET	0.47
C-N2	0.45
C-10A	0.41

The rheological responses of the nanocomposites were dominated by the clay at low frequencies and by the matrix at high frequencies [60]. At low frequencies, G' of the nanocomposites was greater than that of the unfilled PET due to the clay particles restricting the movement of the PET chains as shown in Figure 5.7(a). At high frequencies, the clay particles did not appear to affect the movement of the PET chains and consequently the G' of the nanocomposites was similar to that of ExPET. Similar rheological responses of nanocomposites to the testing frequency/amplitude have been reported for PC/PBT-clay nanocomposites [109] and for PC-clay nanocomposites [110,111].

The C-10A had a higher G' than the C-N2 in the low frequencies as shown in Figure 5.7(a). In general, a high dispersion of the clay provides large areas of clay layers strongly interacting with the polymer chains, resulting in the increase of G' especially at low frequencies. This result indicates that the dispersion of the 10A is better than that of the N2, in agreement with the SEM results. It implies that the 10A is more compatible with PET than the N2. The higher surfactant content is believed to be the reason for this.

Figure 5.7(b) shows the complex viscosity (η^*) for all samples. The complex viscosities of the VPET and the ExPET demonstrate a Newtonian fluid response in the frequency range up to approx 10^2 rad/s. Both nanocomposites showed that shear thinning was occurring throughout the frequency range and was more pronounced at low frequencies. The value of η^* of the ExPET was less than that of the VPET in all frequency range. This was due to the loss in PET molecular weight as indicated by the reduction of intrinsic viscosity shown in Table 5.1. The same rheological results in a study of PET were observed by Vidotti [45]. Sanchez-solis et al. [112] reported that the rheological properties and the molecular weight of the extruded PET were lower

than those of the neat PET. This indicated the decrease in the rheological properties of the extruded PET was due to the degradation of PET during the extrusion.

The shear thinning index (α) of η^* ($\eta^* \propto \omega^{\alpha}$) at low frequencies is a useful parameter to compare the degree of dispersion of clay [63] and has been discussed in chapter 2. The dispersion state of nanocomposites with a high shear-thinning index is better than that of nanocomposites with a low shear-thinning index. In this work, the shear-thinning index changed from zero for the unfilled PET to 0.2 for the C-N2 and to 0.53 for the C-10A. The greater shear thinning indicates that the 10A is more compatible with the PET than the N2, resulting in a greater dispersion of clay in C-10A.

At high frequencies, the value of η^* for the materials are in the following order: VPET > ExPET > C-N2 > C-10A. The reduction in η^* of the nanocomposites was due to the level of degradation of the polymer. Table 5.1 shows that the IV of the nanocomposites, especially the 10A nanocomposite, was lower than the extruded PET. It has also been reported that the 15A, 20A and 10A were degraded during melt blending under nitrogen and consequently caused molecular weight degradation of recycled PET by hydrolysis reaction [47]. The decomposition of the 10A and 20A provided chloromethane and water as major volatile by-products [113]. This was attributed to the PET hydrolysis degradation. The TGA results of the 10A and N2 organoclays in Figure 5.8 show that the thermal decomposition temperature of both organoclays was lower than the typical melt processing temperature of PET (255-280 °C). This implies that the loss in molecular weight of the PET in the nanocomposites resulted from not only the high shear heating in the extruder, but also the degradation of the organoclay.

The C-10A showed the lower complex viscosity than the C-N2 at high frequencies. The IV of the 10A-nanocomposite was also lower than that of the N2-nanocomposite (Table 5.1). This indicates that the PET molecular weight decreased with increasing the surfactant content. Figure 5.8 shows that increasing the amount of the surfactant lowered the thermal stability of the organoclay. This result explained why the PET matrix of the C-10A nanocomposite degraded more than that of the C-N2 nanocomposite. The reduction of molecular weight due to increasing the surfactant content was also found in the blending of recycled PET with the 20A and the 15A [47]. In addition, the greater molecular weight degradation in the 10A nanocomposite could also be attributed to a higher dispersion of the 10A in the PET. The higher dispersion increased the exposure of the polymer to the surfactant on the organoclay surfaces [114].

In summary, the rheological properties and the SEM images confirmed that the C-10A possessed a greater dispersion of the clay than the C-N2. The degradation of the organoclay did not hinder the dispersion of the organoclay.

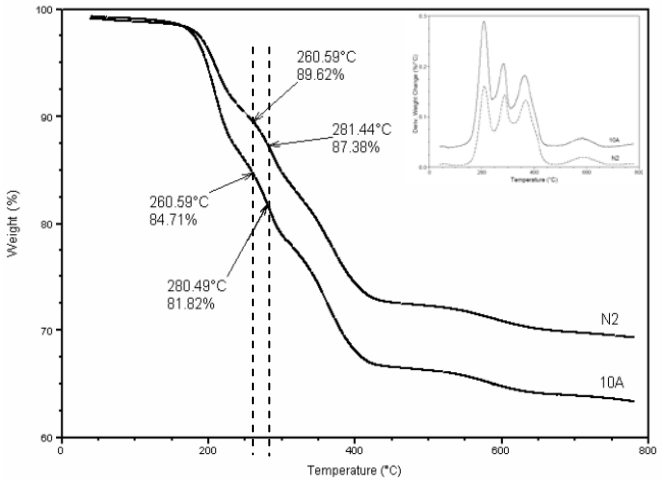

Figure 5.8 TGA thermograms of Cloisite 10A and Nanofil 2.

5.4 Mechanical properties

The tensile specimens of PET/clay nanocomposites were produced by an injection moulding. The dumb-bell specimens were 3.3 mm thick according to ASTM D638. The barrel temperature was set to 255-265°C and the mould temperature was set at 30°C. With these conditions, the moulding consisted of two layers, a core and a skin. The core layer appeared opaque indicating a semicrystalline structure, while the skin layer was transparent, indicating an amorphous structure. The explanation for this is as follows:

When the molten PET/clay nanocomposite was injected into the cold mould, the melt against the cavity walls was rapidly quenched to produce a solid layer (skin) with an amorphous structure. The solid layer had low thermal conductivity, thus limiting the heat transfer from the remaining melt in the core to the cavity walls. The cooling rate at the core was therefore lower than that at the skin. Furthermore, it was concluded that the clay particles acted as an effective nucleation agent to induce PET-crystallization in the core of the moulding. As a consequence, the tensile specimens of PET/clay nanocomposites possessed the two-layered structure of an amorphous skin with a semicrystalline core.

The mechanical properties of the injection-moulded specimen were influenced by the nature of the two-layered structure with polymer chain and clay orientations. To investigate the tensile properties of the crystalline and amorphous layers and the effects of surfactant content on these properties, amorphous and semicrystalline films were prepared by compression moulding with different moulding temperatures. The compression films would not include any effects of particles or molecular orientation that could result from injection moulding.

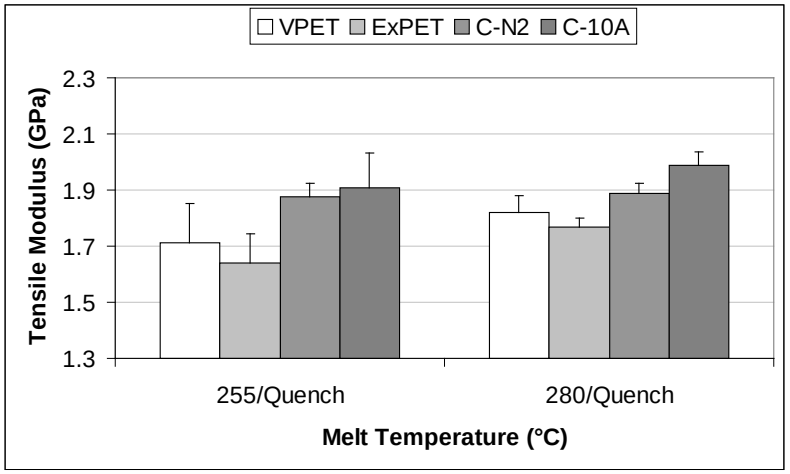

a

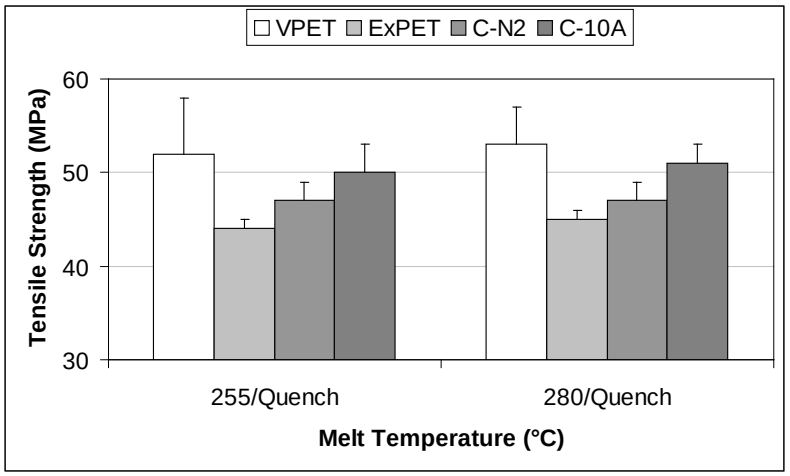

b

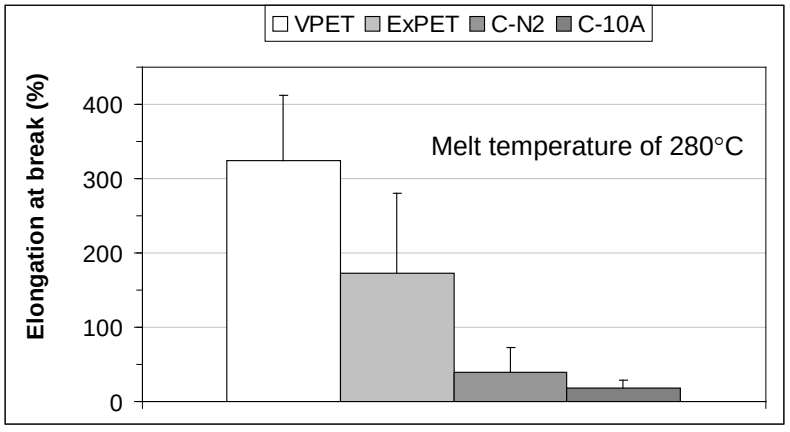

c

Figure 5.9 (a) Tensile modulus, (b) Tensile strength, and (c) elongation at break of *amorphous* films of VPET, ExPET and PET nanocomposites.

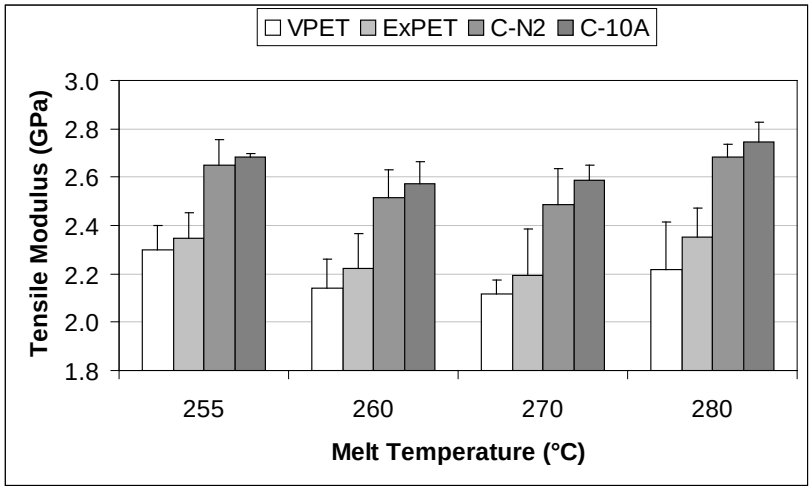

a

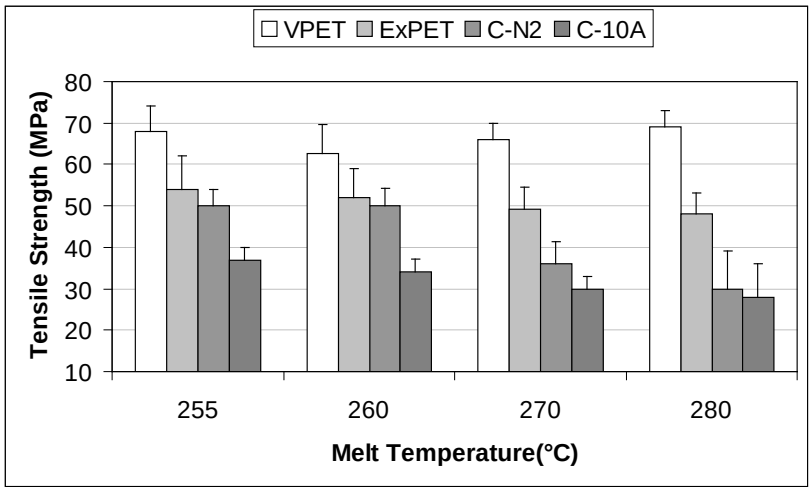

b

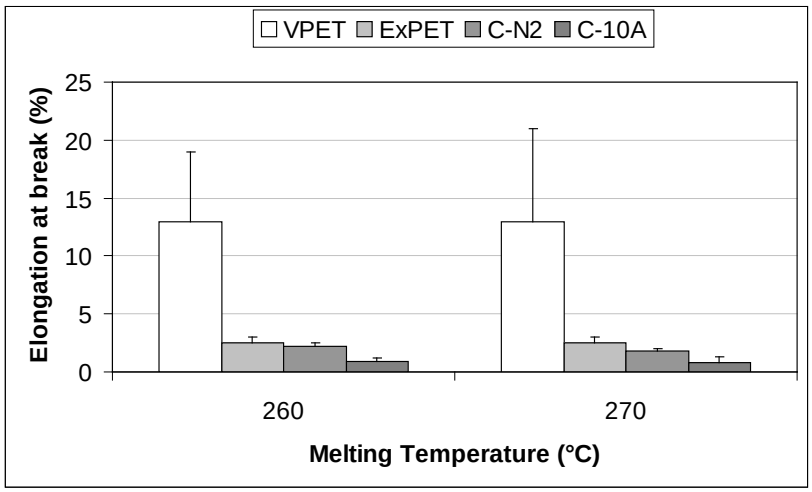

c

Figure 5.10 (a) Tensile modulus, (b) Tensile strength and (c) Elongation at break of *semicrystalline* films of the VPET, ExPET, and nanocomposites that were isothermally crystallised at 200°C for 10 minutes after cooling from the set melt temperature at 40°C/min

Figure 5.9 shows the tensile properties of amorphous compression moulded samples of the VPET, ExPET, and two PET nanocomposites using an extension rate of five mm/min. The molten films were rapidly quenched after being held under compression at 255 and 280°C for three minutes in order to study the effect of the compression moulding temperature on the mechanical properties. The amorphous films were 0.15 mm thick. The results show that the moulding temperature had little effect on the modulus and strength of the unfilled and filled PET. Compared with the ExPET, the moduli in Figure 5.9(a) were enhanced by 15% for the C-10A and by 11% for the C-N2. In Figure 5.9(b), both nanocomposites had a lower strength than the VPET but they had a superior strength to the ExPET that had an equivalent thermal history. The C-10A showed a higher modulus and strength than the C-N2, indicating that the 10A-organoclay had a better dispersion in PET than the N2-organoclay.

Figure 5.10 shows the mechanical properties for all crystalline samples held under compression at the different melt temperatures of 255, 260, 270 and 280°C for three minutes. The molten films were cooled at a rate of 40 °C/minute to 200°C, maintained at this temperature for ten minutes and then rapidly quenched. The thickness of semicrystalline films was 0.15 mm. The moduli of all samples were not affected by the melt temperature as shown in Figure 5.10(a). The moduli were enhanced by 17% for the crystalline C-10A and 13% for the crystalline C-N2 relative to the crystalline ExPET. The tensile strength of the crystalline VPET and the crystalline ExPET did not change with the melt temperature. The tensile strength of the nanocomposites presented in Figure 5.10(b) was, however, less than that of the VPET and ExPET and decreased with increasing melt temperature.

Interestingly, the crystalline C-N2 exhibited a higher tensile strength than the crystalline C-10A for all the melt temperatures. Compared to the amorphous C-N2 in Figure 5.9(b), the crystalline C-N2 had a higher tensile strength from a melt temperature of 255-260°C. When the melt temperature was higher than 260°C, the strength of the crystalline C-N2 decreased significantly and was lower than that of the amorphous C-N2. The tensile strength of the crystalline C-10A was much lower than that of the amorphous C-10A and decreased with increasing melt temperature. Based on the tensile strength results, the processing temperature for the N2-organoclay should not be raised above 260°C. All of the processing temperatures used for the crystalline 10A nanocomposites produced a lower tensile strength than the crystalline N2 nanocomposite.

The TGA results in Figure 5.8 show that the N2-organoclay was more thermally stable than the 10A-organoclay at the PET processing temperatures. At 260°C the weight loss was 10% for the N2-organoclay and 14% for the 10A-organoclay. With the processing temperature of 260°C, the tensile strength, Figure 5.10(b), slightly decreased for the crystalline C-N2 and considerably decreased for the crystalline C-10A compared with the ExPET. At 270°C or 280°C, the N2 showed weight loss of 13% or more and this point coincided with the processing temperature at which the strength of the N2-samples dramatically decreased. The low thermal stability of the organoclay appeared to reduce the tensile strength of the crystalline nanocomposites. However, it seemed not to affect the strength of the amorphous nanocomposite.

In general, the elongation at break of a polymer significantly decreases with the addition of organoclays. For example, the elongation at break of fully exfoliated clay PA-6 and PA-66 nanocomposites decreased with organoclay loadings above 4.5

wt% and 1.5 wt%, respectively [115]. The elongations at break of the amorphous and the crystalline VPET, ExPET, and PET nanocomposites are shown in Figures 5.9(c) and 5.10(c) respectively. The breaking strain of the PET nanocomposites, especially C-10A, was lower than the unfilled systems. With either the amorphous or semicrystalline structure, the C-N2 had a higher breaking strain than the C-10A, despite the lower clay dispersion in the C-N2. A greater molecular weight degradation of the C-10A matrix than C-N2 matrix could be a possible cause for the lower breaking strain.

5.5 Relation between crystal structure and tensile properties

The investigation of the relationship between the crystalline structure and the mechanical properties of unfilled and filled PET based on nanoclay is discussed in this section. The granule samples were melted and compressed at 280°C for three minutes. The molten and compressed films were cooled from 280°C at a rate of 40 °C/minute to a temperature between 200, 210, and 215°C before immediately quenching to room temperature to obtain the films with different levels of crystallinity. The examination of crystallinity was explained in section 3.12 in chapter 3. The crystalline structures of the samples were observed through a polarized light microscope (PLM). The tensile properties were investigated using a Hounsfield H10KT instrument. The PLM results are shown in Figures 5.11(a), (b) and (c), 5.12 are for the VPET and Figures 5.13(a), (b) and (c), 5.14 for the C-10A.

The PLM images of VPET in Figures 5.11(a) and 5.11(b) show the initial stage of the growth of the spherulites The spherulites continued to grow until they impinged on each other, resulting in the spherulitic boundary lines clearly seen in Figure 5.11(c). The average diameter of the spherulites with a perfect Maltese cross pattern was about 40-50 μm, and is similar to Imai and Kaji's measurement [116]. Figure 5.12 shows that the modulus and strength of VPET increased linearly with increasing crystallinity. The crystallinity measurement was explained in section 3.12 in chapter 3.

The nanocomposites of C-10A crystallised at a higher temperature and crystallised faster than the unfilled polymer. Figure 5.13 shows that the spherulites were less well-defined than the unfilled polymer. At the final crystallization stage, Figure 5.13(c), the spherulite size was about 10-15 μm. In the filled system, the

tensile strength decreased linearly with the increase of crystallinity as seen in Figure 5.14. The decrease will be discussed later.

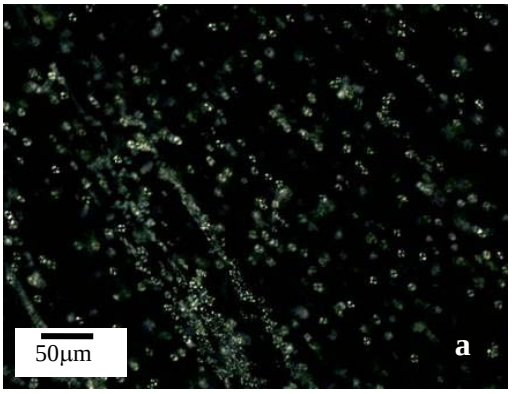

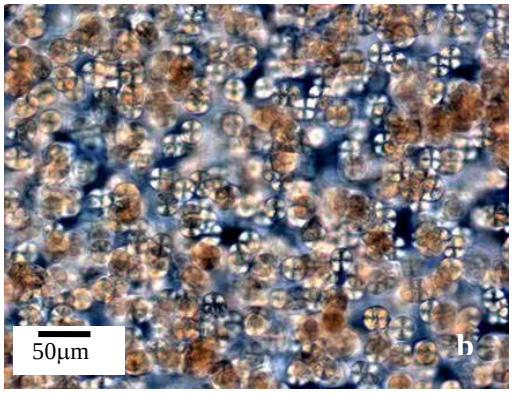

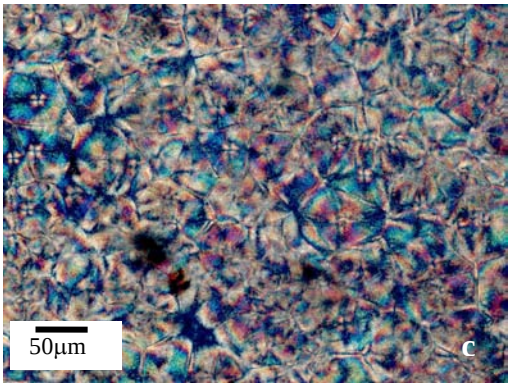

Figure 5.11 PLM images of the virgin PET samples. (a) and (b) were rapidly quenched from a temperature of 210°C and 200°C, respectively. (c) was rapidly quenched after crystallisation at 200°C for 10 minutes. Their tensile properties are shown in Figure 5.12.

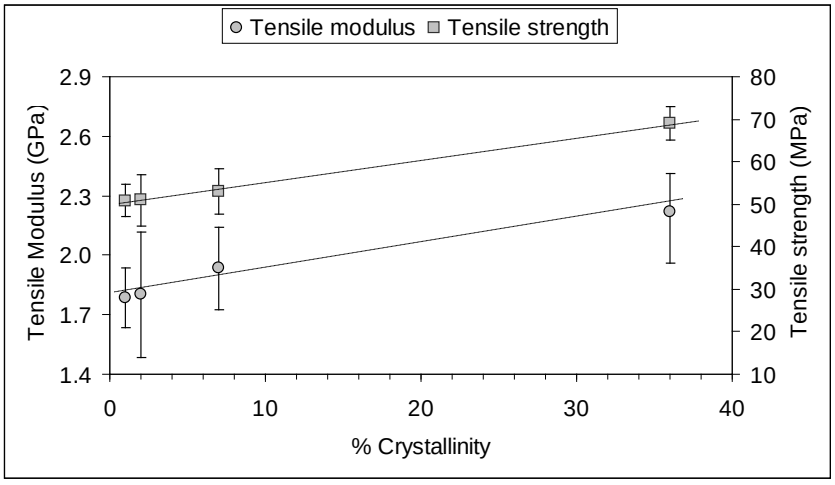

Figure 5.12 Tensile modulus and strength plotted against different % crystallinity by quenching the melt VPET from different temperatures of 280, 210, 200°C, and after crystallization at 200°C for 10 minutes.

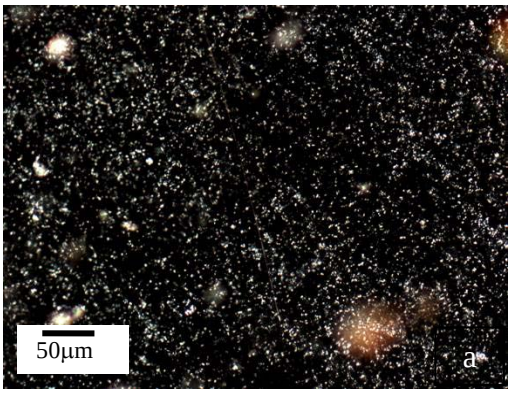

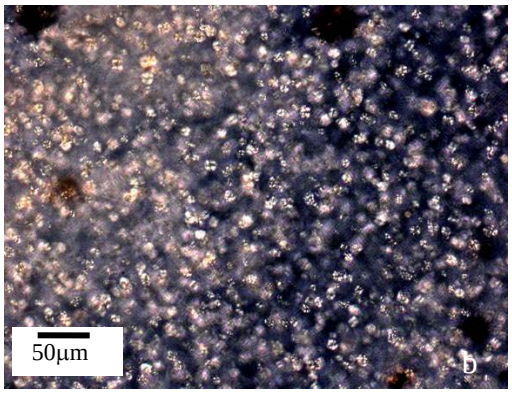

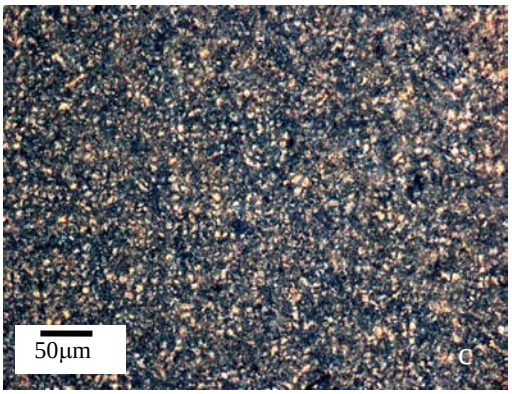

Figure 5.13 Spherulite structures of C-10A samples. (a) and (b) were rapidly quenched from a temperature of 215°C and 210°C, respectively. (c) was rapidly quenched after crystallisation at 200°C for 10 minutes. Their tensile properties are shown in Figure 5.14.

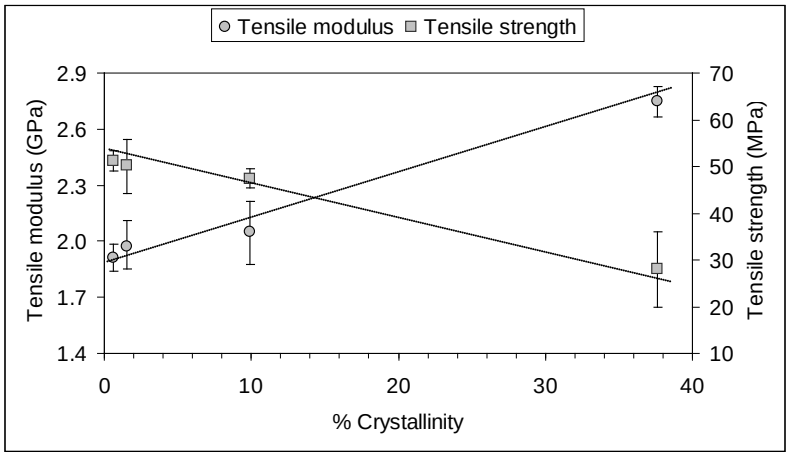

Figure 5.14 Tensile properties of C-10A with different % crystallinity by quenching the melt of C-10A from different temperatures of 280, 215, 210°C, and after crystallisation at 200°C for 10 minutes.

Figure 5.15 shows the spherulites of the extruded PET. The spherulite size of less than 20 μm for the extruded PET was less than the 50 μm size of the spherulites of the neat PET. A decrease in size and perfection of the spherulites after an increasing number of processing heat cycles has been reported in nylon 6 [117]. When PET was subjected to high shear and temperature, the polymer chains were broken due to the material's encounter with a degrading agent such as temperature, oxygen, mechanical stresses, and water [118]. The extruded PET could also have been contaminated by impurity particles from the extruder. Figure 5.16 shows the spherulites of the neat PET and the extruded PET observed using PLM. Both samples were melted and cooled from 270°C to 210°C at rate 40°C/min and then rapidly quenched. The PLM images clearly revealed that the extruded PET had a higher number of spherulites than the neat PET. This showed that the rate of nucleation of the extruded PET was greater than the neat PET at the set crystallization conditions. This resulted in the larger number of smaller spherulites present in the extruded PET than those in the neat PET.

The crystalline structure of the nanocomposites was further investigated using SEM. Fracture surfaces were obtained from the compression moulded film tensile specimens. The molten and compressed samples were cooled from 280°C at a rate of 40 °C/minute to 200°C, crystallised at this temperature for 10 minutes, and then rapidly quenched. The neat PET was fractured after cooling in liquid nitrogen. The extruded PET and the nanocomposites were fractured at room temperature. The fracture surfaces of all samples were etched by a KOH/methanol solution for 1 hour. This removed some of the amorphous material on the surfaces to clearly reveal the spherulites as shown in Figure 5.17. The average spherulite size obtained from these SEM images was 38 μm for the VPET, 14 μm for the ExPET, 12 μm for the C-10A

and 8 μm for the C-N2. The difference in the size of the spherulites can be seen in Figure 5.17. It seemed that the 10A and N2 organoclays did not contribute significantly to the heterogeneous nucleation in PET although the N2 appeared to be more efficient than the 10A (see Figure 5.17). The spherulites of the neat PET in Figure 5.17(b) and the extruded PET in Figure 5.17(d) consisted of lamellar fibrils symmetrically radiating from the centre. Figures 5.17(f) and (h) shows that the spherulites in the nanocomposites were not as symmetrical as those observed in the unfilled samples. In Figure 5.17(b), the straight lines of the spherulite boundaries are clearly seen. These boundaries were not as clear in the extruded PET, Figure 5.17(c), and the nanocomposites, Figures 5.17(f) and (h).

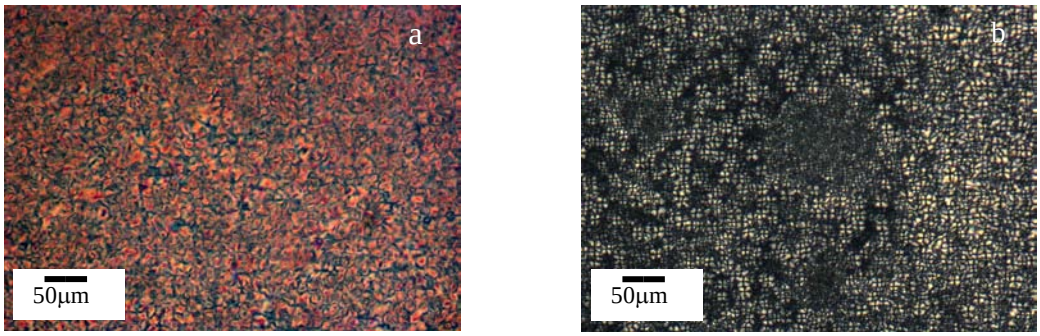

Figure 5.15 Spherulite structures of extruded PET (a) compression moulding film (b) casting film.

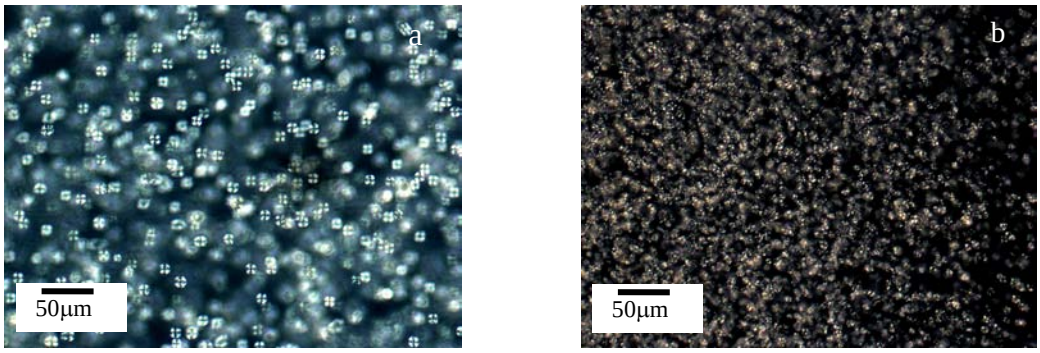

Figure 5.16 PLM images of (a) the virgin PET and (b) the extruded PET

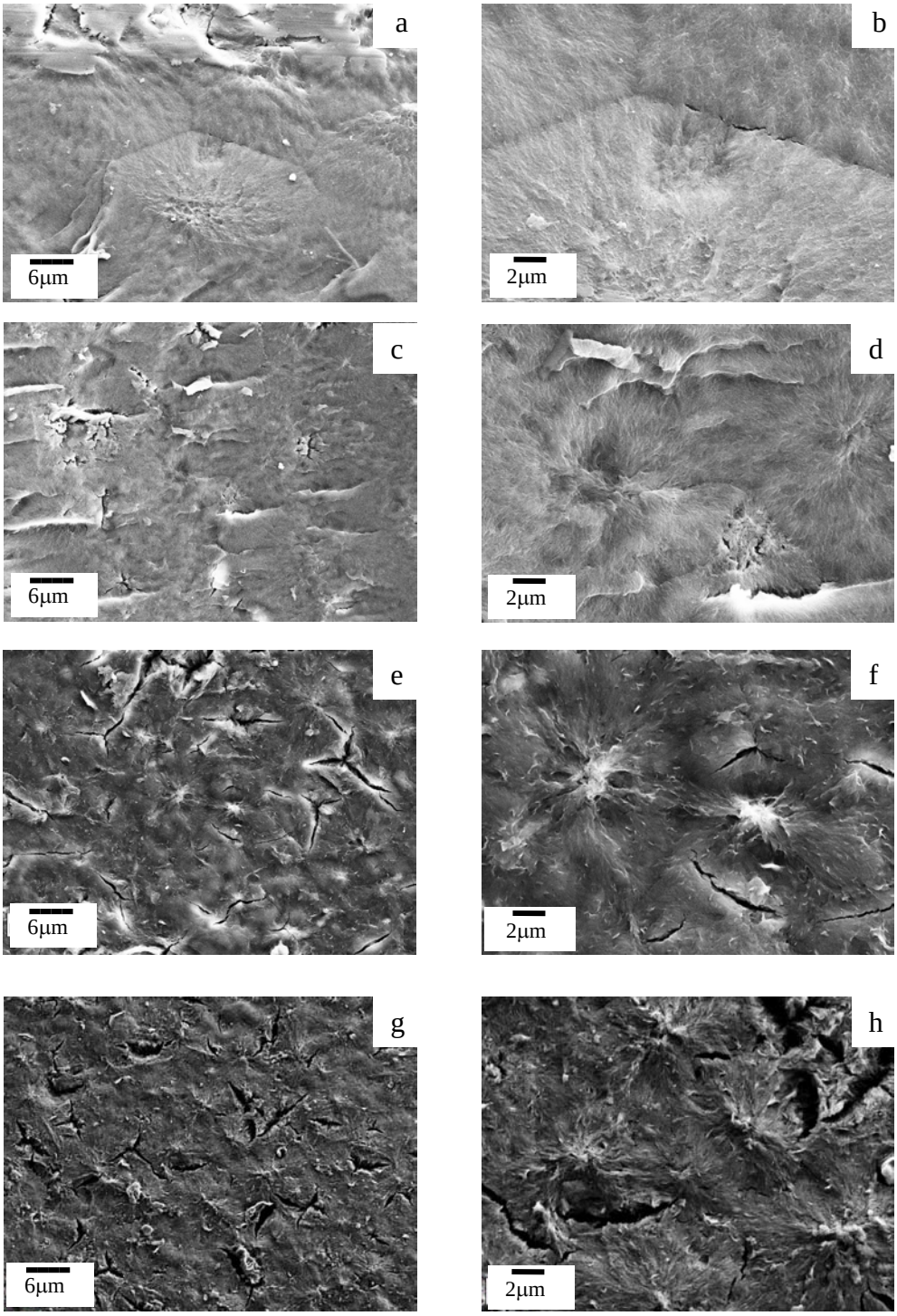

Figure 5.17 SEM images of fracture surfaces of VPET (a, b), ExPET (c, d), C-10A (e, f), C-N2 (g, h) which were etched in KOH/methanol

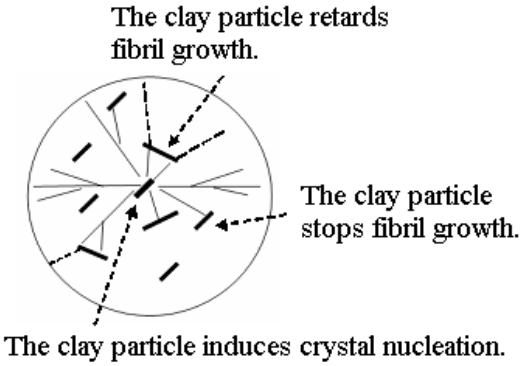

Figure 5.18 Schematic shows clay particles retarded or stopped fibril growth.

Figures 5.17(f) and (h) show the spherulites of the crystalline C-10A and C-N2 nanocomposites respectively. The small white lines present in Figure 5.17(f) are the edges of clay particles that were revealed by a KOH/methanol etching. It was expected that the clay particles that were dispersed in the matrix would have effectively nucleated the spherulites and consequently would have produced a large number of small spherulites. These images, however, reveal that the majority of the clay particles in the matrix did not induce spherulite nucleation. In fact, the particles could inhibit or stop the lamellar fibrils growing when their growth front hits the large surface areas of the clay particles [119,120] as shown in the schematic, Figure 5.18. This could retard the crystallization of the PET nanocomposites by reducing the crystal growth rate.

Figure 5.17(h) shows that the spherulites of the C-N2 were smaller than these of C-10A, Figure 5.17(f). The difference in the extent of clay dispersion in the PET matrix between the C-10A and C-N2 might be the reason. The SEM results in section 5.2 showed that the C-N2 in Figure 5.6(a) possessed a higher number of large particles than C-10A in Figure 5.4(a). Large clay particle agglomerates have been shown to induce nuclei more than the small thin clay particles in PET [51]. This could explain the greater number of smaller spherulites in the C-N2 than in the C-10A.

The nature of the boundaries between spherulites strongly influences the toughness of a semicrystalline polymer. Butler and Donald [80] investigated spherulitic deformation of polyethylene films and reported that the spherulite boundaries were the weakest areas of the spherulitic structure in all types of polyethylene. The spherulitic deformation occurred first between spherulites (interspherulitic deformation) rather than inside spherulites (intraspherulitic deformation). The number of tie molecules across the spherulite boundaries and between the crystal lamellae within the spherulite strongly affected the toughness of PE films. The number of interlamellar tie molecules depends on both the molecular weight and the lamellar crystal parameters, including long period (L) and lamellar thickness (l_c) and amorphous thickness (l_a). These tie molecules cannot be developed if the end-to-end distance of a polymer molecule in the melt is not greater than ($2l_c + l_a$) [121] as shown in Figure 5.19. Similarly the number of tie molecules across the spherulite boundaries will be dependent on the molecular weight. Strengthening the spherulite boundaries by increasing the number of tie molecules resulted in an increase in toughness of the PE films [80].

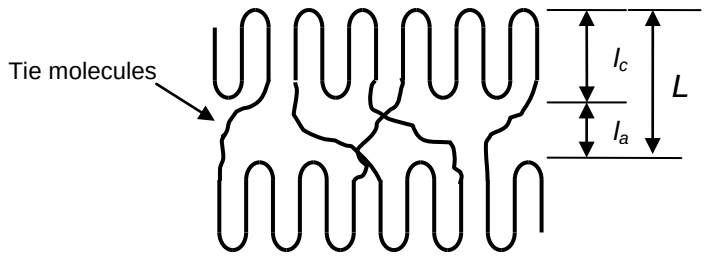

Figure 5.19 It is assumed that a tie molecule between lamella crystals can be formed if its end-to-end distance is greater than $2l_c + l_a$.

The effects of nanoclay on the crystal structure of PET were discussed in section 2.4 in chapter 2. It was found that the presence of nanoclay did not change the crystal unit of PET as shown in Figure 2.10. Recently, Lee and Im [79] blended a PET nanocomposite with layer double hydroxide (LDH) which is known as anion clay with a brucite-like sheet structure. They examined the crystal parameters (L and l_c) of the PET-LDH nanocomposites using small-angle X-ray scattering (SAXS). The SAXS results showed the LDH-clay affected the lamellar crystal parameters of the PET as shown in Figure 2.11. L decreased with increasing the LDH content but l_c did not change. The amorphous thickness (l_a) was obtained from the crystal parameters of L and l_c ($l_a = L - l_c$). The decrease of l_a caused brittleness in the materials [122]. Figure 2.11 shows that the lamellar crystal parameters of the neat PET gave ($2l_c + l_a$) of 36 nm. Generally, the average length of PET molecular chains is in the range between 100 and 150 nm, Table 5.2. If the length of the PET molecules was shortened by three to five times of their original length, the PET chains would have been unable to form tie molecules.

Table 5.2 Molecular weight properties of various PET

M_n of PET (g/mol)	IV of PET (dL/g)	Number of PET repeat unit	Length of PET molecule (nm)	Ref.
18649	0.49	97	104	[123]
19583	0.65	101	108	[124]
23000	0.79	119	127	[125]
26479	0.796	138	148	[126]

Note: The chain repeat unit distance of PET is 10.75Å as examined by X-ray diffraction [126]. The PET (chemical formula: $C_{10}H_8O_4$) molecular weight of repeating unit is 192.2 g/mol [1].

In this study, a significant reduction of the number of tie molecules between the spherulite boundaries was believed to occur in the crystalline nanocomposites, especially the C-10A. The intrinsic viscosity results, Table 5.1, indicated that the C-10A had shorter PET molecules than the ExPET and C-N2. Some of the degraded PET molecules were possibly shorter than ($2l_c + l_a$) and consequently could not form tie molecules. Furthermore, the amorphous material inside and outside the spherulite boundaries reduced with increasing crystallinity. These two phenomena might lead to a reduction in the number of tie molecules between the spherulite boundaries. Consequently, the strength of the spherulite boundaries would be decreased and it would make the nanocomposite more brittle. The crystalline nanocomposites had a higher tensile modulus and a lower breaking strain than the unfilled PET. This would also account for the decrease in the tensile strength of the C-10A with increasing crystallinity as shown in Figure 5.14.

The tensile test results in section 5.4 showed that the tensile strength of C-N2 increased with increasing crystallinity when the compression moulding melt temperature was not more than 260°C. When the processing temperature was higher than 260°C, the C-N2 showed the opposite trend in the tensile strength. This might, again, be attributed to the reduction of the tie molecules in the spherulite boundaries.

5.6 Isothermal crystallization kinetics

Physical, chemical, and thermal properties of semicrystalline polymers such as PET, PA, PP, and PE etc. are strongly enhanced by the presence of the crystalline phase. Generally, the crystallization kinetics of the polymers involves a nucleation and growth process. Understanding of the crystallization kinetics is of great importance to optimize processing conditions (cooling time, rate, and temperature) to obtain products with desired properties. The Avrami equation is a useful equation that is widely used to study the crystallization kinetics, including nucleation types (homogeneous or heterogeneous) and crystal growth geometry (rod, disc, or sphere). This section describes the investigation on the effect of two organoclays with a different surfactant content on the melt crystallization kinetics of PET under isothermal conditions using the Avrami equation.

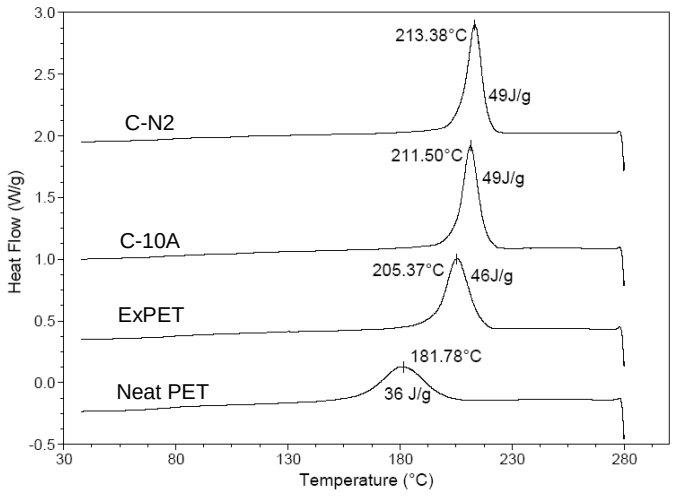

Figure 5.20 DSC pattern of cooling scan for the neat PET, extruded PET, C-10A and C-N2.

Firstly, the cooling scan DSC curves of the neat PET, extruded PET, and PET nanocomposites were examined and these are shown in Figure 5.20. All of the samples were held at 280 °C for five minutes to remove their thermal history and then cooled down to room temperature at a cooling rate of ten °C/min. Compared with the neat PET, the extruded PET had a higher crystallization temperature (T_{hc}) (Δ24°C), a narrower crystallization peak width, and a larger crystallization exotherm (ΔH_{hc}), suggesting an increase of the crystallization rate and the % crystallinity.

As explained in section 5.3, the PET molecular chains were broken by the melt shearing and temperature of the extrusion process that caused a reduction of the intrinsic viscosity and the complex viscosity in the high frequency range. A few research groups have reported the reduction of molecular weight for PET subjected to high temperature processing. Sandro et al. [118] investigated the amount of carboxylic end groups (-COOH) of PET recycled from virgin resin as a function of consecutive recycling steps. It was found that the amount of carboxylic end groups (-COOH) increased as the number of processing cycles increased, indicating that chain scission occurred during each processing cycle. Correspondingly, Anand et al. [127] reported a significant reduction of intrinsic viscosity (IV) of PET from 0.98 to 0.88 dL/g during melt blending that also indicated a reduction of the PET molecular weight. The small molecules resulting from the chain scission are more mobile than the longer chains that enable them to crystallise more readily. The result is that there is an increase in the crystallization temperature, the crystallization rate, and the crystallinity of the processed polymer compared to the virgin polymer.

It has been shown that processing alone significantly influences the crystallization behaviour of PET. Thus, for a true evaluation of the effect of the clay

nanoparticles on PET crystallization, the neat PET and the nanocomposites had to be subjected to the same thermomechanical history.

The nanocomposites of the 10A and the N2 had a higher T_{hc} of Δ6 and Δ8°C than the ExPET respectively. The crystallization peak width of the nanocomposites was narrower and their ΔH_{hc} was slightly higher than those of the ExPET. Similarly, Wang et al. [28] reported that adding 3 wt% of organoclay in PET increased T_{hc} by 10°C.

Figure 5.21 shows the isothermal crystallization curves for the VPET, ExPET, C-10A and C-N2 by cooling molten polymers to different isothermal crystallization temperatures. The isothermal crystallization kinetics was investigated at temperatures ranging from 183 to 200°C for the VPET, from 209 to 218°C for the ExPET, and from 215 to 224°C for both nanocomposites. These isothermal temperature ranges were chosen from the cooling scan curves in Figure 5.20 to ensure that the heat flow and the development of the relative crystallinity could be slow enough to be precisely measured [128,129]. The proper isothermal temperatures provided the perfect isothermal crystallization curves shown in Figure 5.21.

Figure 5.21 clearly shows that the crystallization times for all of the samples increased with increasing T_{hc}. Moreover, all samples in Figures 5.21(a), (b), (c), and (d) show that the crystallization peaks moved to a longer time and became flatter and wider, indicating that the crystallization rate decreased with the increases of the T_{hc}. The reason for this is that the mobility of the polymer chains is high and the nucleation rate is low when the T_{hc} approaches the melting temperature (T_m) (i. e. as the degree of supercooling ($\Delta T = T_m - T_{hc}$) decreases).

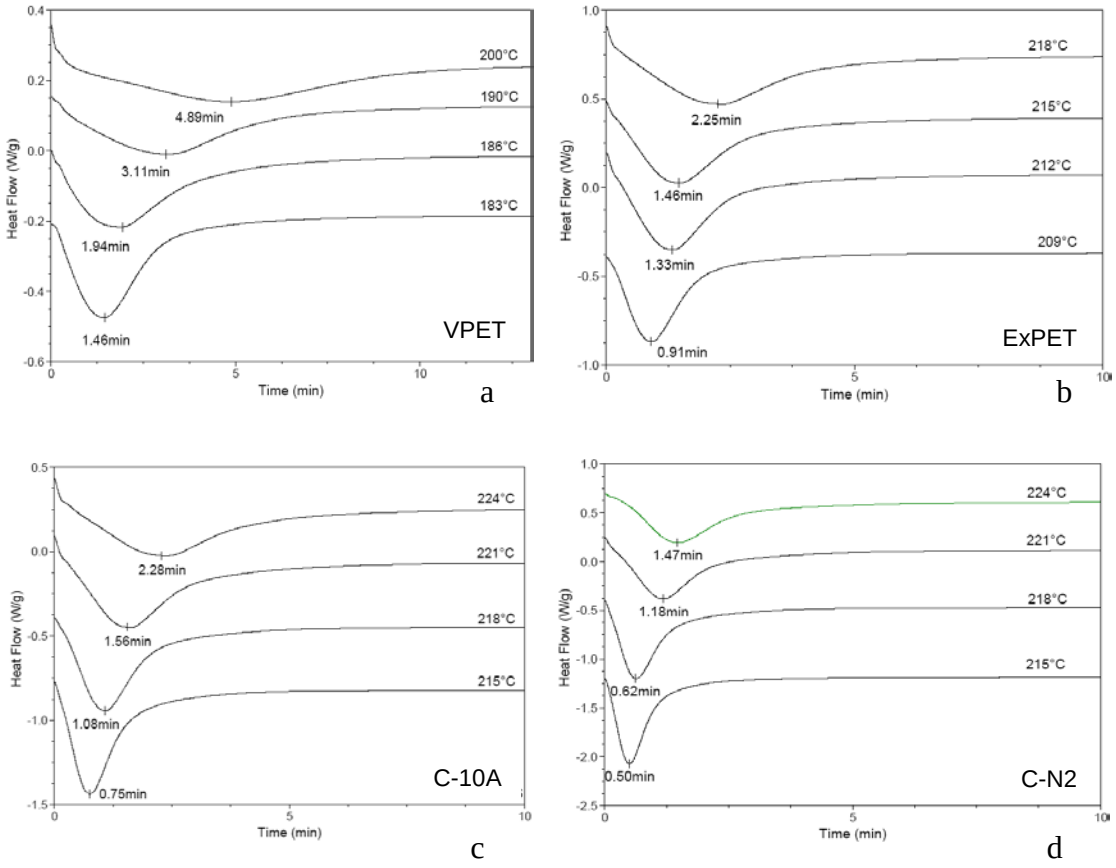

Figure 5.21 Heat flow of isothermal crystallization from the melt for: (a) VPET, (b) ExPET, (c) C-10A, and (d) C-N2.

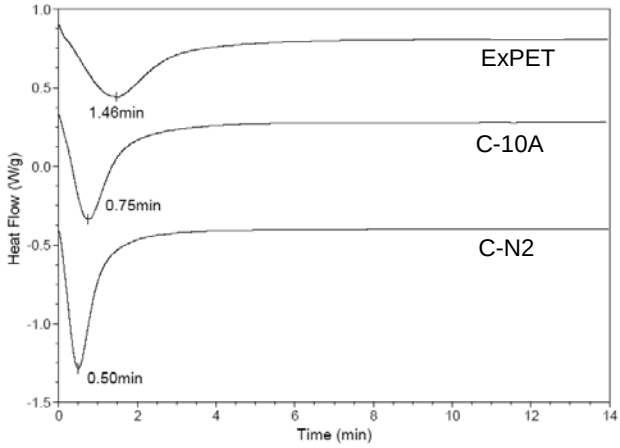

Figure 5.22 Heat flow versus time during isothermal crystallization at T_{hc} of 215°C of ExPET, C-10A, and C-N2.

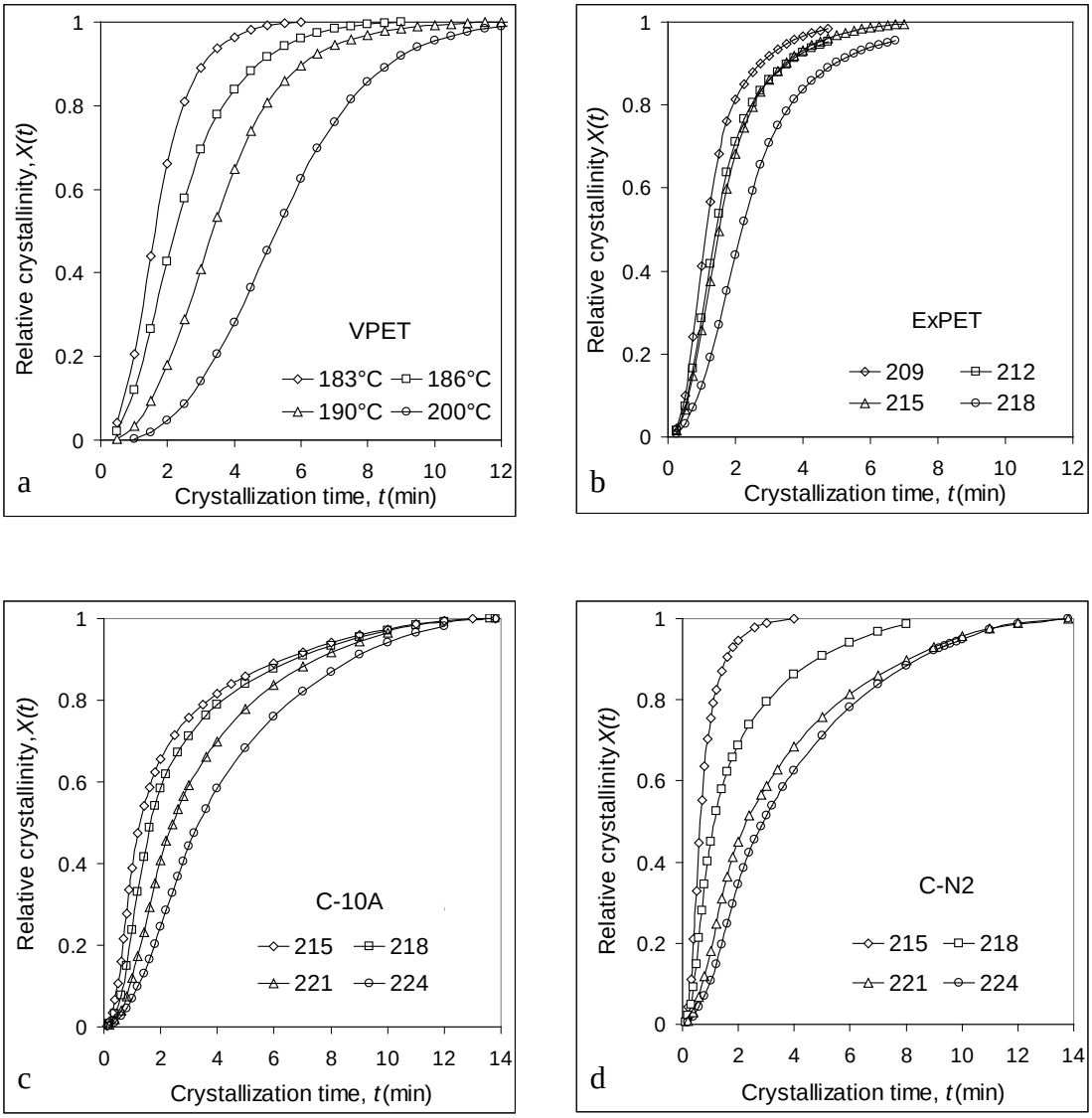

Figure 5.23 Development of relative crystallinity with time during isothermal crystallization for (a) neat PET, (b) ExPET, (c) C-10A, and (d) C-N2.

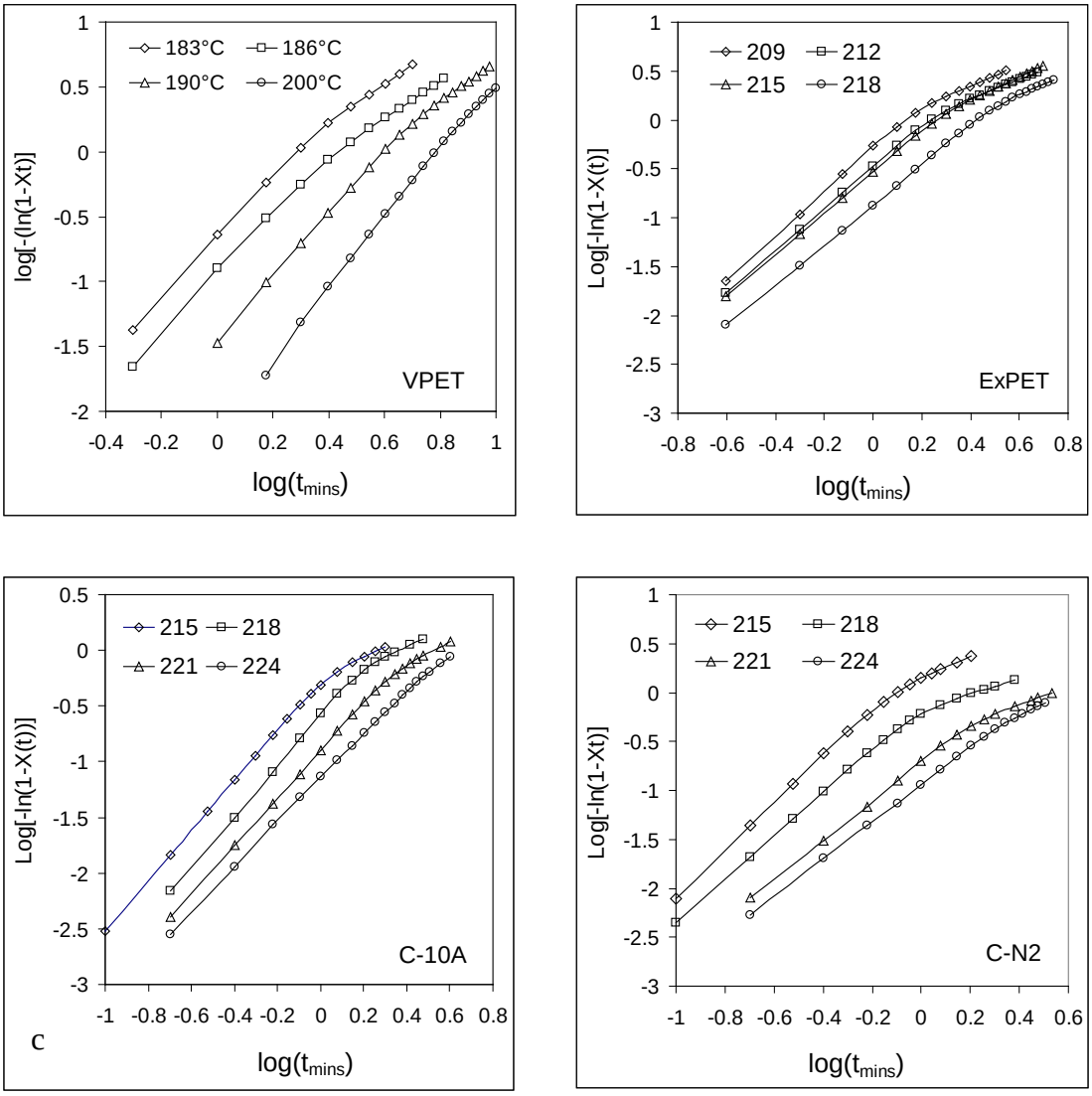

Figure 5.24 Avrami plots for (a) neat PET, (b) ExPET, (c) C-10A, and (d) C-N2.

The isothermal behaviour for the VPET and ExPET was similar, but the ExPET with previous thermal history exhibited a faster crystallization. Figure 5.22 shows the isothermal crystallization curves for the ExPET and both nanocomposites at the crystallization temperature of 215°C. The exothermic peaks of the nanocomposites were sharper than that of the ExPET. In addition, the time to reach the exothermic peak of both nanocomposites was shorter than that of the ExPET by three times for the C-N2 and doubles that for the C-10A. Figure 5.22 clearly shows

that the addition of nanoclay decreased the time to reach the exothermic crystallization peaks and reduced the width of crystallization peak of the ExPET. Both of these effects are the result of an enhanced crystallization rate of the PET nanocomposites. These results suggested that the organoclay had acted as a heterogeneous nucleation agent for PET. The relative crystallinity, *X(t)*, as a function of time (*t*) was calculated from the results shown in Figure 5.21 by the following equation.

$$X(t) = \frac{X_c(t)}{X_c(t_\infty)} = \frac{\Delta H_t}{\Delta H_\infty} = \frac{\int_0^t (dH/dt)dt}{\int_0^\infty (dH/dt)/dt} \tag{5.1}$$

where ΔH_t is the sum of the heat flow from the beginning of the crystallization process to time *t*, and ΔH_∞ is the total heat flow up to the end of the crystallization process. Figure 5.23 shows the relative crystallinity as a function of the crystallization time at different crystallization temperature for the neat PET, extruded PET, and the nanocomposites. It can be observed that the *X(t)* curves exhibited sigmoid shape that increased slowly in the early stage, increased rapidly in the mid stage, and then slowed again at the final stage. All the sigmoid curves were shifted to the right along the time axis with increasing T_{hc}. The isothermal crystallization data of all the samples were further analysed by using the following Avrami equation, as mentioned in section 2.6.

$$1 - X(t) = \exp(-Kt^n) \tag{5.2}$$

This equation is often written as the following double logarithmic equation to easily obtain the value of *K* and *n*.

$$\log[-\ln(1-X(t)] = \log K + n\log t \tag{5.3}$$

where *X(t)* is the relative crystallinity at time *t*, *K* is the overall crystallization rate constant (i.e. nucleation and growth rates), and *n* is the Avrami constant, that is related to the nucleation type (homogeneous or heterogeneous, 1 or 0, respectively) and crystal growth direction (one, two, or three-dimensional growth, from 1 to 3). The Avrami equation is valid when a plot of log [−ln(1 − *X(t)*] vs. log(*t*) shows a straight line [74].

Figure 5.24 shows the curves of log[-ln(1-*X(t)*] against log(*t*) obtained for the neat PET, ExPET, and nanocomposites. The curves show a two-stage crystal growth process. In the primary stage, the curves show a linear relationship, indicating that the crystals grew with a constant growth rate and the Avrami equation was valid. In the secondary stage, a deviation from the linearity of the curves is observed, indicating that the crystal growth rate was not constant due to the beginning of crystal impingement. Figure 5.25 shows the overall crystallization rate constants (*K*) of the VPET, ExPET, and the nanocomposites were constant during the primary crystallization and then increased during the secondary crystallization. The secondary stage began at a crystallization of about 80% for VPET, 60% for ExPET, 50% for C-10A, and 40% for C-N2 as shown in Figure 5.25. The early deviation in the crystal growth for the nanocomposites, especailly C-N2, was due to some of the clay particles acting as instantaneous nuclei, resulting in a reduction of the interspherulitic distance. Hence, the crystal impingement occurred more rapidly for the nanocomposites than that for the unfilled PET.

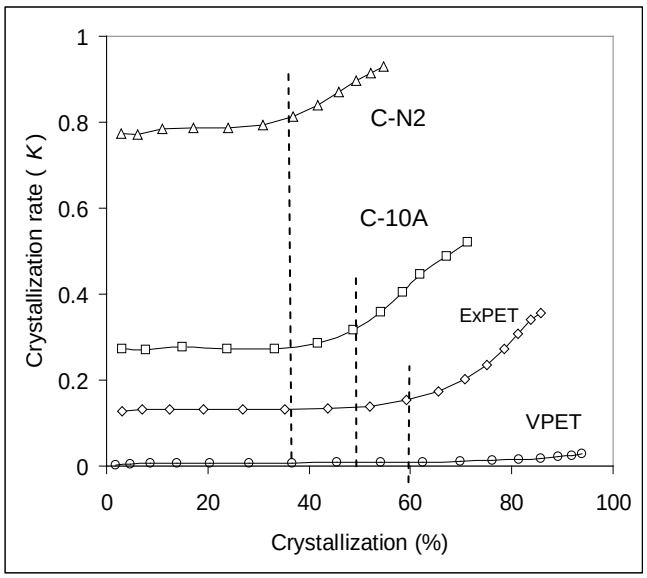

Figure 5.25 Overall crystallization rate (*K*) vs. % crystallization for the ExPET, the nanocomposites with isothermal crystallization temperature of 218°C, and the virgin PET with isothermal crystallization temperature of 200°C.

The *n* and *K* values are directly obtained from the slope and intersection of the straight line of the curves in Figure 5.24, which provide half-time of crystallization ($t_{1/2}$) shown below:

$$t_{1/2} = \left[\frac{\ln 2}{K}\right]^{1/n} \tag{5.4}$$

The half time of crystallization ($t_{1/2}$) was defined as the time at which 50% of the maximum possible crystallinity for the polymer is attained. These crystallization parameters are also listed in Table 5.3. The C-N2 exhibited a lower half-time than the C-10A, indicating that the crystallization rate of the former was higher than that of the latter. Despite less dispersion, N2 was more effective than 10A as a nucleating agent for PET crystallization. Similarly it was reported that PET with unmodified clay (Cloisite Na^+) had a higher crystallization rate than PET with 10A or 15A [51]. It was

explained that the clay surfaces of Cloisite Na^+ with an absence of surfactant are directly in contact with the polymer matrix, which might make Cloisite Na^+ a more efficient heterogeneous nucleation site [130]. The decrease of the surfactant content in the N2 organoclay led to an increase in the interaction between the clay surfaces and the polymer matrix. The N2 organoclay was, therefore, a more efficient nucleation agent than the 10A organoclay.

The Avrami constant (*n*) obtained for the neat PET was in a range of 2.2-2.9, which probably corresponds to a two-dimensional crystal growth with a combination of sporadic (2-D+1) and instantaneous (2-D+0) nucleation or a three-dimensional crystal growth with instantaneous (3-D+0). These *n* values of the neat PET were consistent with the data reported in the literature [73,125]. The extruded PET exhibited values of *n* in the range of 2.0-2.3, in agreement with the data reported by Chae et al. [131]. The reduction of *n* for the extruded materials indicated that the nucleation and growth mechanism of PET were strongly affected by the melt processing. As explained in section 5.6 regarding the degradation of PET during extrusion, the smaller molecules and the impurity particles in the ExPET acted as heterogeneous nucleating agents, leading to *n* approaching the value of 2.

The addition of clay in the PET matrix resulted in insignificant changes of the Avrami constant in relation to the extruded PET as shown in Table 5.3. The Avrami constant of 2 indicated that the growth mechanism of spherulites was two-dimensional rather than three-dimensional. The crystal growth geometry (two or three dimensional growth), however, was unable to be identified by the SEM and PLM images in Figure 5.17 and Figure 5.14 respectively.

Table 5.3 Avrami constant for VPET, ExPET, and nanocomposites

Sample	T_c (°C)	n	$K(\min^{-n})$	$t_{1/2}$ (min)
Neat PET	183	2.3	0.30	1.6
	186	2.2	0.13	2.2
	190	2.7	0.03	3.4
	200	2.9	0.01	5.3
ExPET	209	2.3	0.55	1.1
	212	2.2	0.33	1.4
	215	2.1	0.29	1.5
	218	2.0	0.13	2.2
C-10A	215	2.3	0.57	1.1
	218	2.3	0.27	1.5
	221	2.1	0.13	2.2
	224	2.0	0.07	3.3
C-N2	215	2.4	1.18	0.7
	218	2.3	0.77	1.0
	221	2.0	0.19	1.9
	224	1.9	0.11	2.6

Table 5.4 The crystallization characterisation of polymer nanocomposites

PET & PET + nanofiller	Preparation method	Avrami constant n	Ref
PET	In situ polymerization	3.1-3.3	[72]
PET + Montmorillonite		2.1-2.3	
PET	In situ polymerization	3.1-3.4	[77]
PET + Expandable fluorine mica		2.3-2.6	
PET	In situ polymerization	2.2-2.9	[124]
PET + Silica (SiO_2)		2.3-2.8	
PET	In situ polymerization	2.2-2.7	[132]
PET + Silica (SiO_2)		2.2-3.4	
PET	In situ polymerization	2.8-3.2	[133]
PET + Silica (SiO_2)		2.8-3.6	
PET	Melt blending	2.0-2.2	[131]
PET + Silica (SiO_2)		2.8-3.3	
PET	In situ polymerization	2.3-3.2	[78]
PET + Antimony Doped Tin oxide (ATO)		3.5-4.1	
PET	Melt mixing	2.4-2.6	[134]
PET + Carbon Black		2.1-2.3	

Table 5.4 shows that the Avrami constant of PET nanocomposites blended with different types of nanoparticles. The Avrami constant of PET was decreased from 3 to 2 by the addition of layer particles such as montmorillonite [72] and fluorine mica [77], indicating the dimensionality of crystal growth changed from 3 to 2 dimensions with heterogeneous nucleation. On the contrary, the addition of round-shaped nanoparticles of silica (SiO_2) [124,131-133] or antimony doped tin oxide (ATO) [78] increased the Avrami constant, indicating the 3-dimensional crystal growth with heterogeneous nucleation.

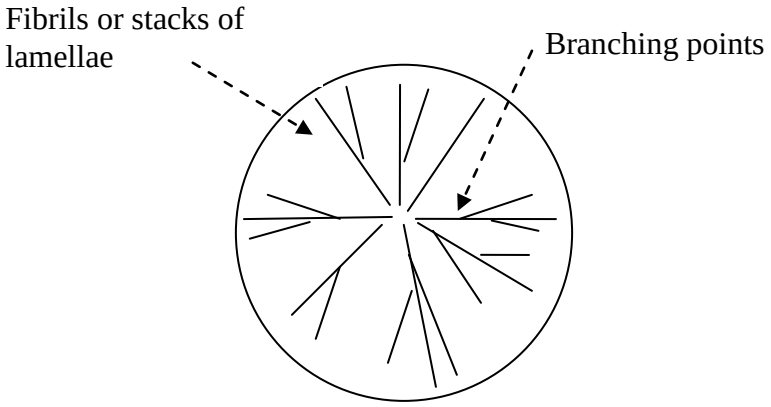

Figure 5.26 Model of spherulitic structure consisting of lamellar fibrils growing radially from a nucleating centre.

A model of the spherulitic structure is shown in Figure 5.26 [135]. The spherulite consists of lamellar fibrils growing radially from a nucleus. The spherulitic fibrils also contain low-angle *branching points*, where new lamellar fibrils are initiated. Bain [136] proposed a relationship between Avrami constant and the number of *branching points* in crystal lamellae, the bigger the number is, the larger the Avrami constant. The ATO and silica nanoparticles might have some physical interaction with the PET molecules that result in an increase in the number of branching points as well as the Avrami constant. In contrast, when the spherulite

growth-fronts hit the clay particles, the spherulites stop growing or grow around the particles as shown in Figure 5.18. This might be the reason for the reduction of the Avrami constant for the PET nanocomposites based on nanoclay.

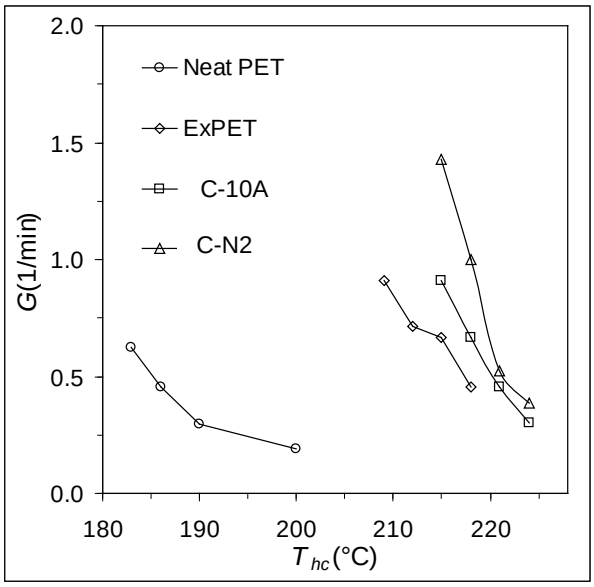

Figure 5.27 The overall crystallization rates ($G = 1/t_{1/2}$) as a function of isothermal crystallization temperature for VPET, ExPET, and nanocomposites.

The trend of the overall crystallization rate can be determined from the reciprocal of the crystallization half-time plotted against the isothermal crystallization temperature as shown in Figure 5.27. The VPET exhibited a gradual increase of the crystallization rate with a decreasing crystallization temperature (or increasing supercooling). The overall crystallization rate was mainly dominated by the nucleation growth rate because the homogeneous nucleation gradually formed from the melt throughout the crystallization process of the VPET. The crystallization rates rapidly increased with a decreasing crystallization temperature (or increase supercooling) for the ExPET and nanocomposites, especially for the C-N2. The impurity particles in the ExPET and the nanoclay in the nanocomposites are believed

to initiate the heterogeneous nucleation that emerged at the beginning of the crystallization process. The overall crystallization rate, therefore, was dominated by the crystal growth rate throughout the crystallization process of the ExPET and the nanocomposites.

5.7 Effect of clay without surfactant on the PET crystallization

The effect of the nanoclay without surfactant (non-surfactant nanoclay) on the melt crystallization behaviour of the PET nanocomposites was investigated. It has been reported that the surfactant on the clay surfaces can be removed by strong acid [137,138] such as trifluoroacetic acid (TFA). This is because the strong acid was able to break the ionic bonding between the surfactant and the clay layers [137]. The present study, therefore, used this technique to remove the surfactant from the surfaces of the organoclay that was dispersed in the melt blended nanocomposite.

The C-10A and C-N2 were dissolved in a mixture of TFA/chloroform (50/50: V/V). The solutions of nanocomposites were then precipitated in methanol at 0°C to obtain the nanocomposites without the surfactant on the clay surfaces. The precipitated materials were dried in a vacuum oven at 80°C for 24 hours to extract the remaining solvent. The non-surfactant clay nanocomposites were labelled as C-10A-M and C-N2-M. The amount of the surfactant remaining in the organoclay can be examined by an evaluation of the nitrogen content using elemental analysis [137]. Unfortunately, it was not possible to make this measurement because this laboratory did not have the required equipment. It has, however, been reported that the TFA/chloroform solvent combination was an effective solvent to remove the surfactant [138]. The hot crystallization behaviour of the non-surfactant clay nanocomposites (C-N2-M and C-10A-M) was analysed using DSC. The DSC cooling

results were compared with those of their original materials (C-10A and C-N2) and the ExPET as shown in Figure 5.28.

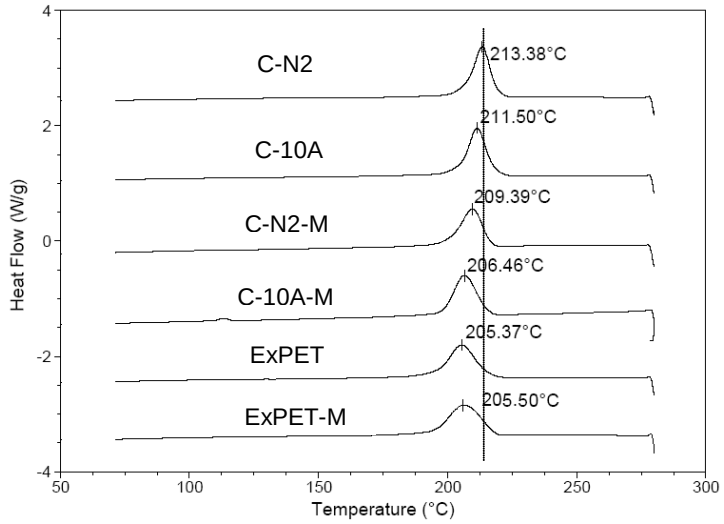

Figure 5.28 DSC cooling curves of the nanocomposites with and without surfactant compared with the ExPET and ExPET-M.

Figure 5.28 revealed that the non-surfactant clay samples possessed a lower hot-crystallization temperature (T_{hc}) than the samples with the surfactant clay. The T_{hc} decreased by 4°C for the C-N2-M and 5°C for the C-10A-M compared with their raw materials. The decrease in the T_{hc} for the 10A nanocomposite was slightly higher than that for the N2 nanocomposite possibly due to the higher amount of surfactant in the 10A. The T_{hc} of both the non-surfactant clay nanocomposites was lower than that of their original nanocomposites. This suggested that the surfactant on the organoclay surfaces significantly influenced the crystallization of the PET nanocomposite. The reason for this was that the surfactant could increase the polymer mobility and lead to an increase in the crystal growth. The increase in the polymer mobility in the surfactant-clay nanocomposites might result from an increase in the PET molecular weight loss due to the low thermal stability of the organoclay.

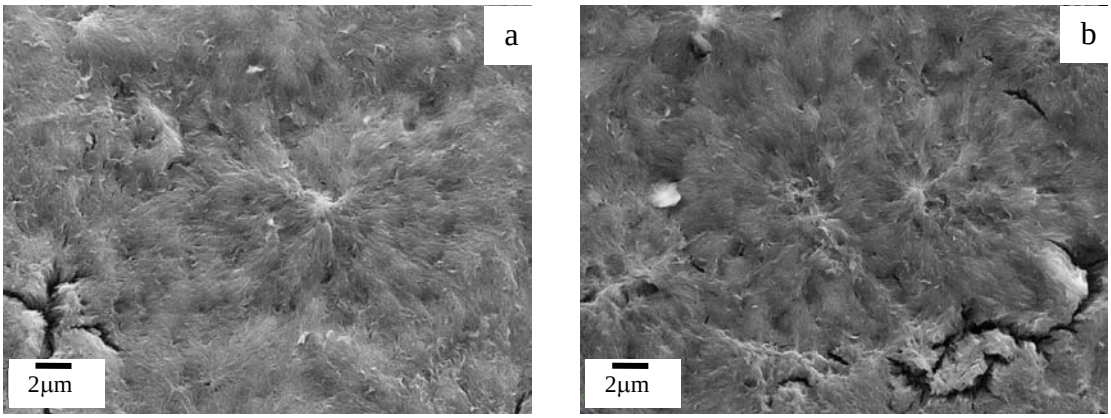

Figure 5.29 SEM images of C-10A-M (a) and (b) C-N2-M which were etched in KOH/methanol solvent for one hour.

Figure 5.28 shows that the C-10A-M had a slightly higher T_{hc} of 1°C than the ExPET, suggesting that the non-surfactant clay in the C-10A-M insignificantly enhanced the PET crystallization. The SEM images in Figure 5.29(a) and Figure 5.17(f) shows that the C-10A-M and C-10A had a similar size and number of spherulites. It seemed that the surfactant in the 10A organoclay improved the PET crystallization by increasing the crystal growth rather than initiating nucleation.

The C-N2-M had a T_{hc} of 4°C higher than the ExPET shown in Figure 5.28, suggesting that the non-surfactant clay in the C-N2-M improved the crystallization more than that in the C-10A-M. Figure 5.29(b) shows that the C-N2-M had a slightly higher number of spherulites than the C-10A-M, Figure 5.29(a). This might be attributed to a lower dispersion of the non-surfactant clay particles in the C-N2-M. It implied that the large clay particles were more efficient nucleation sites for the PET crystallization than the smaller better dispersed particles. It can be concluded, therefore, that the clay particles themselves increased the nucleation rate when they formed large particles while the surfactant in the organoclay increased the crystal growth rate.

5.8 Conclusions

PET nanocomposites based on two organoclays with different percentages of the same surfactant (Cloisite 10A and Nanofil 2) were prepared using a twin screw extruder. The morphological, rheological and mechanical properties, crystal structure and isothermal melt crystallization were investigated and compared to unfilled PET. The conclusions are summarized in the following details.

- Although Cloisite 10A had a higher degradation than the Nanofil 2, the former possessed a higher dispersion of the clay particles than the latter as evidenced by SEM and rheology results.
- The tensile moduli of amorphous and crystalline films of the 10A nanocomposite were greater than those of the N2 nanocomposite and the unfilled PET.
- The tensile strength of the amorphous film of the 10A nanocomposite was greater than that of N2 nanocomposites. On the contrary, the strength of the crystalline film of the former was lower than that of the latter and reduced with an increase in the compression moulding melt temperature.
- The tensile strength of the crystalline N2-PET nanocomposite increased with an increase in the crystallinity when the compression moulding temperature was not more than 260°C. On the contrary, the tensile strength of the crystalline 10A-PET nanocomposite decreased with an increase in the crystallinity for all of the processing temperatures.
- The low thermal stability of the 10A and N2 organoclay appeared to reduce the tensile strength of the *crystalline* nanocomposite but it did not appear to affect the tensile strength of the *amorphous* nanocomposite.
- The 10A nanocomposite possessed a higher molecular weight degradation of the PET matrix than the N2 nanocomposite as evidenced by the intrinsic viscosity.

- Despite a lower dispersion of the clay particles, the strain at break of the N2 nanocomposite with either the amorphous or semicrystalline structure was higher than that of the 10A nanocomposite.
- The poorly dispersed clay particles in the N2 nanocomposite seemed to be more efficient in nucleating PET crystallization than the well dispersed clay particles in the 10A nanocomposite.
- It seemed that the 10A and N2 organoclay did not contribute significantly to the effective heterogeneous nucleation in PET although the N2 appeared to be more efficient than the 10A.
- The isothermal crystallization rates of the PET nanocomposites containing the 10A and N2 were 1.5 and 2.2 times greater than that of the extruded PET respectively.
- The 10A organoclay increased the overall crystallization rate of PET by an increase in the crystal growth rate.
- The N2 organoclay increased the overall crystallization of PET by an increase in the nucleation and crystal growth rates.
- The extruded PET and the nanocomposites possessed the same Avrami constant of 1.9-2.4 that indicated a two-dimensional spherulite growth from heterogeneous nucleation. This also suggested that the nanoclay insignificantly affected the Avrami constant.

Chapter 6

Conclusions

6.1 General conclusions

Solvent blending system

The following conclusions have been drawn on the results of this work.

- Preparation of well exfoliated organoclay (Cloisite 10A) in a PET matrix was accomplished by using a two-step blending process as follows.
    1. Pre-blending a master batch of a solvent blended PET/organoclay nanocomposite with ultrasonication and epoxy.
    2. Blending the master batch with virgin PET in a twin screw extruder.
- Solvent blending provided a higher dispersion of clay particles than melt blending.
- Among four commercial organoclays including Cloisite 10A, Nanofil-2, and SE3010, Cloisite 10A possessed the highest dispersion in PET.
- Cloisite 15A was unsuitable to blend with PET in a solvent of phenol and chloroform because the 15A suspension in the PET solution was unstable.
- Nanofil 2 was dispersed less in the solvent blended nanocomposite than Cloisite 10A due to a lower amount of surfactant in the former than in the latter. It suggested that increasing the amount of surfactant led to an increase in the dispersion.
- SE3010 possessed the lowest dispersion in PET.
- The 4-5% of residual phenol was present in the solvent blended nanocomposite after drying in a vacuum oven at 80°C for 48 hours and strongly affected the PET crystallization.

- The crystallization behaviour of solvent blended PET/clay nanocomposite was not only influenced by the nanoclay but also by the residual solvent.
- The T_g of the solvent blended PET nanocomposite decreased due to the residual solvent.
- The nanoclay rather than the residual solvent decreased the cold-crystallization temperature of the solvent blended PET nanocomposite.
- In contrast, the increase in melt-crystallization temperature of the solvent blended nanocomposites was mainly affected by the residual solvent rather than the nanoclay.
- The degree of dispersion of the nanoclay did not affect the crystallization of the solvent blended PET nanocomposites.

Melt blending system

Effect of the amount of surfactant on the nanoclay dispersion in PET and physical properties of the melt blended nanocomposites was investigated. Both melt blended nanocomposites possessed a mixture of intercalation and tactoid structure. Increasing the surfactant concentration led to an increase in the nanoclay dispersion resulting in enhancement in tensile modulus and strength but it reduced PET crystallization rate. The degradation of the organoclay did not limit the nanoclay dispersion. The low thermal stability of the organoclays reduced the tensile strength of the crystalline nanocomposite but it did not affect the tensile strength of the amorphous nanocomposite. The surfactant in the organoclay affected the crystal growth rate while the nanoclay itself affected the nucleation rate when its dispersion was not high.

6.2 Future work

The present study showed that the use of epoxy (diglycidyl ethers bisphenol-A or DGEBA) as a compatibilizer led to a significant increase in the dispersion of nanoclay in PET matrix. It, however, lowered the viscosity of PET, which possibly reduced the efficiency of PET intercalation into the nanoclay gallery due to reduced shear stress possibly in processing. Complete exfoliated clay nanocomposite was, therefore, not achieved. The other chain extenders that were able to increase the PET viscosity could be used to study further.

Besides the use of a chain extender, a proper blending sequence as shown in the following steps could lead to the development of a fully exfoliated clay nanocomposite.

1. Modify PET with a proper chain extender to increase the viscosity of the PET.
2. Modify organoclay with the extender to improve the compatibility between the organoclay and the PET.
3. Blend the modified PET and the modified organoclay via solvent blending or a twin screw extruder.

This work has reported the relationship between the crystal structure and tensile properties of PET/organoclay nanocomposite. Further investigation of the spherulitic deformation mechanisms might provide more details of the influence of the microstructure and the nanoclay on the mechanical behaviour of the PET/organoclay nanocomposites using copper grid technique.

References

1. F. Awaja and D. Pavel, *Eur Polym J*, **41**, 1453 (2005)
2. T. Rieckmann and S. Volker, In Modern polyesters: Chemistry and Technology of Polyesters and Copolyesters; Scheirs, J.; Long, T. E., Eds.; John Wiley and Sons: West Sussex, UK, 2003, p 35.
3. T. Rieckmann and S. Volker, In Modern polyesters: Chemistry and Technology of Polyesters and Copolyesters; Scheirs, J.; Long, T. E., Eds.; John Wiley and Sons: West Sussex, UK, 2003, p 52.
4. A. B. String, Plastic Materials and Processing; Prentice-Hall: New Jersey, 1996.
5. N. C. Lee, Plastic Blow Molding Handbook; Chapman and Hall: London, 1990.
6. B. Tekkanat, In PET Packaging Technology; Brooks, D. W.; Giles, G. A., Eds.; Sheffield Academic Press Ltd: Sheffield, 2002.
7. M. Lu, K. Manning, S. Nelsen, and S. Leyrer, In ANTEC 1998; SPE: Atlanta, 1998.
8. A. Okada and A. Usuki, *Mater Sci Eng* , **C3**, 109 (1995)
9. K. Masaya, *J. Polym. Sci. Part A: Polym Chem*, **42**, 819 (2004)
10. http://www.nanocor.com/tech_sheets2.asp/ Last accessed 08 December 2008
11. P. C. Lebaron, Z. Wang, and T. J. Pinnavaia., In Polymer-Clay Nanocomposites; T.J. Pinnavaia, G. W. B., Ed.; Wiley: New York, 2001.
12. S. S. Ray and M. Okamoto, *Prog Polym Sci* , **28**, 1539 (2003)
13. M. G. Fonseca, C. R. Silva, J. S. Barone, and C. Airoldi, *J Mater Chem*, **10**, 789 (2000)
14. Q. H. Zeng, A. B. Yu, G. Q. (Max) Lu, and D. R. Paul, *J Nanosci Nanotechnol*, **5**, 1574 (2005)
15. N. Ogata, S. Kawakage, and T. Ogihara, *J Appl Polym Sci*, **66**, 573 (1997)
16. T. D. Fornes, D. L. Hunter, and D. R. Paul, *Polym*, **45**, 2321 (2004)
17. T. D. Fornes and D. L. Hunter, *Macromol*, **37**, 7698 (2004)
18. T. D. Fornes, P. J. Yoon, and D. R. Paul, *Polym*, **43**, 6727 (2002)
19. H. R. Dennis, D. L. Hunter, D. Chang, S. Kim, J. L. White, J. W. Cho, and D. R. Paul, *Polym*, **42**, 9513 (2001)
20. R. Krishnamoorti and K. Yurekli, *Curr Opin Coll Interface Sci*, **6**, 464 (2001)
21. F. Gao, *Materials Today*, **7**, 50 (2004)
22. H. B. Kim, J. S. Choi, C. H. Lee, S. T. Lim, M. S. Jhon, and H. J. Choi, *Eur Polym J*, **41**, 679 (2005)
23. S. S. Lee, Y. T. Ma, H. W. Rhee, and J. Kim, *Polym*, **46**, 2201 (2005)
24. T. Y. Tsai, C. H. Li, C. H. Chang, W. H. Cheng, C. L. Hwang, and R. J. Wu, *Adv Mater*, **17**, 1769 (2005)
25. Z. Ke and B. Yongping, *Mater Lett*, **59**, 3348 (2005)
26. S. H. Kim and S. C. Kim, *J Appl Polym Sci*, **103**, 1262 (2007)

27. Y. Li, J. Ma, Y. Wang, and B. Liang, *J Appl Polym Sci*, **98**, 1150 (2005)
28. Y. Wang, J. Gao, Y. Ma, and U. S. Agarwal, *Compos B Eng*, **37**, 399 (2006)
29. U. Gurmendi, J. I. Eguiazabal, and J. Nazabal, *Macromol Mater Eng*, **292**, 169 (2007)
30. M.C. Lai, K.C. Chang, W. C. Huang, S. C. Hsu, and J. M. Yeh, *J Phys Chem Solids*, **69**, 1371 (2008)
31. G. D. Barber and R. B. Moore, *ACS PMSE Proceedings*, **82**, 241 (2000)
32. C. F. Ou, M. T. Ho, and J. R. Lin, *J Polym Res*, **10**, 127 (2003)
33. C. F. Ou, M. T. Ho, and Z. Qi., *J Appl Polym Sci*, **91**, 140 (2004)
34. Y. Ke, C. Long, and Z. Qi, *J Appl Polym Sci*, **71**, 1139 (1999)
35. J. H. Chang, S. J. Kim, Y. L. Joo, and S. Im, *Polym*, **45**, 919 (2004)
36. Y. Imai, S. Nishimura, E. Abe, H. Tateyama, A. Abiko, A. Yamaguchi, T. Aoyama, and H. Taguchi, *Chem Mater*, **14**, 477 (2002)
37. G. Zhang, T. Shichi, and K. Takagi, *Mater Lett*, **57**, 1858 (2003)
38. J. Hao, X. Lu, S. Liu, S. Khim, L. Yang, and C. Chua, *J Appl Polym Sci*, **101**, 1057 (2006)
39. W. J. Choi, H. J. Kim, K. H. Yoon, O. H. Kwon, and C. I. Hwang, *J Appl Polym Sci*, **100**, 4875 (2006)
40. J. C. Matayabas and S. R. Turner, In Polymer-Clay Nanocomposites; T.J. Pinnavaia, G. W. B., Ed.; Wiley: New York, 2001.
41. http://www.rockwoodadditives.com/nanoclay/ Last accessed 08 December 2008
42. C. H. Davis, L. J. Mathias, J. W. Gilman, D. A. Schiraldi, J. R. Shields, P. Trulove, T. E. Sutto, and H. C. Delong, *J Polym Sci Part B Polym Phys*, **40**, 2661 (2002)
43 C. I. W. Calcagno, C. M. Mariani, S. R. Teixeira, and R. S. Mauler, *Polym*, **48**, 966 (2007)
44. E. Alyamac and U. Yilmazer, *Polym Compos*, **28**, 251 (2007)
45. S. E. Vidotti, A. C. Chinellato, G. H. Hu, and L. A. Pessan, *J Polym Sci Part B Polym Phys*, **45**, 3084 (2007)
46. A. Pegoretti, J. Kolarik, C. Peroni, and C. Migliaresi, *Polym*, **45**, 2751 (2004)
47. M. Kracalik, J. Mikesoa, R. Puffr, J. Baldrian, R. Thomann, and C. Friedrich, *Polym Bull*, **58**, 313 (2007)
48. M. T. M. Bizarria, A. L. F. D. M. Giraldi, C. M. D. Carvalho, J. I. Velasco, M. A. D. Avila, and L. H. I. Mei, *J Appl Polym Sci*, **104**, 1839 (2007)
49. M. Kracalik, M. Studenovsky, J. Mikesoa, J. Kovarova, A. Sikora, R. Thomann, and C. Friedrich, *J Appl Polym Sci*, **106**, 2092 (2007)
50. M. Kracalik, M. Studenovsky, J. Mikesoa, A. Sikora, R. Thomann, C. Friedrich, and J. Simonik, *J Appl Polym Sci*, **106**, 926 (2007)
51. G. D. Barber, B. H. Calhoun, and R. B. Moore, *Polym*, **46**, 6706 (2005)
52. http://www.arkema.com/group/en/products/detailed_sheets/technical_polymers/lotader/product_info/home.page/ Last accessed 08 December 2008
53. M. C. Costache, M. J. Heidecker, E. Manias, and C. A. Wilkie, *Polym Adv Technol*, **17**, 764 (2006)

54. N. Hasegawa and A. Usuki, *J Appl Polym Sci*, **93**, 464 (2004)
55. S. S. Ray, K. Okamoto, and M. Okamoto, *Macromol*, **36**, 2355 (2003)
56. H. A. Barnes, J. F. Hutton, and K. Walters. An Introduction to Rheology; Elsevier: Amsterdam, 1989.
57. J. M. Dealy and K. F. Wissbrun, Melt Rheology and It's Role in Plastics Processing: Theory and Applications; Van Nostrand Reinhold: New York, 1990.
58. R. Krishnamoorti, R. A. Vaia, and E. P. Giannelis, *Chem Mater* , **8**, 1728 (1996)
59. R. Krishnamoorti and E. P. Giannelis, *Macromol*, **30**, 4097 (1997)
60. J. Ren, A. S. Silva, and R. Krishnamoorti, *Macromol*, **33**, 3739 (2000)
61. R. Krishnamoorti and E. P. Giannelis, *Langmuir*, **17**, 1448 (2001)
62. J. Zhao, A. B. Morgan, and J. D. Harris, *Polym*, **46**, 8641 (2005)
63. R. Wagener and T. J. G. Reisinger, *Polym*, **44**, 7513 (2003)
64. T. D. Fornes, and D. R. Paul, *Polym*, **44**, 4993 (2003)
65. T. D. Fornes, P. J. Yoon, H. Keskkula, and D. R. Paul, *Polym*, **42**, 9929 (2001)
66. R. K. Shah, D. H. Kim, and D. R. Paul, *Polym*, **48**, 1047 (2007)
67. A. N. Wilkinson, Z. Man, J. L. Stanford, P. Matikainen, M. L. Clemens, G. C. Lees, and C. M. Liauw, *Compos Sci Technol*, **67**, 3360 (2007)
68. J. Scheirs, In Modern polyesters: Chemistry and Technology of Polyesters and Copolyesters; Scheirs, J.; Long, T. E., Eds.; John Wiley and Sons: West Sussex, UK, 2003, p 516.
69. G. Reese, In Modern polyesters: Chemistry and Technology of Polyesters and Copolyesters; Scheirs, J.; Long, T. E., Eds.; John Wiley and Sons: West Sussex, UK, 2003, p 404.
70. C. Wutz, M. Bark, J. Cronauer, R. Dohrmann, and H. G. Zachmann, Rev Sci Instrum, 66 (1995)
71. C. Bai, R. J. Spontak, C. C. Koch, C. K. Saw, and C. M. Balik, *Polym*, **41**, 7147 (2000)
72. T. Wan, L. Chen, Y. C. Chua, and X. Lu, *J Appl Polym Sci*, **94**, 1381 (2004)
73. X.F. Lu and J. N. Hay, *Polym*, **42**, 9423 (2001)
74. R. M. R. Wellen and M. S. Rabello, *J Mater Sci*, **40**, 6099 (2005)
75. G. H. Hsu, Y. N. Yang, T. L. Yu, and H. L. Lin, *J Polym Res*, **13**, 361 (2006)
76. B. Culbert, and A. Christel, In Modern polyesters: Chemistry and Technology of Polyesters and Copolyesters; Scheirs, J.; Long, T. E., Eds.; John Wiley and Sons: West Sussex, UK, 2003, p 161.
77. C. Saujanya, Y. Imai, and H. Tateyama, *Polym Bull*, **51**, 85 (2003)
78. X. Chen, C. Li, and W. Shao, *Euro Polym J*, **43**, 3177 (2007)
79. W. D. Lee, and S. S. Im, *J Polym Sci Part B Polym Phys*, **45**, 28 (2007)
80. M. F. Butler, and A. M. Donald, *J Mater Sci*, **32**, 3675 (1997)
81. H. W. Starkweather, P. Zoller, and G. A. Jones, *J Polym Sci Polym Phys*, **21**, 295 (1983)
82. C. Riccardi, R. Barni, E. Selli, G. Mazzone, M. R. Massafra, B. Marcandalli, and G. Poletti., *Appl Surf Sci*, **211**, 386 (2003)
83. J.W. Cho and D. R. Paul, *Polym*, **42**, 1083 (2001)

84. J. Ren, Adriana S. Silva, and R. Krishnamoorti, *Macromol*, **33**, 3739 (2000)
85. A. B. Morgan, J. W. Gilman, and C. L. Jackson, *Macromol*, **34**, 2735 (2001)
86. G. S. Sura, H. L. Sunb, S. G. Lyua, and J. E. Mark, *Polym*, **42**, 9783 (2001)
87. R. Xu, E. Manias, A. J. Snyder, and J. Runt, *Macromol*, **34**, 337 (2001)
88. C. J. G. Plummer, L. Garamszegi, Y. Leterrier, M. Rodlert, and J. E. Manson , *Chem Mater*, **14**, 486 (2002)
89. C. A. Mitchell and R. Krishnamoorti, *J Polym Sci Part B Polym Phys*, **40**, 1434 (2002)
90. A. B. Morgan and J. D. Harris, *Polym*, **45**, 8695 (2004)
91. C. Chen and T. B. Tolle, *J Polym Sci*, **42**, 3981 (2004)
92. D. Wu, C. Zhou, W. Yu, and X. Fan, *J Polym Sci Part B Polym Phys*, **43**, 2807 (2005)
93. D. Wu, C. Zhou, W. Yu, and F. Xie, *J Appl Polym Sci*, **99**, 340 (2006)
94. M. Lai and J.K. Kim, *Polym*, **46**, 4722 (2005)
95. K. Dean, J. Krstina, W. Tian, and R. J. Varley, *Macromol Mater Eng*, **292**, 415 (2007)
96. N. N. Mahamuni and A. B. Pandit, *Ultrason Sonochem*, **13**, 165 (2006)
97. D. Wu, C. Zhou, X. Fan, D. Mao, and Z. Bian, *Polym Degrad Stab*, **87**, 511 (2005)
98. L. Xu, S Reeder, M. Thopasridharan, J. Ren, D. A. Shipp, and R. Krishnamoorti, *Nanotechnol*, **16**, 514 (2005)
99. H. Ma, L. Tong, Z. Xu, and Z. Fang, *Polym Degrad Stab*, **92**, 1439 (2007)
100. A. A. Haralabakopoulos, D. Tsiourvas, and C. M. Paleos, *J Appl Polym Sci*, **71**, 2121 (1999)
101 S. C. Jana, N. Patel, and D. Dharaiya, *Polym*, **42**, 8681 (2001)
102. S. Podzimek, *J Appl Polym Sci*, **54**, 91 (1994)
103. K. Weisskopf, *J Appl Polym Sci*, **39**, 2141 (1990)
104. D. I. Bower. An Introduction to Polymer Physics, 2002.
105. A. A. Lambert, K. A. Mauritz, and D. A. Schiraldi, *J Appl Polym Sci*, **84**, 1749 (2002)
106. I. Y. Phang, K. Pramoda, D. T. Liu, and C. He, *Polym Int*, **53**, 1282 (2004)
107. M. L. D. Lorenzo, M. E. Errico, and M. Avella, *J Mater Sci*, **37**, 2351 (2002)
108. J. P. He, H. M. Li, X. Y. Wang, and Y. Gao, *Euro Polym J*, **42**, 1128 (2006)
109. W. S. Depolo, D. W. Litchfield, and D. G. Baird. ANTEC, (2006)
110. A. J. Hsieh, P. Moy, F. L. Beyer, P. Madison, E. Napadensky, J. Ren, and R. Krishnmoorti, *Polym Eng Sci*, **44**, 825 (2004)
111. P. J. Yoon, D. L. Hunter, and D. R. Paul, *Polym*, **44**, 5341 (2003)
112. A. S. Solis, I. R. Ibarra, M. R. Estrada, F. Calseras, and O. Manero, *Polym Eng Sci*, **44**, 1094 (2004)
113 L. Cui, D. M. Khramov, C. W. Bielawski, D. L. Hunter, P. J. Yoon, and D. R. Paul, *Polym*, **49**, 3751 (2008)
114. T.D. Fornes, P.J. Yoon, and D. R. Paul, *Polym*, **44**, 7545 (2003)
115. F. Chavarria and D. R. Paul, *Polym*, **45**, 8501 (2004)
116. M. Imai and K. Kaji, *Polym*, **47**, 5544 (2006)

117. MA. J. L. Gonzalez, M. T. R. Hernandez, E. A. G. L. Santos, and J. V. Olmos, *J Appl Poly Sci*, **76**, 851 (2000).
118. S. D. Mancini and M. Zanin, *Mater Res*, **2**, 33 (1999)
119. Y. C. Chua, S. W. Lin, and L. X. Lu, *Macromol Chem Phys*, **208**, 1789 (2007)
120. K. E. Strawhecker and E. Manias, *Chem Mater*, **15**, 844 (2003)
121. Y.L. Huang and N. Brown, *J Polym Sci Polym Phys*, **29**, 129 (1991)
122. B. Fayolle, X. Colin, L. Audouin, and J. Verdu, *Polym Degrad Stab*, **92**, 231 (2007)
123 L. Incarnatoa, P. Scarfatoa, L. D. Maioa, and D. Aciernob, *Polym*, **41**, 6825 (2000)
124 Y. C. Ke, T. B. Wu, and Y. F. Xia, *Polym*, **48**, 3324 (2007)
125 G. Z. Papageorgiou, D. S. Achilias, D. N. Bikiaris, and G. P. Karayannidis, *J Therm Anal Calorim*, **84**, 85 (2006)
126. K. M. Jones, In PET packaging technology; Brooks, D. W.; Giles, G. A., Eds.; Sheffield Academic Press Ltd: Sheffield, 2002, p 44.
127. K. A. Anand, U. S. Agarwal, and R. Joseph, *Polym*, **47**, 3976 (2006)
128. L. Sorrentino, S. Iannace, E. D. Maio, and D. Acierno, *J Polym Sci Part B Polym Phys*, **43**, 1966 (2005)
129. A. T. Lorenzo, M. L. Arnal, J. Albuerne, and A. J. Muller, *Polym Test*, **26**, 222 (2007)
130. K. Stoeffler, P. G. Lafleur, and J. Denault, *Polym Degrad Stab*, **93**, 1332 (2008)
131. D. W. Chae and B. C. Kim, *J Mater Sci*, **42**, 1238 (2007)
132. Y. Yang, H. Xu, and H. Gu, *J Appl Polym Sci*, **102**, 655 (2006)
133. X. Tian, C. Ruan, P. Cui, W Liu, J. Zheng, X, Zhang, X, Yao, Kangzheng, and Y. Li, *J Macromol Sci Part B Phys*, **45**, 835 (2006)
134. G. Q. Zhang, F. Sun, L. P. Gao, L. N. Wang, M. Shao, and D. J. Q. Liu, *J Compos Mater*, **41**, 1477 (2007)
135. L. H. Spering. Introduction to Physical Polymer Science; John Wiley & Sons, Inc.: New York, 1985.
136. J. Bian, S. R. Ye, and L. X. Feng, *J Polym Sci Part B: Polym Phys*, **41**, 2135 (2003)
137. D. Lee and K. Char, Langmuir, 18, 6445 (2002)
138. J. W. Chung, S. B. Son, S. W. Chun, T. J. Kang, and S. Y. Kwak, *Polym Degrad Stab*, **93**, 252 (2008)